

Hydrogen Embrittlement Susceptibility of Ferritic High Strength Steels An Experimental Approach

Boot, T.

DOI

[10.4233/uuid:33005955-017b-492b-8760-2da34cd950ca](https://doi.org/10.4233/uuid:33005955-017b-492b-8760-2da34cd950ca)

Publication date

2025

Document Version

Final published version

Citation (APA)

Boot, T. (2025). *Hydrogen Embrittlement Susceptibility of Ferritic High Strength Steels: An Experimental Approach*. [Dissertation (TU Delft), Delft University of Technology]. <https://doi.org/10.4233/uuid:33005955-017b-492b-8760-2da34cd950ca>

Important note

To cite this publication, please use the final published version (if applicable).
Please check the document version above.

Copyright

Other than for strictly personal use, it is not permitted to download, forward or distribute the text or part of it, without the consent of the author(s) and/or copyright holder(s), unless the work is under an open content license such as Creative Commons.

Takedown policy

Please contact us and provide details if you believe this document breaches copyrights.
We will remove access to the work immediately and investigate your claim.

The background of the cover is a grid of yellow circles. In the center, there is a cluster of circles in green and brown, representing a crystal lattice or a specific material structure. The text is overlaid on this pattern.

Hydrogen Embrittlement Susceptibility of Ferritic High Strength Steels

An Experimental Approach

Tim Boot

HYDROGEN EMBRITTLEMENT SUSCEPTIBILITY OF FERRITIC HIGH STRENGTH STEELS

AN EXPERIMENTAL APPROACH

HYDROGEN EMBRITTLEMENT SUSCEPTIBILITY OF FERRITIC HIGH STRENGTH STEELS

AN EXPERIMENTAL APPROACH

Dissertation

for the purpose of obtaining the degree of doctor
at Delft University of Technology
by the authority of the Rector Magnificus, prof. dr. ir. T.H.J.J. van der Hagen,
chair of the Board for Doctorates
to be defended publicly on
Friday 5 December 2025 at 12:30 o'clock

by

Tim BOOT

Master of Science in Materials Science and Engineering, Delft University of Technology,
The Netherlands
born in Rotterdam, The Netherlands

This dissertation has been approved by the promotor.

Composition of the doctoral committee:

Rector Magnificus,	chairperson
Dr. V. A. Popovich,	Delft University of Technology, <i>promotor</i>
Dr. A. J. Böttger,	Delft University of Technology, <i>promotor</i>

Independent members:

Prof. dr. ir. J. M. C. Mol	Delft University of Technology
Prof. dr. H. Hajibeygi	Delft University of Technology
Prof. dr. M. Djukic	University of Belgrade, Serbia
Prof. dr. K. Verbeken	Ghent University, Belgium
Dr. Ir. M. J. M. Hermans	Delft University of Technology, reserve member

This research was carried out under project number N19009c in the framework of the Partnership Program of the Materials innovation institute M2i (www.m2i.nl) and the Netherlands Organization for Scientific Research (www.nwo.nl).



TATA STEEL



Keywords: Hydrogen Embrittlement, Titanium Carbide, Vanadium Carbide, Dual Phase, Steel

Printed by: Ridderprint | <https://www.ridderprint.nl/>

Cover by: Tim Boot

Copyright © 2025 by T. Boot

ISBN 978-94-6522-759-7

An electronic copy of this dissertation is available at
<https://repository.tudelft.nl/>.

To all those before me, and hopefully many more after me, who write without the use of
Large Language Models.

CONTENTS

Summary	xi
Samenvatting	xv
1. Introduction	1
1.1. Motivation for this project	1
1.2. Materials Challenges	3
1.2.1. Detrimental strengthening mechanisms	3
1.2.2. Time-dependent behaviour	3
1.2.3. Nano-scale interactions	4
1.3. Research objectives and thesis outline	4
2. Background	7
2.1. Hydrogen Absorption	7
2.2. Mechanisms of Hydrogen Embrittlement	8
2.3. Influence of microstructural features	12
2.3.1. Dislocations	12
2.3.2. Grain Boundaries	13
2.3.3. Different Phases	13
2.3.4. Intermetallic Precipitates	14
2.4. Influence of external factors	15
2.4.1. Surface roughness	15
2.4.2. Charging environment	16
2.4.3. Stress and strain concentrations	16
2.4.4. Strain rate	18
2.5. Summary and conclusions	19
3. Nano-precipitate Steels after Gaseous Hydrogen Charging	21
3.1. Introduction	22
3.2. Materials & Methods	24
3.2.1. Microstructural Characterisation	26
3.2.2. Thermal Desorption Spectroscopy	28
3.2.3. Mechanical Characterisation	28
3.3. Results & Discussion	28
3.3.1. Grain size evolution	28
3.3.2. Precipitate growth	29
3.3.3. Effect on hydrogen absorption	33
3.3.4. Origins of hydrogen trapping in TiC	35
3.3.5. Origins of hydrogen trapping in VC	38

3.3.6. Effect on mechanical behaviour	39
3.4. Conclusions	41
4. Nano-precipitate Steels after Electrochemical Hydrogen Charging	43
4.1. Introduction	44
4.2. Methods	45
4.2.1. Heat treatment and characterisation	45
4.2.2. Resulting microstructures	46
4.2.3. In-situ Slow Strain Rate Tensile testing	49
4.2.4. Hydrogen analysis	49
4.3. Results	51
4.3.1. Hydrogen Absorption	51
4.3.2. Mechanical behaviour	51
4.4. Discussion	52
4.5. Conclusions	60
5. Effects of Plastic Deformation	63
5.1. Introduction	64
5.2. Methods	65
5.2.1. Heat treatment and microstructure	65
5.2.2. In-situ Multi-Step Tensile testing	66
5.2.3. Hydrogen analysis	67
5.2.4. Characterisation	69
5.3. Results	70
5.3.1. Hydrogen Absorption	70
5.3.2. Measurements of plastic deformation	72
5.4. Discussion	73
5.5. Conclusions	78
6. Effects of Martensite Content in Dual Phase Steels	81
6.1. Introduction	82
6.2. Materials and Methods	83
6.2.1. Heat treatments and characterisation	84
6.2.2. Hydrogen charging and mechanical testing	85
6.3. Results and Discussion	86
6.3.1. Creation of microstructures	86
6.3.2. Hydrogen trapping	87
6.3.3. Mechanical behaviour	88
6.3.4. The role of martensite in fracture	92
6.3.5. The role of martensite in fracture initiation	93
6.4. Conclusions	96
7. Discussion and Conclusions	99
7.1. Discussion	99
7.1.1. The effects of precipitate size	99
7.1.2. The effects of precipitate type	101

7.1.3. The effects of charging environment	101
7.1.4. The effects of plastic deformation	102
7.1.5. The effects of martensite	103
7.1.6. The role of crack initiation	103
7.2. Conclusions	104
7.3. Recommendations	105
A. Supplementary Figures to Chapter 4	109
Acknowledgements	127
Curriculum Vitæ	129
List of Publications	131

SUMMARY

Advanced High Strength Steels (AHSS) are essential to reduce weight and consequently CO₂ emissions in the automotive industry. However, they are vulnerable to Hydrogen Embrittlement (HE), because many strengthening mechanisms present in their microstructures are also a cause of HE. The contributions of individual microstructural features to HE is not yet completely understood. Several challenges occur when studying HE in these steels. Firstly, since all strengthening mechanisms interact with hydrogen, isolating the effect of singular features is complicated. Moreover, HE is a time-sensitive phenomenon which requires experimental setups that minimise time between hydrogen charging, testing and measuring in order to avoid desorption between steps. Two types of iso-parametric microstructures were created for this project, in order to isolate the effect of individual features. Firstly, ferritic steels containing either Vanadium Carbide (VC) or Titanium Carbide (TiC) nano-precipitates of different size distributions since the addition of nano-precipitates is a promising candidate to provide both strength and ductility. Secondly, Dual Phase (DP) steels with varying amounts of martensite in a ferrite content, since these steels are the most widely used in the automotive sector.

This research begins by subjecting nano-precipitate strengthened steels to annealing treatments designed to achieve two distinct precipitate size distributions. A 2 hour heat treatment leads to precipitates of around 10 nm in size, that grow to more than 10 nm after 20 hours. Heat treatments are performed in either N₂ or H₂ gas in order to provide both a reference steel as well as one that charges the precipitates with hydrogen. After hydrogen contents were measured using Thermal Desorption Spectroscopy (TDS), the hydrogen gas is found to predominantly charge large incoherent precipitates with hydrogen. These precipitates of sizes larger than 100 nm are present in the microstructure from the steelmaking process. Smaller (semi-)coherent carbides with sizes on the order of 10 nm are not observed to contain hydrogen after the treatment. Hydrogen trapped in incoherent precipitates is trapped irreversibly in carbon vacancies inside the precipitate bulk, meaning that it does not diffuse throughout the steel. The activation energies could only be determined for TiC precipitates, which range from 69 kJ/mol to 115 kJ/mol. This type of trapping inhibits accumulation of hydrogen at critical areas such as crack tips, which means that no HE is observed in these specimens. Secondary Ion Mass Spectrometry was performed to visualise hydrogen trapped in the incoherent precipitates. Hydrogen in the TiC precipitates is primarily stored at the interface with the matrix, whereas in VC precipitates it is distributed throughout the entire bulk. This is explained as an effect of a higher C-vacancy concentration in VC.

In order to also fill (semi-)coherent precipitates with hydrogen, the four precipitate steels were also charged electrochemically. This was performed in-situ during Slow Strain

Rate Tensile (SSRT) tests at room temperature. The steels that contain the smaller precipitates were found to contain most hydrogen, which indicates that the precipitate interface is the most important trapping site. These precipitates, with sizes around 10 nm, trap hydrogen mainly inside C-vacancies on the coherent interface with activation energies of around 15 kJ/mol, whereas their larger but still semi-coherent counterparts trap inside misfit dislocation on the interface with energies of around 30 kJ/mol. Since these activation energies are low, hydrogen diffuses to critical areas and HE is observed in the SSRT tests. With the exception of the TiC steel containing larger precipitates, all steels lose around 15% of their ductility after being charged with hydrogen. The VC steel with the smallest 10 nm precipitates performs best since it retains the highest strength and ductility in a hydrogen environment. Through combined analysis using Scanning Electron Microscopy (SEM), Electron Back Scattering Diffraction (EBSD) and Electron Dispersive Spectroscopy (EDS), higher embrittlement in the steel with the largest TiC precipitates is shown to be an effect of the presence of precipitates on grain boundaries. These precipitates are theorised to cause dislocation pile-up at grain boundaries, which attracts hydrogen and subsequently causes accelerated intergranular fracture. As a result, this TiC steel is the only one that shows accelerated necking in the tensile curve. All other steels only show signs of embrittlement after the onset of necking, which suggests an important role of high plastic deformation for the HE mechanisms in these steels.

The effects of plastic deformation are further investigated by deforming the TiC steel with the smallest precipitates to predetermined levels of plastic strain, both before and during hydrogen charging. Dislocation densities are obtained using X-Ray Diffraction (XRD), and compared to the hydrogen content. A linear correlation between the dislocation density and hydrogen content is established, from which the hydrogen content in non-dislocation traps such as lattice sites, grain boundaries and precipitates is determined. This is found to be 0.72 wppm, which is only a small part of total hydrogen contents of 2.36 wppm at 0% and 3.69 wppm at 3% plastic deformation. Precipitates are therefore found to only be of minor influence to hydrogen trapping in these steels, especially after the onset of plastic deformation. After hydrogen charging, the pre-deformed steels are fast fractured to investigate the effects of hydrogen during early deformation stages on the extent of HE. Only minor embrittlement of approximately 10% is discovered, compared to 60% for specimens that were not pre-strained but only subjected to SSRT. This indicates that hydrogen exposure in the later stages of plastic deformation plays a pivotal role in HE of these steels. Post-mortem observations furthermore show that fracture initiation happens around 1% of plastic deformation for the steel. This has no effect on pre-strained specimens, since the crack tip is shielded from the electrolyte during the majority of the test duration. On the other hand, the crack tip is constantly exposed during the SSRT tests. This is the reason that HE is much more severe in the SSRT specimens, although the exposure to the hydrogen environment is only half as long. This finding serves as an important indicator that exposure of micro-cracks to the hydrogen environment is more important for HE in these steels than an elevated hydrogen content in the specimen bulk.

The following study shifts the focus from nano-precipitates to the role of martensite

in a ferritic matrix. The effects of martensite are investigated by subjecting DP steels with varying martensite contents to in-situ SSRT testing. Characterisation of grain size and ferrite/martensite (F/M) interphase area is performed using Optical Microscopy (OM), SEM and EBSD, which shows that the F/M interphase increases with the increase in martensite content. Kernel Average Misorientation (KAM) measurements indicate a plastic strain localisation around the F/M interphase boundary, which is the main trap for hydrogen in these steels. Fracture initiation occurs on this boundary, and propagates through connected martensite grains. This means that high martensite content steels show a higher degree of HE, although it reaches a maximum from a martensite content of 50%, where the extent of HE results in 80% ductility loss. Cross-sectional SEM and fractographic observations show that brittle crack initiation occurs within martensite that is present on the surface. Because of an anisotropic banded martensite configuration as a result of the rolling process of these steels, preferential fracture propagation along the rolling plane is observed.

In summary, this thesis demonstrates that plastic deformation localisation plays an important role in the HE related fracture in all examined steels. Furthermore, early brittle crack initiation is found to be an important factor in fracture, especially when these cracks remain exposed to the hydrogen environment. The presence of sub 10 nm sized VC precipitates is shown to be an effective way of increasing the strength of steels and its H absorption capacity without increasing its susceptibility to HE. In DP steels, decreasing the amount of martensite present on the surface may yield improvements in HE resistance. These findings lead to some concise recommendations for designing steel with improved HE resistance.

SAMENVATTING

Geavanceerde Hogesterktestalen (Advanced High Strength Steels, AHSS) zijn essentieel om het gewicht en daarmee ook de CO₂ uitstoot van de automobielsector te verminderen. AHSS zijn echter vatbaar voor waterstofverbrossing (Hydrogen Embrittlement, HE), omdat veel mechanismen die voor sterkte in het staal zorgen, tegelijkertijd HE kunnen veroorzaken. De individuele bijdrage die verschillende microstructurele kernmerken aan HE leveren, wordt echter nog niet voldoende begrepen. Er zijn verschillende uitdagingen voor het bestuderen van HE. Allereerst is het isoleren van de bijdrage van individuele kernmerken ingewikkeld, omdat meerdere versterkende kernmerken tegelijk optreden, en deze allemaal beïnvloed worden door waterstof. Daarnaast is HE een tijdsgebonden fenomeen, waardoor het essentieel is om testopstellingen te gebruiken die de tijd tussen het beladen met waterstof, het testen van het materiaal, en het meten van de waterstofconcentratie minimaliseren. Dit voorkomt waterstofdesorptie tussen de stappen door. In dit project zijn er twee soorten isoparametrische stalen gemaakt om het effect van individuele kernmerken zoveel mogelijk te isoleren. De eerste soort is een ferritisch staal dat ofwel vanadium carbide (VC), ofwel titanium carbide (TiC) nanoprecipitaten van verschillende grootten bevat. Het toevoegen van precipitaten is een veelbelovende strategie voor het verhogen van zowel de sterkte, als de rekbaarheid van het staal. Daarnaast zijn er ook tweefase stalen (Dual Phase, DP) gefabriceerd met verschillende hoeveelheden martensiet, omdat deze stalen breeduit in de sector gebruikt worden.

Het onderzoek begint met het blootstellen van de precipitaathoudende stalen aan gloeibehandelingen die ontwikkeld zijn om twee verschillende grootteverdelingen van precipitaten te realiseren. Een behandeling van 2 uur creëert precipitaten van 10 nm groot, die na 20 uur uitgroeien tot meer dan 10 nm. De warmtebehandelingen worden in N₂ of H₂ gas uitgevoerd, zodat er een staal wordt gemaakt waarin de precipitaten waterstof bevatten, maar er ook een referentiestaal is. Uit thermische desorptiemetingen (TDS) blijkt dat het waterstofgas voornamelijk grote incoherente precipitaten belaaft met waterstof. Deze precipitaten van 100 nm of groter zijn al vanaf het gietproces in het staal aanwezig. Kleinere (semi-)coherente precipitaten met groottes rond de 10 nm worden daarentegen na deze behandelingen niet met waterstof beladen. De waterstof die opgeslagen wordt in de incoherente precipitaten is onomkeerbaar gebonden in open koolstofvacatures binnenin de precipitaten, wat betekent dat het niet door het staal diffundeert. De activeringsenergie van waterstof in de precipitaten kan alleen bepaald worden voor TiC precipitaten, en ligt tussen de 69 kJ/mol en 115 kJ/mol. Dit soort sterk gebonden waterstof voorkomt dat waterstof in kritieke locaties zoals de scheurpunt terecht komt, waardoor er in deze stalen geen HE wordt waargenomen. Secundaire Ionen Massaspectrometrie (SIMS) wordt gebruikt om waterstof te visualiseren die opgenomen is in incoherente precipitaten. Waterstof in TiC precipitaten wordt vooral opgeslagen

in de buurt van het grensvlak met de matrix, terwijl die in VC precipitaten verdeeld is over de hele precipitaten. Dit wordt verklaard als een effect van een hogere concentratie koolstofvacatures in VC precipitaten.

Om ook (semi-)coherente precipitaten te kunnen beladen met waterstof, worden de vier precipitaathoudende stalen ook elektrochemisch beladen. Dit wordt in-situ gedaan tijdens het testen van proefstukken in een trekproef met lage reksnelheid (Slow Strain Rate Tensile, SSRT) op kamertemperatuur. De stalen die kleinere precipitaten bevatten, namen de meeste waterstof op, wat aantoont dat het grensvlak van precipitaten en de matrix de voornaamste plek is waar waterstof opgeslagen wordt. Deze precipitaten van rond de 10 nm groot binden waterstof voornamelijk in koolstofvacatures op het coherente grensvlak met activeringsenergieën rond de 15 kJ/mol, terwijl de grotere, maar toch semi-coherente precipitaten waterstof in zogenoemde 'misfit' dislocaties met energieën rond de 30 kJ/mol binden. Omdat waterstof daar zwak gebonden is, diffundeert het naar kritieke punten in de microstructuur, en wordt er HE waargenomen tijdens de SSRT tests. Met uitzondering van het TiC staal met grotere precipitaten, verliezen alle stalen ongeveer 15% van hun rekbaarheid. Het VC staal met de kleinste precipitaten presteert het beste tijdens de test, omdat deze zowel de hoogste sterkte, als de hoogste rekbaarheid behoudt. Door een gecombineerde analyse van Rasterelektronenmicroscopie (Scanning Electron Microscopy, SEM), Elektronen Terugverstrooiings Diffractie (Electron Backscattering Diffraction, EBSD) en Elektronen Dispersieve Spectroscopie (EDS) wordt aangetoond dat de hogere verbrossing van het TiC staal met de grootste precipitaten een gevolg is van de aanwezigheid van precipitaten op korrelgrenzen. Deze lijken een ophoping van dislocaties rond de korrelgrenzen te creëren, die waterstof aantrekt en daardoor versnelde interkristallijne breuk veroorzaakt. Daardoor is dit TiC staal het enige staal dat versnelde insnoering vertoont tijdens de trekproef. Alle andere stalen vertonen slechts na het punt van insnoering tekenen van verbrossing, wat suggereert dat grote hoeveelheden plastische vervorming een grote rol spelen bij HE in deze stalen.

De effecten van plastische vervorming worden verder onderzocht door het TiC staal met de kleinste precipitaten bloot te stellen aan verschillende vooraf bepaalde hoeveelheden plastische rek, zowel voor als tijdens het beladen met waterstof. Dislocatiedichtheden zijn bepaald via Röntgendiffractie (X-ray Diffraction, XRD) en vergeleken met de hoeveelheden opgenomen waterstof. Er wordt een lineair verband gevonden tussen beiden, waaruit de hoeveelheid waterstof die op plekken gebonden zit die geen dislocaties zijn, zoals korrelgrenzen en precipitaten, is bepaald. Deze hoeveelheid is 0.72 wppm, wat maar een klein deel is van de totale hoeveelheid waterstof van 2.36 wppm bij 0%, en 3.69 wppm bij 3% plastische vervorming. Precipitaten hebben dus maar een kleine invloed op de opname van waterstof in deze stalen, zeker wanneer plastische vervorming optreedt. Nadat er beladen wordt met waterstof, worden de vervormde stalen snel gebroken om de invloed van waterstof die opgenomen wordt tijdens het begin van vervorming op de uiteindelijke hoeveelheid HE te bepalen. Hier wordt een verbrossing van 10% gevonden, wat laag is vergeleken met de 60% verbrossing van stalen die continu aan een SSRT test blootgesteld worden. Dit betekent dat blootstelling aan waterstof tijdens de late stadia van vervorming een kritieke rol speelt voor HE in deze stalen. Verder wordt er via

post-mortem observaties ook ontdekt dat er breuk initiatie ontstaat rond 1% plastische rek. Dit heeft geen effect op de vooraf gerekte proefstukken, omdat de scheurpunt van het elektrolyt afgeschermd wordt tijdens de rest van de test, dit in tegenstelling tot de volledige SSRT proeven waar de scheurpunt constant wordt geopend. Hierdoor is de hoeveelheid HE in de SSRT proefstukken hoger, terwijl ze maar de helft van de tijd aan waterstof worden blootgesteld. Deze waarneming is een belangrijke indicatie dat het blootstellen van microscheuren aan de waterstofomgeving meer bijdraagt aan HE in deze stalen dan een hoger waterstofgehalte in het materiaal zelf.

Hierna wordt de focus van het onderzoek verplaatst van nano-precipitaten naar de rol van martensiet in een ferritische matrix. De effecten van martensiet worden onderzocht door DP stalen met verschillende martensietgehalten bloot te stellen aan in-situ SSRT tests. Karakterisering van korrelgrootte en ferriet/martensite (F/M) grensvlak wordt gedaan met Optische Microscopie (OM), SEM en EBSD, waaruit blijkt dat het F/M grensvlak groter wordt met een toenemend martensietgehalte. Kernel Gemiddelde Misorientatie (Kernel Average Misorientation, KAM) metingen tonen aan dat plastische vervorming zich lokaliseert rond het F/M grensvlak, waardoor dit de voornaamste locatie wordt voor het opnemen van waterstof in deze stalen. Breuk begint op dit grensvlak, en beweegt zich daarna door verbonden martensietkorrels heen. Dit betekent dat stalen met een hoger martensietgehalte meer HE vertonen, tot een martensietgehalte van 50%, waar de HE een maximum bereikt van 80%. SEM en breukobservaties van doorsneden tonen aan dat er brosse breuk initiatie voorkomt in martensietkorrels aan het oppervlak van het staal. Door een anisotrope verdeling van martensiet rond de banden in de walsrichting van het staal, heeft de breuk een voorkeur om door het walsvlak te groeien.

Dit onderzoek wijst uit dat plastische vervorming een belangrijke rol speelt bij HE gerelateerde breuk in alle onderzochte stalen. Daarnaast wordt er aangetoond dat brosse breuk initiatie een belangrijke factor is voor breuk, met name als scheuren blootgesteld blijven aan een waterstofomgeving. Het toevoegen van VC precipitaten met afmetingen van minder dan 10 nm is een effectieve manier om zowel de sterkte, als de waterstof-opnamecapaciteit van stalen te vergroten, zonder de vatbaarheid voor HE te verhogen. In tweefase stalen kan het verminderen van martensiet op het oppervlak een toename in HE-bestendigheid realiseren. Deze waarnemingen worden samengevat in een aantal aanbevelingen voor het ontwerpen van stalen met een betere resistentie tegen HE.

1

INTRODUCTION

1.1. MOTIVATION FOR THIS PROJECT

The automotive industry is a considerable contributor to global CO₂ emissions, as shown in Figure 1.1. With an increasing amount of SUVs entering the passenger vehicle market, see Figure 1.2, average car weight has been increasing in recent years and the total CO₂ emissions of the sector are still rising [1]. 75% of the fuel consumption of modern cars is related to vehicle weight, of which 40% is constituted of the car body and interior [2–4]. Reducing vehicle weight will therefore lead to CO₂ reductions, but this has to be done without compromising passenger safety. For this reason, this industry has been on the forefront of developing and using (Advanced) High Strength Steels (AHSS) in vehicles, which consist of steels with a tensile strength of 400 MPa and above [5]. Higher strength steels allow for critical parts in the vehicle to be manufactured from thinner material, which reduces the weight of the vehicle while retaining good mechanical properties to guarantee safety [6, 7]. A good example is the 2020 Toyota Highlander, which was made larger, but 100 kg lighter than its predecessor, largely an effect of the use of more AHSS [8].

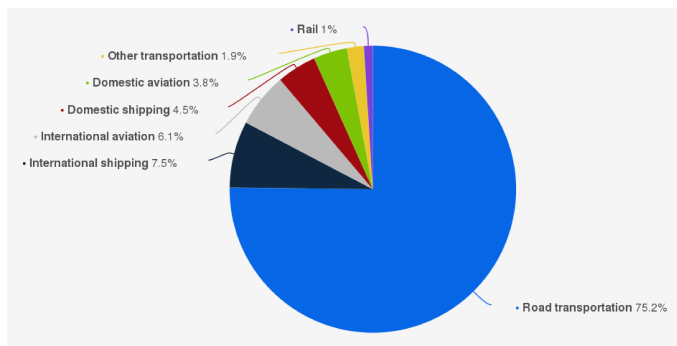


Figure 1.1.: Worldwide CO₂ emissions by the transport sector in 2023 [9].

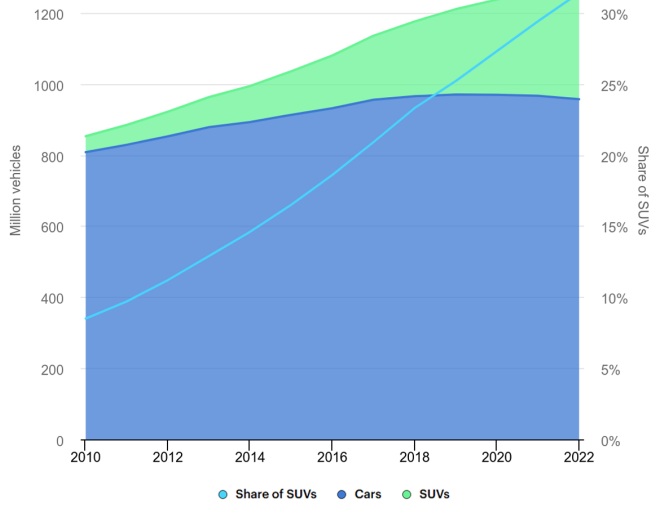


Figure 1.2.: The total amount of vehicles globally, and the percentage of CO₂ emissions that an increasing amount of SUVs brings [1].

The most commonly used AHSS are Dual-Phase (DP), Complex Phase (CP), Transformation Induced Plasticity (TRIP) and Twinning Induced Plasticity (TWIP) steels, all of which consist of intricate multi-phase microstructures in order to obtain both a high strength and ductility [3]. Dual-Phase (DP) steels are most commonly used, and make up around a third of the body-in-white of a modern car chassis [10]. They are used in various components such as panels, pillars and shock reinforcement parts [11]. A problem that grows in severity with the invention of stronger steels, however, is that they are more susceptible to Hydrogen Embrittlement (HE) [12–17]. Hydrogen Embrittlement is the observed reduction in mechanical properties of steels as a result of hydrogen present inside the steel, originally described by Johnson in 1875 [18]. For stronger steels, like AHSS, this can result in a significant reduction in both ductility and strength. Needless to say, such a reduction in properties poses a substantial problem for the implementation of steels in load bearing and forming operations. An example of this process is seen in AHSS in the form of edge cracking [19], which refers to the cracks that initiate on the sheared edges of AHSS plate steel after forming. While cracks are not present when the plate is being formed, elastic springback when it is released from the die can cause cracking. This is often an effect of delayed hydrogen accumulation in the zones of high plastic deformation [20]. Critical zones for hydrogen accumulation can also be other features, such as hard phases, interfaces or regions of stress concentrations [21–24].

1.2. MATERIALS CHALLENGES

There are several characteristics that make research into HE of AHSS a challenge. These are outlined in this section, which creates a framework in which research objectives were established.

1.2.1. DETRIMENTAL STRENGTHENING MECHANISMS

The microstructure of a high strength steel often combines multiple types of hardening mechanism in order to obtain its strength. Mechanisms like grain refinement, inclusion of multiple phases, solid solution strengthening or precipitation hardening are used in combination to obtain high strength while retaining ductility. However, these mechanisms can also be detrimental to the HE performance of a steel, and the role of individual features in HE related fracture is not yet fully understood [12, 15, 25]. The challenge resides in the fact that all microstructural features interact with, or trap, hydrogen. The main feature studied in literature that can be capable of providing both strength and HE resistance is the presence of nano-carbides within the matrix. Several studies have analysed the trapping capability of nano-carbides and the effects of size and distribution in the past [22, 26, 27]. They have not, however, correlated the trapping behaviour to the macroscopic HE behaviour of the tested steels.

The AHSS that is most used in car bodies, DP steel, obtains its high strength from a high content of martensite. The steels, however, were shown to be susceptible to HE to a large extent because of the strain partitioning on the ferrite/martensite interphase [28]. Cracking often initiates on this boundary because the localised zones of large plastic deformation attract high local hydrogen concentrations. The content of martensite within the matrix therefore has a pronounced effect on the susceptibility to HE. Davies observed a plateau in the extent of HE above 30% martensite content [29], but Wang et al. did not [28]. They mention the continued redistribution of hydrogen from the interphase to the martensite even after the martensite content rises above 30%. The exact role of the strain partitioning and H redistribution in DP steels with different martensite contents is still unknown.

Furthermore, the fact that AHSS often incorporate more strengthening mechanisms at once means that it becomes difficult to isolate the effect of a single microstructural feature on HE. The solution to this challenge would be to engineer a set of iso-parametric steels that are mostly similar in microstructure except for a single feature. Two types of iso-parametric steels will be discussed in this thesis: one containing different types of precipitate, and another containing varying amounts of martensite. This process starts with selection of alloys with carefully engineered contents that allow for creation of iso-parametric microstructures.

1.2.2. TIME-DEPENDENT BEHAVIOUR

A challenge that was already touched upon is the effect of delayed onset cracking, which is a result of the high diffusivity of hydrogen in ferrite even at room temperature.

1 Hydrogen continuously diffuses throughout the microstructure, and can absorb into or desorb from steels in a matter of minutes [30]. Knowing exactly where hydrogen resides can only be determined through modelling, by post-mortem examination of fracture features, or by analysing in a controlled environment that limits diffusion. One way to circumvent the issue of hydrogen desorption from the steel is to perform testing in-situ in a hydrogen charging environment, and developing a method of analysis that does not allow for hydrogen desorption in between charging, testing, and measuring. The type of charging environment significantly influences the resulting hydrogen distribution in the steel. Choosing the right charging condition for the envisioned research or application is therefore essential, but not straightforward since their effects are not yet fully understood.

1.2.3. NANO-SCALE INTERACTIONS

Perhaps the most challenging aspect of HE research is the nanoscopic scale of the interaction between hydrogen and steel. Observing hydrogen in its trapping location is only possible in a handful of technologies such as Atom Probe Tomography [31] or Secondary Ion Mass Spectrometry [32, 33]. However, these techniques require lengthy sample preparation that excludes the possibility of observing quickly diffusible hydrogen. Other techniques like Thermal Desorption Spectroscopy can be performed quickly after charging, but only make macro-scale hydrogen content measurements without a good spatial resolution [22, 34]. It is therefore very challenging to investigate the interaction between hydrogen and dislocations, for example, since their interaction is weak enough to allow hydrogen desorption at room temperature [35]. Nevertheless dislocations play an important role in hydrogen trapping and hydrogen related fracture mechanisms [25], which means they are an important area of research.

1.3. RESEARCH OBJECTIVES AND THESIS OUTLINE

This thesis presents a body of work aimed at understanding the effect of different microstructural features of high strength steels on their susceptibility to HE. Firstly, a theoretical background for the topic of HE is established in Chapter 2. For the rest of this thesis, two microstructural features within a ferritic matrix were focused on specifically: nano-precipitates and the martensitic phase. Iso-parametric steels were created to investigate both features as independently of other features as possible. The first is a single phase ferritic steel with nano-carbide precipitates to provide strengthening while retaining ductility. The second is a DP steel consisting of a ferritic matrix with varying martensite content. This thesis aims at understanding:

1. The effect of size and type of nano-precipitates on HE.
2. The effect of different charging environments on precipitate hydrogen trapping.
3. The effects of plastic deformation on HE.
4. The effects of different martensite concentrations on HE in DP steels.

Research into the first two objectives was combined into two chapters in this thesis; Chapter 3 and Chapter 4. Chapter 3 describes research performed on two types of nano-precipitate, TiC and VC, which were varied in size and morphology through annealing heat treatment. The precipitates present in a fully ferritic matrix provide a good iso-parametric steel for isolated study and comparison of the precipitates and their role on HE. In Chapter 3, these steels are charged with hydrogen in high temperature hydrogen gas. The absorption of hydrogen into larger incoherent precipitates is discussed, as well as its effect on HE of these steels. In Chapter 4, the same steels are charged in-situ in a mechanical test setup including electrochemical charging to charge smaller precipitates with hydrogen. The chapter discusses the effect of smaller (semi)-coherent precipitates on hydrogen absorption and trapping, and their effect on HE. It also compares the results to those obtained in the previous chapter. The third objective is the topic of Chapter 5, which discusses the effects of elastic and plastic strain on the hydrogen uptake and the related HE susceptibility a TiC containing steel. The effect of martensitic content in DP steels has been investigated in Chapter 6. Fractographic analysis is performed and related to specific distribution of martensite within the microstructure, which affect HE behaviour.

Finally, the overarching findings regarding HE in AHSS are discussed in Chapter 7, including relevant conclusions and recommendations for future research and steel design for HE resistance.

2

THEORETICAL BACKGROUND

This chapter aims to establish a theoretical background for the phenomenon of Hydrogen Embrittlement (HE), limiting itself to the topics that are required for understanding the matter presented in this thesis.

2.1. HYDROGEN ABSORPTION

Hydrogen Embrittlement can occur when hydrogen is absorbed into a steel from any kind of environment that holds hydrogen. Common examples are pipes used for high temperature steam transport[36], linepipe steels for sour service conditions [37, 38] or steels subjected to cathodic protection as a corrosion inhibition mechanism [39]. The main environments for hydrogen absorption in AHSS could be either the hot rolling and annealing, or coating steps during production, service conditions where high temperature water vapour is present, or a fractured coating causing exposure to a corrosive environment [14]. In lab settings, the amount of absorbed hydrogen can be controlled by applying a cathodic potential or current to a steel submerged in electrolyte, which changes the amount of hydrogen created on the surface. Popular electrolytes are H_2SO_4 solutions to create a low pH solution and force hydrogen reduction through Equation 2.1[40, 41], NaCl solutions for a neutral pH solution [42, 43], or NaOH solutions for a high pH electrolyte [42, 44, 45]. In case of neutral or high pH environments, water reduction is used as the mechanism for hydrogen adsorption instead of hydrogen ion reduction. This is shown in Equation 2.2.



Hydrogen that is adsorbed onto the surface through electrochemical reduction can either absorb further into the microstructure (Eq. 2.3) or recombine to form H_2 gas (Eq. 2.4). To avoid excessive gas formation, recombination poisons are added to the electrolyte. The most popular recombination poisons in literature are thiourea

(CH₄N₂S) [40, 46, 47] and ammonium thiocyanate (NH₄SCN) [48–51]. When steels come into contact with gaseous hydrogen, the equilibrium between both sides of Equation 2.4 becomes important for hydrogen absorption. For diatomic gases such as H₂, this equilibrium was first described by Sievert [52] but further described by Hirth [53] as

$$c_0 = 0.00185\sqrt{P} \exp\left(\frac{-3440}{T}\right) \quad (2.5)$$

where c_0 is the atom fraction of adsorbed atomic hydrogen at the surface, P is the hydrogen gas pressure in bar or 0.1 MPa and T is temperature in K. When hydrogen has sufficient time to homogenise throughout a specimen, the concentration c_0 is equivalent to the equilibrium concentration throughout the bulk, not taking into account trapping by defects such as dislocations. It is possible to simulate gaseous hydrogen charging through electrochemical means, but this is highly dependent on parameters such as surface oxides, surface roughness and microstructure [42]. Electrochemical charging easily leads to hydrogen concentrations that require the equivalent of several hundred bars of gas to reach, which generally leads to significantly higher hydrogen contents after electrochemical charging [54].

Hydrogen that is absorbed into the microstructure preferentially occupies certain sites. These sites are graphically represented in Figure 2.1 which shows the transition from hydrogen adsorbed in surface sites in 2.1a towards different types of hydrogen traps throughout the microstructure in 2.1b. A distinction is often made in literature between two different kinds of traps. These are called strong and weak traps, deep and shallow traps, or irreversible and reversible traps [25]. The depth, or strength, of a trap is usually denoted by the energy level of the hydrogen in the trap relative to that when it resides in an interstitial lattice site. This is visually represented in Figure 2.2. There is no clear physical distinction between a shallow and deep trap. In practice, however, a distinction is often made between reversible and irreversible traps at a fixed trapping energy. Maroef et al. state a well-defined trapping energy of 60 kJ/mol as the distinction between reversible and irreversible trapping [55]. Dadfarnia et al. select a wider distinction by designating trapping energies of less than 30 kJ/mol as reversible, and more than 60 kJ/mol as irreversible [56]. This is more in line with findings by Castaño-Rivera et al. who calculated a threshold of 35 kJ/mol below which traps are reversible, and 65 kJ/mol above which they are irreversible [57]. Some microstructural features can have different trap energies that lie in between these two values. The difference between specific features is discussed in Section 2.3.

2.2. MECHANISMS OF HYDROGEN EMBRITTLEMENT

Trapped hydrogen can damage the microstructure and cause embrittlement, but the exact mechanism by which this happens is a topic of ongoing debate. Several mechanisms have been proposed that either individually or simultaneously act to cause embrittlement. The most relevant ones to this thesis are the following:

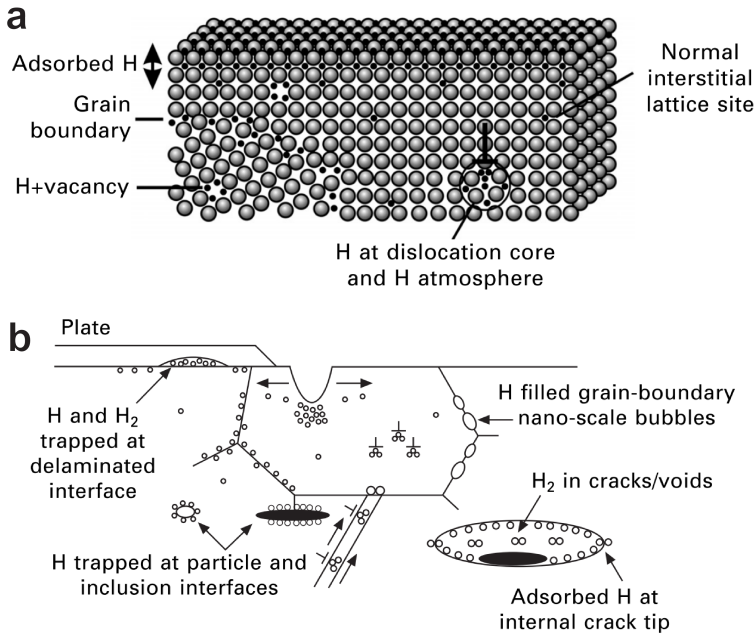


Figure 2.1.: Graphical representation of different hydrogen traps in the microstructure on a) nano and b) microscopic scale. Adapted from [25].

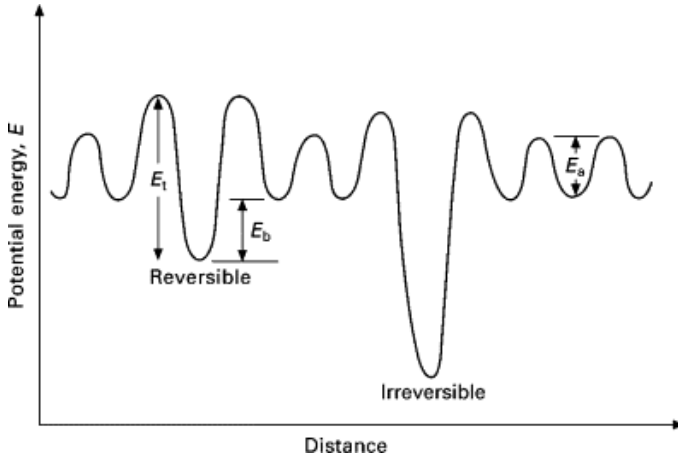


Figure 2.2.: Representation of hydrogen trap depth [58]. E_a , E_b and E_t are the lattice activation energy, trap binding energy and trap activation energy, respectively.

- Hydrogen Enhanced Decohesion (HEDE) is related most closely to the macroscopic observations of HE. Troiano put forward the theory that interstitials

of any kind, including hydrogen, can cause rapid delayed failure if a sufficient incubation time and stress are present [59]. Oriani and Josephic postulate a similar decohesion theory in 1974[60]. They find an intergranular (IG) fracture surface of a high strength steel after they charge it with hydrogen and subject it to high stress, showing that decohesion preferentially happens at grain boundaries or other phase boundaries when a critical hydrogen concentration is reached. The HEDE mechanism has been experimentally observed to cause decohesion at grain boundaries in for example nickel [61], austenite [62] and ferrite [63]. In high strength steels, HEDE is often found along grain phase boundaries between martensite and austenite [64], martensite and ferrite [65], but also within martensite grains along boundaries between α martensite and strain induced ϵ martensite [66]. Grain boundary inclusions have also been characterised as important sites for the onset of decohesion [22, 35, 67, 68].

- Hydrogen Enhanced Localised Plasticity (HELP) was first proposed by Beachem in 1972 to explain dimples on the fracture surfaces of specimens fractured in hydrogen environments [69]. Beachem states that "instead of hydrogen locking dislocations in place, it unlocks them and allows them to multiply or move at reduced stresses.". Proof of this model came in 1999 when Robertson provided experimental evidence that introduction of hydrogen to a steel both speeds up moving dislocations and unlocks dislocations that were previously pinned [70]. Both effects were found to be reversible upon the removal of the hydrogen, pointing to the influence of diffusible (reversibly trapped) hydrogen. More recently, Martin, Robertson and Sofronis provided high resolution SEM images of flat hydrogen related fracture surfaces, showing the presence of dimples on a much smaller scale than in normal ductile fracture, supporting the HELP mechanism of fracture [71]. They also show the emergence of dense dislocation structures immediately beneath a fracture surface that were previously thought to be a result of the brittle HEDE mechanism, not involving dislocation movement. Hwang and Bernstein found that dislocations play a role in transporting hydrogen [72].
- Adsorption Induced Dislocation Emission (AIDE) was suggested by Lynch after Clum coupled the adsorption of hydrogen to the nucleation of dislocations at the surface in 1975 [73–75]. Higher hydrogen concentration in the surface (and sub-surface) layers compared to the bulk facilitates dislocation nucleation, from which Lynch argues that these dislocations can easily move away from a crack tip or assist in causing nano-dimples in front of a crack tip. Lynch argued that because of the similar nature of the AIDE and HELP mechanisms, relative contributions of HELP and AIDE could not be distinguished by electron microscopy techniques of the authors trying to disprove the theory [71]. The AIDE model is still considered relevant in recent literature, but is generally regarded as being of less importance to hydrogen related fracture than the HELP and HEDE mechanisms.
- Hydrogen Enhanced Strain Induced Vacancy formation (HESIV) was proposed by Nagumo in 2004, as a model that shifts the focus from hydrogen as a cause

for fracture to hydrogen as a cause for degradation of material properties which leads to accelerated fracture [76, 77]. This model describes the stabilisation and decreased mobility of strain-induced vacancies in the steel matrix, and the reduced formation energy of vacancies when combining with hydrogen. This has been experimentally shown by for example McLellan and Xu [78]. The mechanism can occur in combination with HELP and AIDE. A larger concentration of vacancies at increasing strain is also mentioned as a reason for the increased uptake of hydrogen by steels undergoing plastic strain.

In more recent literature, it has come to light that synergistic action of multiple mechanisms is common. An overview is given in Figure 2.3 which was made by Wasim et al. in order to unify different embrittlement models [79]. This figure, describing their 'HELP + HEDE' model, shows the expected fracture surfaces and the dominance of certain fracture mechanisms as a function of hydrogen concentration. It should be noted that other ductile mechanisms such as AIDE and HESIV are not excluded by this model, but rather incorporated in the HELP term. At first, low hydrogen concentrations do not allow for sufficient hydrogen localisation to activate HEDE at interfaces, but effects of the HELP model can still be observed (2.3b). Ductile Microvoid Coalescence (MVC) fracture can be observed, but the voids are smaller compared to those without hydrogen. Higher hydrogen concentrations (2.3c) will cause appearance of Transgranular (TG) Quasi-Cleavage (QC) fracture surfaces that show first signs of brittle fracture but are still dominated by HELP and other ductile mechanisms. It is only after a certain 'critical H concentration' that brittle HEDE type fracture starts becoming dominant (2.3e). QC fracture starts appearing more frequently than MVC on the fracture surface, and a sharp drop in toughness is found [36]. If the hydrogen concentration is increased further, Intergranular (IG) fracture facets starts appearing that are a clear indication of HEDE fracture (2.3f). At the highest hydrogen concentrations, ductile mechanism related fracture surfaces are no longer observed (2.3g).

Although this model describes the overall appearance of fracture surfaces in embrittled steels, it does not give quantitative values for critical hydrogen concentrations. The term 'critical hydrogen concentration' has been used differently in literature, meaning either the general concentration in the bulk material or the localised concentration at a defect or a crack tip. The overall hydrogen concentration in the microstructure is measured most experimentally and is therefore often used as the benchmark for the onset of brittle fracture. The local hydrogen concentration at a defect, however, provides a more realistic insight into the nature of the synergistic action between multiple mechanisms. The critical local concentration necessary to initiate brittle fracture will differ depending on the nature of the location or trap, whether it is for example a grain boundary, a crack tip or the interface between a precipitate and the matrix. The nature of the trap will both govern how much hydrogen can be stored there and what the local critical hydrogen concentration is to initiate brittle fracture governed by the HEDE model.

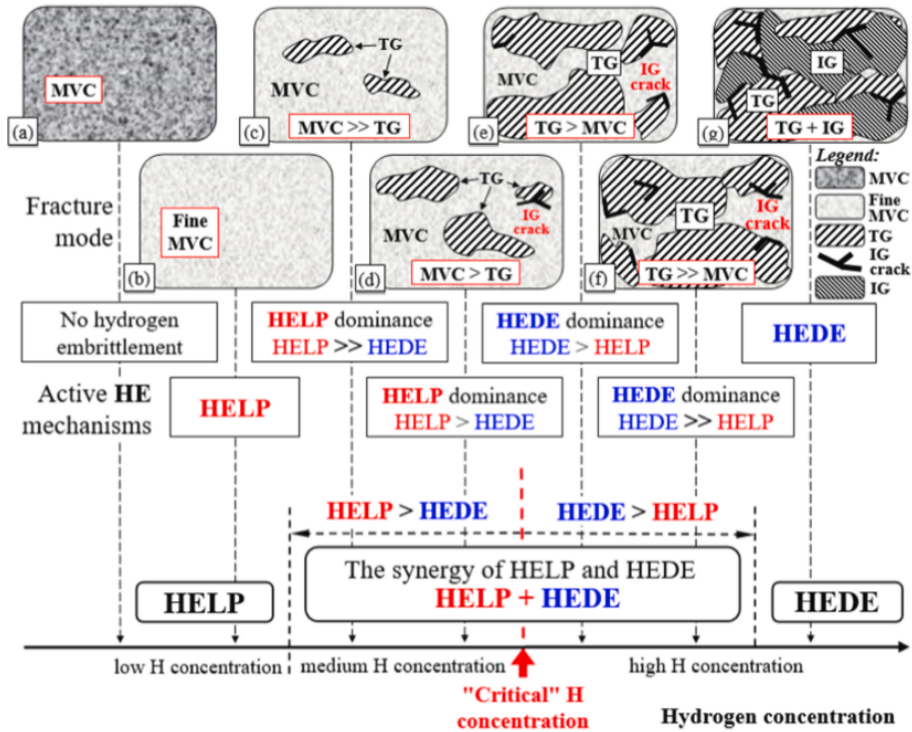


Figure 2.3.: The HELP + HEDE model as discussed by Wasim et al. [79].

2.3. INFLUENCE OF MICROSTRUCTURAL FEATURES

AHSS can feature a large variety of microstructural features that give them their range of mechanical properties. Needless to say, varying the microstructural features will alter a steel's response to hydrogen charging. An overview of the trapping energies of different microstructural features is given in Table 2.1. Not all features will be discussed here, but emphasis will be given to features that are important for the further chapters in this thesis.

2.3.1. DISLOCATIONS

Hydrogen trapping in dislocations was recognised very early on in hydrogen embrittlement research, as a large contributor to increased hydrogen uptake after plastic deformation, next to vacancy trapping [80–82]. Nagumo, Takai and Okuda, for example, perform a thermal desorption study on ferritic and eutectoid steels after hydrogen charging. They conclude that annealing reduces the amount of hydrogen absorbed in a steel compared to a cold drawn condition. Since vacancies and dislocations annihilate at different temperatures, the authors of this study manage to distinguish between trapping in these two features. The strength of

a dislocation trap can be calculated accordingly, and is reported to be around 24 kJ/mol [60, 81, 83]. Physical presence of hydrogen at dislocation cores was shown using atom probe tomography by Chen et al [84]. Ferreira, Robertson and Birnbaum experimentally show the reduction of elastic interactions between dislocations and other obstacles by introducing hydrogen into transparent TEM films and observing dislocation movement [85]. They observe the movement of stationary dislocations upon introduction of hydrogen, where the dislocations move closer towards each other and to a grain boundary in stainless steel. Closer spacing of dislocations causes a more concentrated region of plastic deformation at a similar amount of dislocations. Effect of this are reduced void size in ductile fracture and a reduced plastic zone size ahead of a crack tip, which are described in the HELP model.

2.3.2. GRAIN BOUNDARIES

Hydrogen trapping in grain boundaries is a mechanism that has often been observed experimentally as the reason for characteristic intergranular brittle fracture of steels in hydrogen. One of the reasons for the increased HE susceptibility of higher strength steels is the smaller grain size, and as such, higher grain boundary density [86]. However, not all boundaries act as similar traps. For example, Maroef et al. discuss different measurements of grain boundary trapping energy which lie in between 18 and 60 kJ/mol [55]. This means some grain boundaries can even be classified as strong irreversible hydrogen traps. In general, grain boundaries with a higher misorientation, such as random boundaries, have a higher trapping energy and are more likely to embrittle. Special Coincident Site Lattice (CSL) boundaries such as $\Sigma 3$ boundaries, often found in the form of twins [87], are weaker hydrogen traps and as such are less susceptible to hydrogen embrittlement, as shown by Bechtler et al. and Kwon et al [87, 88]. These authors managed to decrease the HE susceptibility of nickel and TWIP steel, respectively, by increasing the fraction of special boundaries.

2.3.3. DIFFERENT PHASES

HEDE fracture on grain boundaries if the boundary separates two different phases, such as martensite and ferrite [15] or martensite and austenite [64]. Although these phase boundaries do not inherently embrittle due to hydrogen accumulation, the difference in strength between the two phases can cause strain partitioning in the softer phase which increases local dislocation numbers and gives rise to void formation on the grain boundary, which also results in intergranular cracking. The difference between phases is most pronounced in DP steels consisting of soft ferrite and hard martensite. The different hardnesses of the ferritic and martensitic phases result in a pronounced strain heterogeneity upon straining. Because of ferrite's low yield strength, dislocation creation starts in this phase and dislocation pileup is observed at ferrite/martensite (F/M) interphase boundaries. The martensite only starts plastically deforming at much higher strains. Even within the ferritic phase, the plastic deformation is heterogenous, as noted by Korzekwa et al. who observed a much higher dislocation density near F/M interphases than within the internal

regions of ferrite grains [89]. Ghadbeigi et al. measured the local strain in ferrite grains using Digital Image Correlation (DIC) and measured a local strain of up to 120% in the ferrite near F/M interphases [90]. Wang et al. studied the HE of DP steels with varying martensite content [28]. Specimens with a martensite content below 40% fracture according to the ductile microvoid coalescence (MVC) mechanism. At martensite contents over 40%, fracture surfaces slowly move towards transgranular quasi-cleavage (QC) characterised by flat facets with a rough appearance, while the specimen with the highest martensite content of 95% shows clear indication of intergranular (IG) fracture. This points to enhanced hydrogen uptake for DP steels with higher martensite contents, as per the HELP + HEDE model, and a more brittle fracture behaviour. This phenomenon is explained by Momotani et al. who study hydrogen fracture in a low carbon martensitic steel [91].

2.3.4. INTERMETALLIC PRECIPITATES

A specific focus of this thesis is the effect of intermetallic precipitates on the HE behaviour of high strength steels. Precipitates are particles of a second phase within the matrix of elements that are in solid solution at higher temperatures but precipitate upon cooling of a steel [92]. Precipitate sizes range from the nanometer to micrometer scale. It was discovered early on that precipitates can have a range of trapping energies, depending on their size and coherency. Pressouyre describes the trappings created by TiC, Fe₃C and MnS precipitate interfaces as "Irreversible, gets more reversible as the particle is more coherent" [83]. The trapping energy changes because the interfaces get more coherent as the particle size decreases [93]. This was observed by Wei and Tsuzaki through TEM observations [27]. They also observed that the flat and curved sides of plate-like TiC precipitates had different coherencies, and interacted with hydrogen differently. An increase in precipitate size means a decrease in interface area for a constant volume fraction of precipitates in the specimen. However, the amount of traps in the same interface increases when the particles increase in size. Moreover, hydrogen is also trapped in the strain field that arises around the precipitate because of lattice distortion. These effects counteract each other and cause an independence on interfacial area [22]. Recent studies have been able to observe hydrogen at the atom level through techniques such as Atom Probe Tomography (APT) [31] and Small Angle Neutron Scattering (SANS) [94]. Ohnuma et al. measure the distribution of hydrogen in a steel with NbC nanoprecipitates using SANS, and conclude that the hydrogen is trapped at the first few atomic layers outside of the particle [94]. Chen et al. use APT to observe the distribution of H in and around VC precipitates [31]. They conclude that the deuterium (as a substitute for hydrogen) in their experiment is mainly located inside the bulk of the precipitates themselves, which is a possibility that Wei and Tsuzaki also discussed [27]. Whether precipitates are more likely to store hydrogen in their bulk or on the interface depends on multiple factors, including a saddle point energy that hydrogen atoms have to overcome before they can progress into the precipitate bulk [27]. Ab initio Density Functional Theory (DFT) methods are extremely useful for calculating the hydrogen trapping energies for different locations inside and around precipitates [27, 95, 96].

Table 2.1.: Comparison of different trapping densities, both experimentally and numerically obtained, found in literature.

Type of trap	Trapping energy [kJ/mol]	Steel	Reference
Matrix elements			
Interstitial	7	Ferrite	[55]
	55	Austenite	[97]
Vacancy with one or two atoms	60.7	Ferritic iron	[97, 98]
Vacancy with 3 or more atoms	41.5	Ferritic iron	[97, 98]
Dislocation	24	Fe-Ti-C alloy	[83]
Grain boundaries			
Ferrite-ferrite boundaries	24 - 33	Low alloy steel	[35]
	18 - 59	Ferritic iron	[55]
Precipitates			
Coherent TiC	42 - 59	HSLA	[24, 99, 100]
Semi-coherent TiC	55.8	Low alloy steel	[27]
Incoherent TiC	53 - 145	Low alloy steel	[22, 101, 102]
NbC bulk	63 - 68	Low alloy steel	[35]
NbC interface	23 - 48	Low alloy steel	[35]
Coherent VC	25 - 60	Low alloy steel	[26, 96, 103, 104]
Semi-Coherent VC	52 - 58	HSLA	[105]

2.4. INFLUENCE OF EXTERNAL FACTORS

Hydrogen Embrittlement is a consequence of the interaction between hydrogen and the microstructure, but the extent to which it manifests can be influenced by external parameters, that are not material characteristics.

2.4.1. SURFACE ROUGHNESS

The effect of surface roughness was studied by Van Eeckhout et al. who found that a higher roughness increases the likelihood of H₂ bubble formation at the surface, which locally inhibits hydrogen reduction [106]. A rougher surface finish (e.g. ground instead of polished) moreover creates a higher actual surface area and leaves more deformation in the sub-surface layers. These layers will contain a high density of dislocations that locally elevated trapped hydrogen, which decreases the diffusion of hydrogen through the surface layers to the bulk.

2.4.2. CHARGING ENVIRONMENT

The relation between the charging environment and the resulting hydrogen distribution in the steel is not straightforward to obtain. The most important factor to consider is the distinction between gaseous and electrochemical charging. Zhao et al. studied the effects of the charging method on the hardening or softening of a low carbon steel [54]. The authors performed electrochemical (E) charging in H_2SO_4 using As_2O_3 as a recombination poison, as well as gas (G) charging at 10 MPa, or 100 bar, and 85 °C. The hydrogen concentrations were measured afterwards using Thermal Desorption Spectroscopy (TDS). Their findings are shown in Figure 2.4, of which Figure 2.4a shows the TDS curves for the total amount of hydrogen for samples charged with both methods. The concentration after electrochemical charging is significantly higher than that after gaseous charging (3.94 vs 0.24 wppm). Furthermore, the relative distribution of hydrogen between shallow and deep traps (lower and higher temperatures) differs between charging methods. In electrochemical charging, the supply of hydrogen from the surface regions is large and deep as well as shallow traps will be filled. In gas charging, the supply is lower, which results in deep traps not being completely filled and bulk hydrogen only being present in small concentrations as can be seen in the inset in Figure 2.4a. As a result of the high absorption rates during electrochemical charging, it could be expected that a hydrogen gradient exists with decreasing concentration further into the specimen until full saturation is reached. Zhao et al. tested this by grinding away the top half of an electrochemically charged specimen before performing TDS on the remaining half. Figure 2.4b shows that the concentration of weakly trapped hydrogen in the half sample is indeed smaller when compared to a full sample. It should be noted however, that the time spent grinding as well as any heat generated during the process would also lead to hydrogen desorption from the half-thickness specimen. It can therefore not be said with certainty that their difference in concentration profile is exclusively a result of sample thickness. As long as a gradient does exist, however, it could lead to a different extent of embrittlement in the surface compared to bulk areas of a steel.

2.4.3. STRESS AND STRAIN CONCENTRATIONS

The presence of geometrical changes like sharp corners or holes can significantly alter the behaviour of a steel under load. These geometrical changes can locally elevate the stress from its nominal levels and are therefore called stress concentrators. The HE of steels can increase in the presence of stress concentrators like notches, and crack tips as an extrapolation of notches, and can cause a further deterioration of mechanical properties beyond that resulting from just the stress concentration. Hardie and Su'e studied the effect of circumferential notch geometries on the HE behaviour of a low alloy steel [107]. When tested in a hydrogen environment, the Notched Tensile Strength (NTS) dropped significantly compared to that in air. The strength of their specimens decreases with increasing stress concentration factor K_t , which is defined as the local stress level at the notch divided by the nominal stress far away from the notch. Figure 2.5 shows data from a study by Wang, Akiyama and Tsuzaki [108]. The authors modelled the local hydrogen concentrations ahead of the

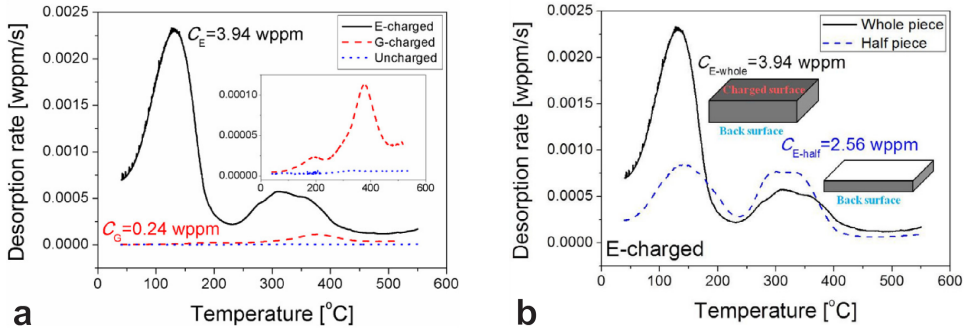


Figure 2.4.: TDS findings from a study by Zhao et al. who compared electrochemical (E) and gaseous (G) charging of hydrogen into low carbon steel [54]. a) Comparison of overall H concentrations between the two charging methods and b) comparison of a whole and half thickness specimen charged electrochemically.

notch at a stress of 0.9 times the break stress, and normalised them compared to bulk concentrations. A higher K_t creates a more localised zone of hydrostatic stress, of higher intensity, that attracts more hydrogen. The notch concentrations therefore become much higher at a K_t of 4.9 compared to 2.1 as a result of the increased local hydrostatic stresses, which lowers the NTS of the specimen. Even when a sample is pre-cracked to a theoretical K_t of infinity, the strength does not decrease further.

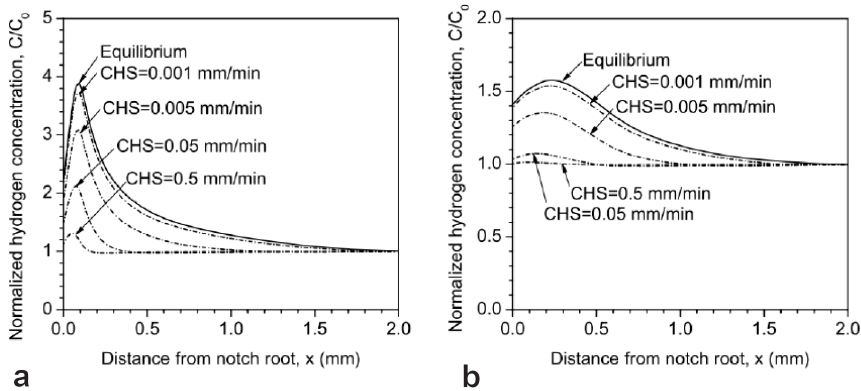


Figure 2.5.: The influence of crosshead speed (CHS) on the local hydrogen concentration ahead of the notch, as studied by Wang, Akiyama and Tsuzaki at 0.9 times the break stress of the sample [45]. (a) was calculated for $K_t = 4.9$ and (b) for $K_t = 2.1$.

Although local microstructural effects like vacancy creation upon deformation were not included in their model, the trend this figure presents is expected to be

present at all regions of hydrostatic stress. Locally high stress concentrations that are elevated above the yield strength will create zones of localised plasticity, or strain concentrations. High dislocation densities in these zones allow for higher diffusible hydrogen concentrations, which will lead to earlier fracture through the HELP, HESIV and AIDE mechanisms and cause exacerbated HE [109].

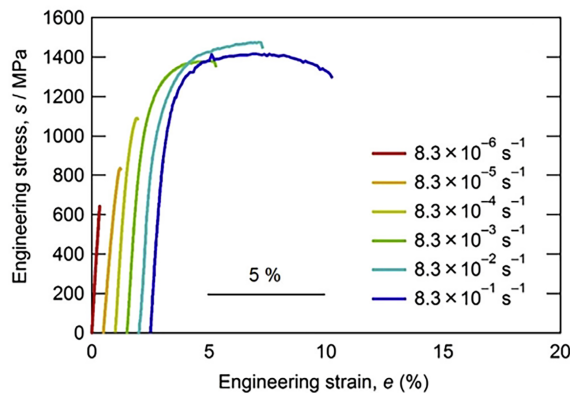


Figure 2.6.: Tensile results obtained by Momotani et al. at different strain rates in hydrogen charged low-carbon martensitic steel [91].

2.4.4. STRAIN RATE

Figure 2.5 also shows the effect of crosshead speed, or strain rate, on notched AISI 4135 steel samples tested by Wang, Akiyama and Tsuzaki [108]. After modelling the hydrogen diffusion and concentration during a tensile test, it can be seen that a lower strain rate leads to much higher local concentrations of diffusible hydrogen, which corresponded to more embrittlement in the samples. The effect of strain rate in hydrogen embrittlement is very pronounced in all steels. This is an effect that is usually caused by hydrogen diffusion during the time spent under load, whether it be in laboratory testing or during the lifetime of a part. Momotani et al. characterise the effect of strain rate on the tensile properties of a lath martensitic steel [91]. They find that tensile tests performed at a low strain rate of $8.3 \times 10^{-6} \text{ s}^{-1}$ cause a greater loss of ductility in the steel than tests performed at $8.3 \times 10^{-1} \text{ s}^{-1}$. At the lower strain rate, hydrogen has the time to diffuse towards critical areas in the microstructure, which are Prior Austenite Grain Boundaries (PAGBs) in this case. The PAGBs are weakened and cause intergranular fracture. At higher strain rates, hydrogen is still present homogeneously throughout the microstructure and fracture is largely transgranular. Figure 2.6 shows the tensile curves obtained by Momotani et al. Hydrogen embrittlement is most prevalent at lower strain rates where eventually fracture happens before the yield point.

Because of this influence of the strain rate on HE of steels, standards like ASTM G142 list acceptable ranges of strain rates to test for hydrogen embrittlement [110], so

that the extent of HE is not underestimated. For fatigue testing, this extends to a sufficiently low frequency and loading rate to allow for hydrogen diffusion towards crack tips.

2.5. SUMMARY AND CONCLUSIONS

The chapter has discussed the different aspects of hydrogen embrittlement research that are required as a background for understanding this thesis. HE is a phenomenon that acts over different time- and length scales, and is thus influenced by a range of microstructural features as well as external parameters. The contents of this chapter can be briefly summarised as follows:

1. AHSS are especially susceptible to HE because they contain a large amount of trapping features, features with a low threshold concentration such as martensite boundaries, and have a low crack propagation resistance. Most features are interlinked, meaning one cannot be changed without affecting others. This makes it especially difficult to find appropriate mitigation measures for these steels. Attempts have been made for specific microstructures, but none have so far been successful in fully eliminating HE.
2. Almost any feature has the ability to trap hydrogen with a certain strength and cause HE. This strength is called the trap density, or the trapping energy of the feature. Weak traps are also called reversible traps, and hydrogen trapped within them is called diffusible hydrogen, since they have enough energy to escape from the traps and diffuse throughout the steel at room temperature. Strong traps are called irreversible because the hydrogen within them is only released at elevated temperatures. The value that separates strong and weak traps is approximately 30 - 60 kJ/mol.
3. Hydrogen fracture is initiated when a microstructural feature reaches a critical hydrogen concentration. Often, these features are interfaces between phases, grains, precipitates or inclusions. What the required local threshold concentration of hydrogen for a particular feature is, depends on the feature and the stress state. High tensile stresses locally increase the hydrogen concentration by attracting diffusible hydrogen as a result of either stress driven diffusion, dislocation movement or vacancy creation and coalescence. Stress concentrations like notches, crack tips, or areas around precipitates or inclusions have a locally increased stress and are therefore preferred sites for crack initiation.
4. Crack propagation in a hydrogen loaded steel is often a combination of brittle and ductile-like mechanisms. Therefore the resulting fracture is often called 'Quasi-Cleavage' (QC). The crack propagation path is highly dependent on local stress state, grain orientation, grain boundary character and the presence of hydrogen trapping features. The fracture mechanism shifts between ductile and brittle mechanisms depending on whether the local critical hydrogen concentration is sufficient to initiate brittle mechanisms.

5. The distribution of hydrogen through the steel, the hydrogen concentration profile, is dependent on the charging method, time and the temperature. Differences in these factors can lead to different relative occupations of strong and weak traps, which can change the HE behaviour of a specific microstructure. When characterising the HE behaviour, appropriate charging conditions should be chosen.

3

HYDROGEN TRAPPING AND EMBRITTELEMENT OF NANO-CARBIDE STEELS AFTER GASEOUS CHARGING

**Tim BOOT, Athira SURESH KUMAR, Santhana ESWARA,
Pascal KÖMMELT, Amarante BÖTTGER, Vera POPOVICH**

This work studies the effect of TiC and VC precipitate sizes on hydrogen trapping and embrittlement. Two experimental ferritic HSLA steels containing either TiC or VC carbides for precipitation strengthening are annealed in nitrogen and hydrogen gas. This results in a hydrogen uptake of up to 0.91 and 0.44 wppm in the TiC and VC steels, respectively. TEM and TDS analysis indicate that semi-coherent TiC particles trap hydrogen in misfit dislocations with an activation energy of 43 kJ/mol. Coherent VC particles are suggested to trap hydrogen in interface carbon vacancies, with an energy between 53 and 72 kJ/mol. Carbon vacancies are the likely trapping site in incoherent precipitates, where SIMS imaging confirms that incoherent TiC precipitates trap preferentially near the interface, whereas incoherent VC precipitates trap throughout their bulk. Neither alloy is embrittled in SSRT tests after hydrogen absorption, which shows that these precipitates can be used as both a hydrogen sink and a strengthening mechanism in steels.

This chapter has been published in the Journal of Materials Science **59**, 18 (2024) [21].

3.1. INTRODUCTION

The automotive industry has been on the forefront of the search for new high strength steel grades for decades. With the development of third generation Advanced High Strength Steels (AHSS), the industry seeks to combine high strength with high ductility at a low cost. Doing so allows for creating more lightweight vehicles in order to reduce CO₂ emissions without compromising on passenger safety [3, 4, 6, 7]. However, AHSS are especially vulnerable to Hydrogen Embrittlement (HE) because their microstructural features, such as high grain boundary densities, interphase boundaries and strain induced martensite are significantly affected by hydrogen [12–16]. In the worst case, HE can manifest itself as sudden premature failure of parts.

One possible solution to HE that has received much attention is the use of carbides precipitated in the matrix as both a strengthening mechanism and a trap for hydrogen [22, 27, 34, 67, 100, 105, 111–113]. Carbides are associated with high activation energies, E_A , for hydrogen to leave specific traps and occupy different sites [58]. High activation energies decrease the overall concentration of diffusible hydrogen, which has been shown to be the main contributor to HE because it can diffuse towards critical areas in the microstructure around room temperature [34, 105, 111, 114, 115]. These critical areas can, for example, be interfaces [65] or crack tips [116], where the hydrogen contributes to crack initiation or growth, resulting in HE. Hydrogen traps associated with precipitates have been shown to have a wide range of activation energies. These vary not only between different precipitate types, but also within each type, predominantly with the precipitate size and as a consequence its coherency with the matrix.

Two of the most frequently studied precipitate types are titanium and vanadium carbides. Table 3.1 lists several values for hydrogen activation energies associated with different locations in these precipitates. TiC precipitates that are coherent with the matrix were experimentally found to have the lowest activation energies, ranging from 42 to 59 kJ/mol, which are attributed to traps at the interface between coherent TiC and the matrix [24, 99]. When the TiC precipitates reach a size of approximately 4.2 nm, the lattice mismatch between the precipitate and the matrix necessitates the creation of misfit dislocations on the precipitate/matrix interface [117]. These dislocations can also trap hydrogen, and have been shown both experimentally and numerically to have activation energies very similar to the coherent interface [27, 118]. Eventually precipitates grow to become fully incoherent with the matrix. These TiC precipitates have been shown to strongly trap hydrogen [112], with an experimentally measured activation energy of up to 145 kJ/mol [22]. Debate is still ongoing, however, about where exactly hydrogen is trapped in these carbides. Atom probe observations by Takahashi et al. suggest trapping at the interface of semi-coherent carbides [119]. Interface trapping is also suggested by several other authors in studies on larger incoherent precipitates [22, 24]. These authors observe a reduction in trapped hydrogen with increasing precipitate size as a result of a reduction in total interface area. However, Wei et al. instead postulate that the amount of hydrogen trapped in TiC corresponds to their total volume [27]. This last

finding is supported by a recent study by Vandewalle et al. who assume trapping to happen mainly at carbon vacancies in the bulk of incoherent TiC precipitates based on the larger equilibrium C-vacancy content in the bulk relative to the interface [112]. Numerical studies agree that C-vacancies in bulk TiC form good hydrogen traps, with activation energies ranging from 105 to 113 kJ/mol [96, 120]. Clearly, further investigation is required to identify the actual trapping site of H in incoherent TiC precipitates.

For VC precipitates there is more consensus on the nature of hydrogen trapping. Malard et al. performed neutron scattering experiments that suggest hydrogen trapping inside precipitates rather than at the interface [113]. This is confirmed by atom probe analysis that Takahashi et al. performed [26]. They conclude that hydrogen is stored inside the carbon vacancy on the coherent interface of small VC precipitates and find an activation energy of 60 kJ/mol. The same trapping site has been calculated numerically by several authors who find activation energies between 37 and 56 kJ/mol [103, 104]. Incoherent vanadium carbides have been shown to have an abundance of carbon vacancies, and in fact often have a different stoichiometry such as V_4C_3 or V_6C_5 [121, 122]. This abundance of vacancies creates many possible sites for hydrogen trapping. Kawakami and Matsumiya calculate an activation energy of 116 kJ/mol [95] for C-vacancies in incoherent vanadium carbides, which is a high value compared to recent studies that find between 3 and 36 kJ/mol [96, 120, 123]. These values are rather low, but could be improved by doping the precipitates with transition metals [124]. On the other hand, an experimental study by Depover et al. attributes activation energies of 62 - 67 kJ/mol to the same traps [105]. Overall, the amount of studies in literature that focus on hydrogen trapping in vanadium carbides is rather limited compared to those that study titanium carbides. To the best of the authors' knowledge, no direct evidence of trapping in incoherent vanadium carbides has been found.

Needless to say, titanium and vanadium carbides provide an interesting opportunity for study of their effects on HE. Several approaches have been taken in the literature. The most common approach is to charge a steel containing the carbides of interest using electrochemical methods at room temperature [100, 102, 105, 111]. These studies, however, fail to charge hydrogen into the bulk of incoherent precipitates since the incoherent interface creates a diffusion barrier that cannot be overcome at room temperature [22, 27, 105]. The alternative is to charge steel with hydrogen during an annealing treatment in a hydrogen containing atmosphere. This charging method is especially relevant to study hydrogen absorption during steel production stages such as hot-rolling or galvanizing, as well as the performance of steels in hydrogen storage and transport applications. However, studies that used this method of high temperature gaseous hydrogen charging mostly performed them only on large semi- or incoherent carbides [22, 100, 112]. While these precipitates enhance hydrogen trapping capacity, smaller carbides are preferred as a strengthening mechanism in steels [26, 64, 100, 126], so a trade-off between precipitate size and trapping capacity is likely required to achieve the best overall performance. A clear knowledge gap exists on the hydrogen trapping capacity of coherent or semi-coherent carbides and

Table 3.1.: Overview of different activation energies obtained from literature, converted to kJ/mol (1 eV = 96.5 kJ/mol).

Carbide	Coherency and type of trap	E_A [kJ/mol]	Type of study
TiC	Coherent precipitates	42 - 59 [24, 99, 100]	Experimental
	Coherent (Interface C-vacancy)	99 - 103 [96, 104]	Numerical
	Semi-coherent (Interface dislocation)	55.8 [27]	Experimental
		48 [118]	Numerical
	Incoherent precipitates	53 - 145 [22, 101, 102]	Experimental
	Bulk C-vacancy	105 - 113 [96, 120]	Numerical
80 - 90 [27, 112]		Experimental	
VC	Coherent (Interface C-vacancy)	37 - 56 [96, 103, 104]	Numerical
		60 [26]	Experimental
	Semi-coherent (Interface)	52 - 58 [105]	Experimental
	Bulk C-vacancy	3 - 116 [95, 96, 120, 123, 125]	Numerical
62 - 67 [105]		Experimental	

the effect thereof on the HE of their steels after high temperature charging. Therefore, this work aims to investigate the effect of the precipitate size and coherency on the hydrogen absorption and embrittlement of the TiC and VC steels after hydrogenation in a high temperature gaseous hydrogen environment.

3.2. MATERIALS & METHODS

Two experimental single-phase ferritic High Strength Low Alloy (HSLA) steels containing either titanium or vanadium carbides, were cast by Tata Steel in IJmuiden for use in this research. The compositions, shown in Table 3.2, were chosen for maximum precipitation of TiC and VC. The Ti:C and V:C atomic ratios were matched as close to 1:1 as possible to achieve this. The As-Received (AR) materials from Tata Steel were fully austenized before being hot rolled to a thickness of 3.5 mm. The slabs were cooled quickly to 630 °C after hot rolling, then subsequently cooled in a furnace to replicate slow coil cooling speeds. Hot rolling took place entirely in the austenitic region (above Ar3) with the austenite-to-ferrite phase transformation and precipitation nucleation and growth in the ferrite phase starting from the fast cooling and continuing up to the initial residence period in the furnace set at 630 °C. Both microstructures are fully ferritic except for the second phase precipitates.

Figure 3.1 shows TEM images of the TiC and VC precipitates in AR state. The TiC precipitates were found to be platelets with an average width of 6 nm and

a thickness of 2 nm. The VC precipitates also appear as platelets, with a similar width but a smaller thickness of about 1 nm. An overview of the size distribution of precipitates in both compositions is given in Figure 3.2. As can be observed in this figure, some larger precipitates were already present in both steels, but they only occur sparingly. Furthermore, both these precipitate types were found to comply with the Baker-Nutting orientation relationship (OR) ($\{001\}_{\text{carbide}} // \{001\}_{\text{ferrite}}$ & $\langle 110 \rangle_{\text{carbide}} // \langle 010 \rangle_{\text{ferrite}}$) between the precipitate and the matrix.

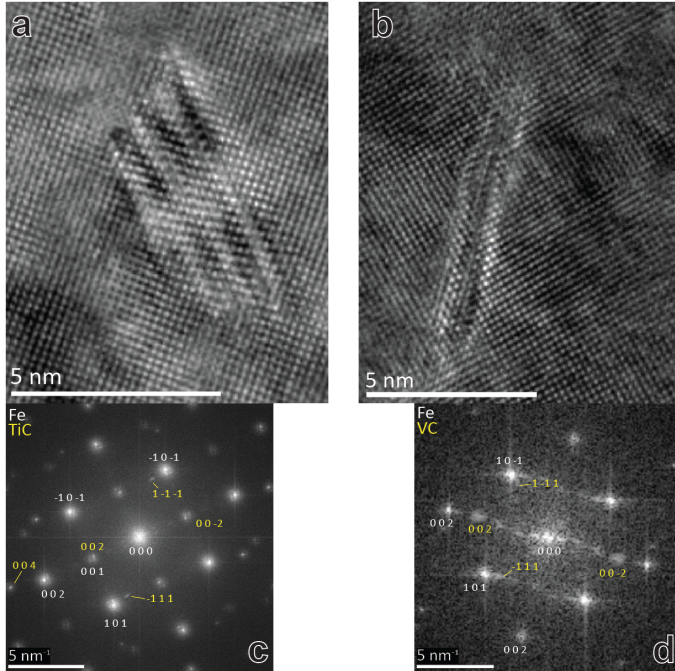


Figure 3.1.: TEM images of small precipitates in the as-received a) TiC and b) VC alloys. c) and d) show the Fast Fourier Transform (FFT) image analyses of the images in a) and b), respectively. Zone Axis $\langle 110 \rangle_{\text{carbide}} // \langle 010 \rangle_{\text{ferrite}}$ was used, which shows that $\{001\}_{\text{carbide}} // \{001\}_{\text{ferrite}}$, according to the Baker-Nutting Orientation Relationship (OR).

The steels were subjected to four different annealing heat treatments for this

Table 3.2.: Summarised alloy contents of the TiC and VC alloys in weight %, determined using X-Ray Fluorescence (XRF).

Alloy type	C	Mn	Al	Si	Ti	V	Trace elements	Balance Fe
TiC	0.07	1.7	0.01	0.01	0.30	-	0.04	97.8
VC	0.07	1.8	0.01	0.02	-	0.31	0.03	97.8

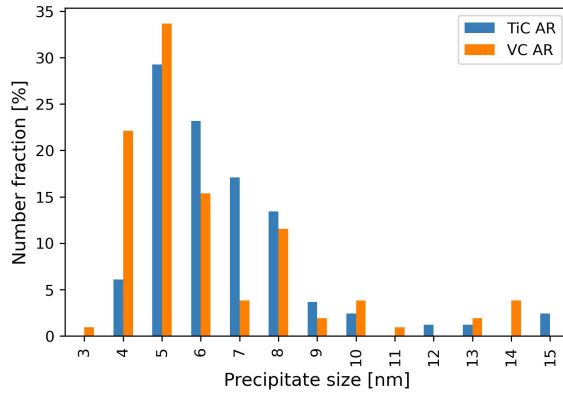


Figure 3.2.: Normalised TiC and VC precipitate size distributions in the AR alloys. Sizes are the average ($\sqrt{\text{length} * \text{width}}$) sizes of platelet shaped precipitates.

research. The main reason for these treatments was to grow the precipitates. Austenite start temperatures (A1) were determined as 729 °C for the TiC alloy and 696 °C for the VC alloy using the Thermo-Calc software package [127]. Ioannidou et al. studied the same VC composition, and find a similar A1 temperature as well as no austenite formation after holding at 650 °C [128]. Following their approach, and in order limit grain growth and possible precipitate dissolution, heat treatment temperatures were kept below the A1 temperatures and all heat treatments were performed at 700 °C for the TiC alloy and 650 °C for the VC alloy. To grow the precipitates to different sizes, heat treatment durations of both 2 h and 20 h were used. These times exclude a 5 °C/min heat up and a furnace limited cooling down (± 1 °C/min). The second reason for utilising heat treatments was to charge the precipitates with hydrogen, to which end both heat treatments were also performed in a pure hydrogen atmosphere. The short 2 h heat treatments were performed in H₂ gas for the full duration. The long 20 h treatments were performed in N₂ for 18 h, followed by H₂ for 2 hours. Only the last 2 hours and the cooling down were performed in hydrogen for these treatments to exclude any effect of the gas on precipitate growth during the first 18 h. Lastly, both heat treatment durations were also performed in pure N₂ as a reference. Table 3.3 gives a concise overview of the heat treatments and how they will be designated throughout this paper. Before heat treatment, the surface of each specimen was sanded up to P1000 grit to create a repeatable surface finish.

3.2.1. MICROSTRUCTURAL CHARACTERISATION

After heat treatment, some specimens were prepared for microstructural analysis. Samples were cut and polished up to a 1 µm diamond finish for hardness measurements and Scanning Electron Microscopy (SEM). Macro-hardness measurements were performed on an automatic Vickers hardness testing machine. The HV2 was recorded for all heat treatment conditions, where indents were at least 100µm in size diagonally to be spaced over multiple grains. Extra

Table 3.3.: An overview of the different heat treatments used in this study and their designation throughout this article. All heat treatments were performed at 700 °C for the TiC alloy and 650 °C for the VC alloy.

Heat Treatment	Designation
2 h in N ₂	SN (short nitrogen)
2 h in H ₂	SH (short hydrogen)
20 h in N ₂	LN (long nitrogen)
18 h in N ₂ + 2 h in H ₂	LNH (long nitrogen + hydrogen)

OPS 0.04 μm finishing was performed for Electron Backscattering Diffraction (EBSD) measurements. EBSD analysis was used to obtain an accurate grain size distribution, where only boundaries with an angle of more than 5 degrees were considered. Analysis was performed on a Thermo Fisher Scientific™ Helios™ G4 PFIB UXe SEM equipped with an EBSD sensor. In each case, mappings were made at an accelerating voltage of 20 kV, a current of 3.2 nA and a step size of 0.085 μm.

Furthermore, TEM analysis was used to characterise the precipitates in both microstructures. Specimens were manually polished to 30 μm thickness, followed by Ar⁺ ion milling to electron transparency. A Thermo Fisher Scientific™ Cs corrected cubed Titan™ was used, operating at 300 kV. For elemental analysis in STEM mode, the super-X detector in the ChemiSTEM™ configuration was employed, and TEM images were collected on a Ceta™ 16M camera.

Lastly, SIMS imaging was employed to observe hydrogen trapping in larger TiC and VC precipitates present in the LNH heat treatment conditions. For SIMS analysis, samples of 1 cm² cross-sectional area were embedded in conductive resin and polished up to an OPS 0.04 μm finish. SIMS analysis was carried out using high vacuum SCIOS-SIMS which is an instrument based on Thermo Fisher Scientific™ FIB-SEM platform with a magnetic sector mass spectrometer [32]. The mass spectrometer was developed in-house by Advanced Instrumentation for Nano Analytics (AINA) group of Luxembourg Institute of Science and Technology (LIST). The instrument uses ⁶⁹Ga⁺ primary ions and has a mass resolving power ($M/\Delta M$) of 400 [32]. It uses four channeltron detectors for mass filtered signal detection. In this work, the samples were biased to -500 V in negative mode to extract ¹H⁻ secondary ions and to +500 V in positive mode to extract ⁴⁸Ti⁺ and ⁵¹V⁺ secondary ions from the sample. The FIB was operated at an acceleration voltage of 30 kV and probe current of 50 pA. The background intensity in ¹H⁻ SIMS images is slightly high due to the high vacuum (not UHV) condition of the instrument which results in the presence of higher amounts of hydrogen in the residual gas inside the chamber (e.g., humidity) [33].

3.2.2. THERMAL DESORPTION SPECTROSCOPY

Thermal Desorption Spectroscopy (TDS) equipment was used to analyse the amount of absorbed hydrogen in the specimens. This was done on a Bruker G8 Galileo device equipped with an IR07 infrared furnace that allows for custom temperature ramping while continuously measuring the desorbed hydrogen flux using a thermal conductivity detector. TDS was performed on steel specimens of 2 x 20 x 110 mm in size, which were first sanded with P1200 sandpaper to remove any oxidation layer and create a reproducible surface finish for desorption. Each combination of steel type and heat treatment was measured at least 3 times with different heating rates, namely 1, 0.66 and 0.33 °C/s. All measurements were performed over a range of 40 °C to 900 °C.

Performing TDS measurements at different heating rates allows for fitting of peak temperatures according to the simplified Kissinger equation [129]:

$$\frac{d \ln(\phi / T_{max}^2)}{d(1/T_{max})} = -\frac{E_A}{R} \quad (3.1)$$

In this equation T_{max} is the peak temperature of a specific H desorption peak in K, ϕ is the heating rate in K/s, R is the universal gas constant $8.3415 \text{ J} \cdot \text{K}^{-1} \cdot \text{mol}^{-1}$ and E_A is the activation energy for hydrogen desorption of the specific hydrogen trap in kJ/mol. By fitting $\ln(\phi / T_{max}^2)$ to $(1/T_{max})$, E_A can be inferred from the slope.

3.2.3. MECHANICAL CHARACTERISATION

Five tensile specimens were prepared and subsequently subjected to each heat treatment condition for mechanical characterisation in a Slow Strain Rate Tensile (SSRT) test. Figure 3.3 displays the specimen geometry. The specimens were all machined perpendicular to the rolling direction of the steel sheets. Before each test, the specimen was sanded up to a P1200 grit finish to remove any oxide layer and realise a surface finish similar to that of the TDS specimens. The tests consist of a constant crosshead displacement of 4.5 mm/h until fracture, which corresponds to an original strain rate of $3 \cdot 10^{-5} \text{ s}^{-1}$ in the gauge section. This strain rate was chosen to allow for sufficient hydrogen diffusion throughout the specimen during the test according to ASTM G142 and G129 [110, 130]. The tests were performed on a Zwick Z100 universal tensile tester.

3.3. RESULTS & DISCUSSION

3.3.1. GRAIN SIZE EVOLUTION

Each sample condition was prepared for EBSD analysis of the grain structure in order to characterise the grain size evolution after all heat treatment conditions. Areas containing several hundreds of grains were measured. Representative images of the both steels after conditions SN and LN (designated VC_{SN} , VC_{LN} , TiC_{SN} and TiC_{LN} , respectively) are shown in Figure 3.4. Microstructures resulting from the short 2 h heat treatment conditions still show some degree of deformation of the lattice as a

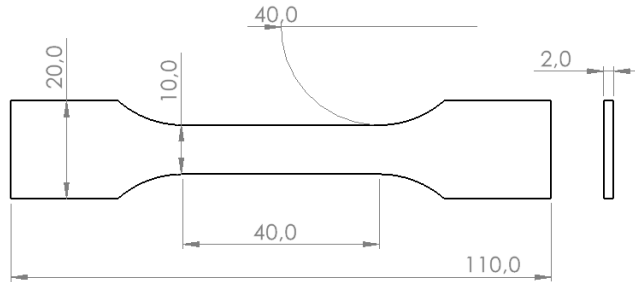


Figure 3.3.: Drawing of the tensile specimen geometry used for SSRT testing. Dimensions are in mm.

result of the hot rolling process. This is eliminated after the long heat treatment of 20 h. X-Ray Diffraction (XRD) measurements confirmed the microstructures after all heat treatment conditions to be fully ferritic. It was found that grain growth during the annealing cycles is limited, and the microstructures of both alloys after long heat treatments are not significantly different from those after short heat treatment as a result of grain boundary pinning by the nano-carbides. The grains are non equiaxed and widespread in areas ranging from $<1 \mu\text{m}^2$ to occasional grains with areas of $>100 \mu\text{m}^2$. Smallest, average and largest grain areas were obtained from the EBSD images and are listed in Table 3.4 as advised by ASTM E1181 for a random grain size distribution of large range [131]. A grain area of $0.1 \mu\text{m}^2$ was chosen as the cut-off point where individual grains can be accurately distinguished from noise with the chosen EBSD step size of 85 nm. Only little grain growth is observed in the TiC alloy even after the long 20 h heat treatments. Any reduction in strength as a result of the heat treatments can therefore be attributed to precipitate growth and the resultant over-aging of the microstructure. In contrast, the average grain size in the VC alloy roughly doubles after the 20 h compared to 2 h so an influence of grain growth on strength reduction is expected. Since it has been shown in the literature that high temperature hydrogen charging does not fill grain boundaries [22, 112, 117], an influence of varying grain sizes on HE is not expected.

3.3.2. PRECIPITATE GROWTH

After TEM analysis of all heat treatment conditions, the acquired images were scanned for precipitates. The average size ($\sqrt{\text{length} * \text{width}}$) of all visible precipitates was manually measured from these images, of which the smallest, average and largest ones have been listed in Table 3.4. The full distributions are displayed in Figure 3.5a for condition SH, and in Figure 3.5b for LNH. Distributions in conditions SN were confirmed to be identical to that in SH for both alloys, as well as condition LN to that for LNH. It becomes apparent from Figure 3.5a that the TiC precipitates adhere to an approximate normal distribution around an average of 10 nm. The VC precipitates, on the other hand, seem to be somewhat smaller in size. The largest

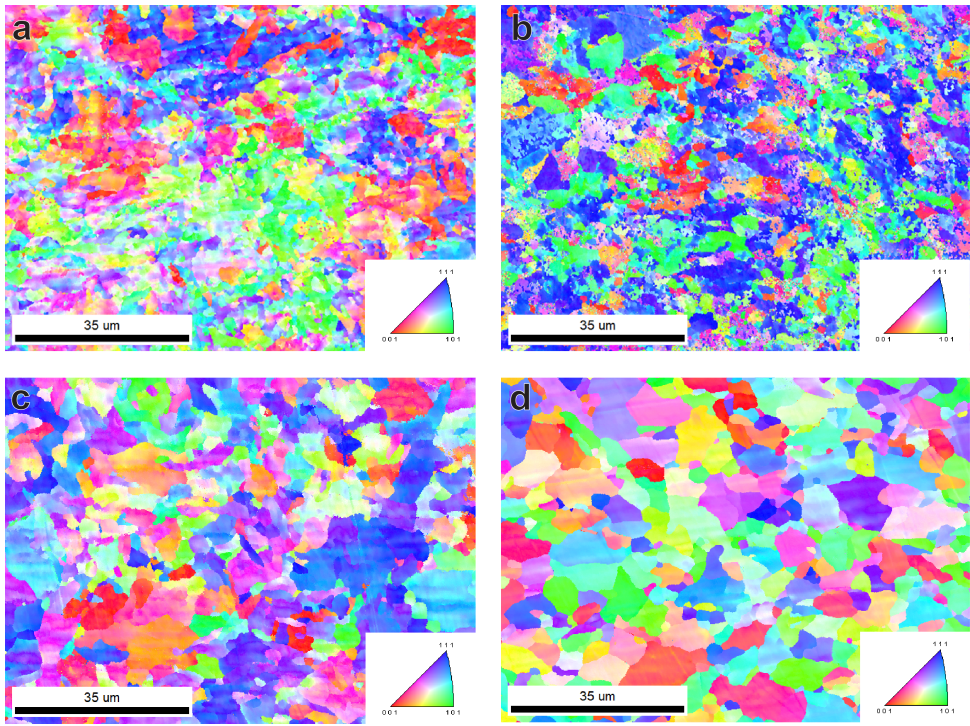


Figure 3.4.: Inverse Pole Figures of the a) TiC_{SN} , b) TiC_{LN} , c) VC_{SN} and d) VC_{LN} conditions, obtained using the OIM AnalysisTM software.

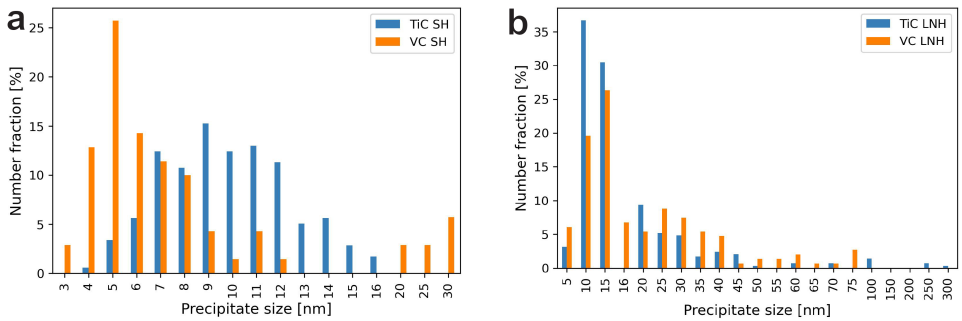


Figure 3.5.: Normalised precipitate size distributions for both alloys in conditions a) SH and b) LNH.

fraction of them lies around an average of 5 nm, with some occurrences between 20 and 30 nm in size. Both precipitate types thus show some growth after a short heat treatment of 2 hours when compared to the AR state, although the titanium carbides show more coarsening after this short duration. The distributions differ after the long

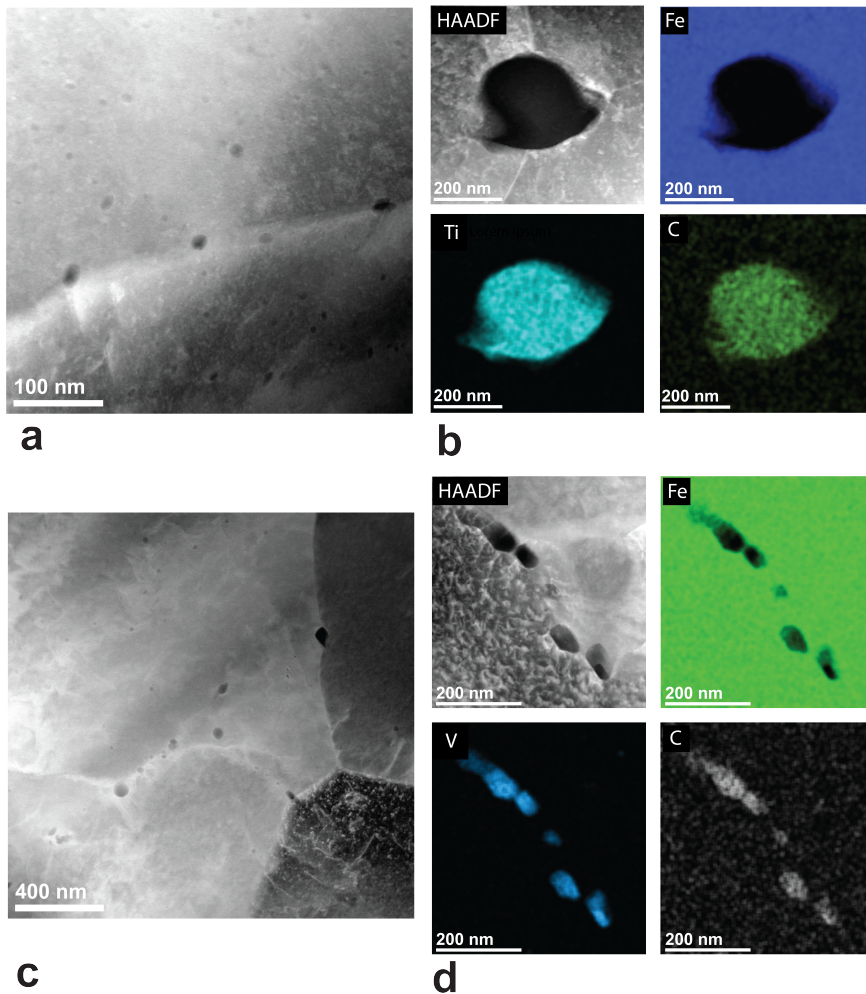


Figure 3.6.: High Angle Annular Dark-Field (HAADF) and Energy Dispersive X-Ray (EDX) images of a) 5 - 30 nm and b) 350 nm TiC precipitates, and c) 10 - 90 nm and d) a group of 50 - 90 nm VC precipitates found in the specimens TiC_{LNH} and VC_{LNH} , respectively.

20 h treatment, for which figure 3.6 illustrates some precipitate occurrences. The TiC distribution still shows a large fraction of carbides around a size of 10 - 15 nm, although some larger precipitates now start to arise that grow to 20 nm or more. The VC distribution shows a larger fraction of precipitates in the 20 - 30 nm size than the TiC, and almost all those smaller than 10 nm have disappeared. Figure 3.5b also shows incidental occurrence of precipitates larger than 100 nm in size for the TiC alloy. In fact, these precipitates were observed for both the VC and TiC alloys in all heat

Table 3.4.: An overview table with microstructural details for all heat treatment conditions. Grain areas were obtained from EBSD results, precipitate sizes were characterised using TEM.

	HT	Hardness HV2	Grain area [μm^2]			Precipitate size [nm]		
			Low	Average	High	Low	Average	High
TiC	AR	267 ± 1.9	-	-	-	2.9	5.7	60
	SN	272 ± 3.1	0.1	3.8	160	2.8	8.6	290
	SH	270 ± 2.7	0.1	2.5	159	3.2	6.5	140
	LN	238 ± 1.6	0.1	5.0	192	5.7	30.3	235
	LNH	223 ± 0.4	0.1	4.0	189	3.6	21.7	223
VC	AR	261 ± 2.4	-	-	-	2.6	6.1	150
	SN	241 ± 1.2	0.1	12.5	223	3.8	9.9	522
	SH	246 ± 1.0	0.1	10.8	243	3.6	7.9	470
	LN	230 ± 0.7	0.1	24.9	231	2.5	17.6	349
	LNH	222 ± 1.2	0.1	23.3	299	3.5	17.4	294

treatment conditions, as well as in the AR state. TEM analysis often overlooks them since their spacing is large compared to the analysed area, but through SEM and SIMS observations it was shown that they exist in all conditions and do not grow in size considerably even after the long heat treatments. The amount of large incoherent precipitates in the TiC alloy was higher than that in the VC alloy. The average TiC precipitate size in Table 3.4 is therefore skewed to a larger average size than the VC precipitates, even though Figure 3.5b shows the TiC_{LNH} precipitates to be smaller than the VC_{LNH} . Lastly, it was observed that carbides in the VC alloy preferentially grow on grain boundaries. This can be seen in Figure 3.6.

Wei et al. state that the critical size for TiC precipitates with the Baker-Nutting orientation to be coherent is 4.2 nm across the broad surface [117]. Therefore only the fraction of carbides that was measured to be smaller than 5 nm could be coherent across the interface. Table 3.4 shows that precipitates smaller than this size were observed in the AR as well as the SN and SH heat treatments. However, this is only a small fraction of all precipitates as can be observed from Figures 3.2 and 3.5a. Therefore, most of the precipitates will instead be semi-coherent with the steel matrix. After the 20 h heat treatments, the small TiC precipitates are considered to be exclusively semi-coherent, while the medium and larger sized ones are incoherent with the matrix. VC precipitates have a lattice constant that is closer to that of the steel lattice, so the critical size for coherency is slightly larger. Takahashi et al. observe small platelike VC precipitates with a thickness of 2-5 nm and a length of approximately 20 nm to be mostly coherent with the matrix, except for misfit dislocation around the curved sides [26]. This is larger than the sizes found for the 2 h heat treatments in this research, so the small VC precipitates can be considered coherent with the matrix at this size. After the 20 h heat treatment, Figure 3.6c shows

medium sized vanadium carbides to be more globular in shape. This is an indication that the surface is no longer coherent with the matrix and will instead have become semi-coherent or fully incoherent, though it becomes clear from Figure 3.5b that some smaller precipitates still remain coherent. It is known that incoherent vanadium carbide precipitates do not usually have a 1:1 stoichiometry but rather exist as V_4C_3 or V_6C_5 structures with a high carbon vacancy content [121, 122]. A varying V-C ratio was also found in elemental analysis during STEM measurements, which confirms large amounts of carbon vacancies in incoherent VC precipitates. The TiC precipitates also showed the presence of carbon-vacancies, but only at precipitate sizes of >100 nm. Figures S1, S2 and S3 show examples of EDX maps and line scans to illustrate the V:C and Ti:C ratios in selected precipitates.

3.3.3. EFFECT ON HYDROGEN ABSORPTION

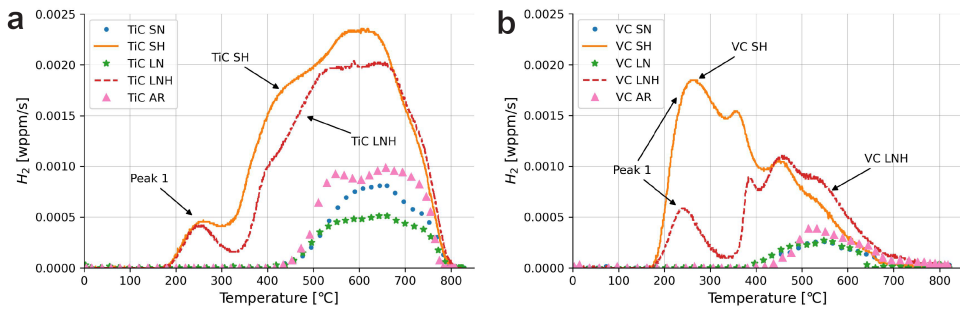


Figure 3.7.: TDS spectra obtained at a heating rate of 1 °C/s for all conditions in a) the TiC alloy and b) the VC alloy.

Table 3.5.: Overview of hydrogen contents in weight part per million (wppm) for all heat treatment conditions.

Heat Treatment	TiC H ₂ [wppm]	VC H ₂ [wppm]
As-received	0.30 ± 0.03	0.09 ± 0.03
SN	0.22 ± 0.02	0.06 ± < 0.01
SH	0.91 ± 0.03	0.44 ± 0.07
LN	0.17 ± 0.02	0.06 ± < 0.01
LNH	0.70 ± 0.04	0.28 ± 0.03

TDS was used to analyse the hydrogen absorption in all conditions. Table 3.5 lists the total amount of hydrogen trapped in each set of heat treatments. A first observation to be made is that the AR materials already contain a small amount of hydrogen, which is most likely a consequence of hydrogen absorption from water-vapor during hot rolling, which has been shown to charge TiC precipitates by Wei et al. [117]. The TiC alloy contains the most hydrogen, with 0.30 wppm

on average, compared to 0.09 wppm in the AR VC steel. It can also be observed that the heat treatments in a pure N₂ environment decrease the total hydrogen content relative to that in the AR state. This is to be expected since if there is no additional hydrogen present to charge the samples during the heat treatment, hydrogen will be desorbed instead. The VC alloy contains less hydrogen overall than the TiC alloy, although the trends are similar. The hydrogen content in the TiC steel is reduced to 0.22 and 0.17 wppm in the SN and LN heat treatments, respectively. The hydrogen content in the VC steel is slightly reduced to 0.06 wppm after the SN heat treatment, which does not decrease further after the LN heat treatment.

The TiC_{SH} condition contains a hydrogen content of 0.91 wppm, compared to 0.70 in condition TiC_{LNH}. This difference can most likely be attributed to a difference in precipitate size distribution. A similar effect can be observed in the VC alloy, which contains 0.44 wppm in condition VC_{SH} and 0.28 in condition VC_{LNH}. The desorption spectra in Figure 3.7 show that although the hydrogen trap distribution is very similar between the two heat treatment conditions in the TiC alloy, it differs significantly in the VC alloy. The lowest temperature peak (Peak 1 in Figure 3.7a) decreases in size significantly after a long heat treatment duration, whereas the other peaks stay relatively similar in size. Moreover, the high temperature peaks above 400 °C contain much less hydrogen than their counterparts in the TiC alloy. This suggests less overall H trapping in the incoherent VC precipitates, but the smaller amount of incoherent VC compared to TiC precipitates also plays a role. The fact that the hydrogen desorption spectra level off around 700 °C in the VC alloy compared to 800 °C in the TiC alloy suggests lower energy trapping for the incoherent VC precipitates.

HYDROGEN TRAPPING STRENGTH

Other than the desorption spectra shown in Figure 3.7 measured at 1 °C/s, all conditions were also tested at heating rates of 0.66 and 0.33 °C/s. This was done to allow fitting of peak temperatures according to the simplified Kissinger's equation (Equation 3.1). To obtain the peak temperatures, the desorption spectra of each heating rate were fit to 4 skewed Gaussian peaks using the Python LMFfit package. The deconvoluted curves for Peak 1 in all VC_{SH} heating rates and the resulting plot to calculate E_A are displayed in Figure S4 for illustration. Unfortunately, significant peak overlap above 300 °C made any realistic interpretation of trapping energies impossible. This is an issue also encountered by Vandewalle et al. [112] and Drexler et al. [40], who review the Kissinger theory and its applicability to overlapping peaks. They find that accurate validation of trapping energies for overlapping peaks can only be obtained if extra boundary conditions based on relative hydrogen trap occupancy are applied to the fitting method. Such knowledge was not obtained in this work. Therefore, further discussion and relation to trapping energies will be restricted to those obtained for the lowest temperature peaks, or Peak 1 as shown in Figure 3.7 and listed in Table 3.6, since these peaks show sufficient separation from the rest of the spectrum for sound interpretation. None of these first peaks can be classified as a fully reversible trap, which is most commonly associated with trapping energies of <30 kJ/mol [40, 132]. Instead, trapping energies range from strong to fully irreversible

with trapping energies ranging between 43 and 96 kJ/mol.

Table 3.6.: Overview of the trapping energies obtained for Peak 1 in all hydrogen charged conditions.

HT Condition	E_A [kJ/mol]
TiC _{SH}	96 ± 2
TiC _{LNH}	43 ± 3
VC _{SH}	54 ± 1
VC _{LNH}	72 ± 10

3.3.4. ORIGINS OF HYDROGEN TRAPPING IN TiC

ORIGIN OF THE FIRST PEAK

Figure 3.7a shows that the desorption spectra for TiC after the short and long heat treatment durations look mostly similar. This suggests that the same traps are occupied inside the steel, but their relative occupancy differs. Firstly, it seems that the low temperature peak remains almost identical in both conditions. In the literature, low temperature trapping is frequently associated with coherent or semi-coherent precipitates. Direct observation of deuterium at TiC interfaces has been made by Takahashi et al. in atom probe studies, on precipitates that are similar in morphology to those observed in conditions TiC_{SN} and TiC_{SH} [119]. Deuterium was observed around the precipitate interface of the plate-like carbides, but not in the bulk, which suggests either interface misfit dislocations or interface C-vacancies as a possible trapping site. Wei et al. measure coherent TiC precipitates to have an overall activation energy of between 46 and 59 kJ/mol [100], but state in a different paper that the misfit dislocation on the semi-coherent interface of TiC has an activation energy of 56 kJ/mol [27]. A different study attributes an energy of 42 kJ/mol to the interface of incoherent precipitates [24], which is close to a value calculated in a separate atomistic study, that finds a maximum of 48 kJ/mol for a misfit dislocation [118]. Since a value of 43 kJ/mol was measured for the TiC_{LNH} condition in this research, it is reasonable to assume that the misfit dislocation is the origin of this trapping peak. However, this is in contrast to the value for Peak 1 in the TiC_{SH} condition, which was measured as 96 kJ/mol. This value is closer to values of 111 kJ/mol obtained by Zhang et al. [104] and 99 kJ/mol obtained from our previous research [96], where activation energies were calculated for a C-vacancy on a coherent TiC surface in BCC iron. An explanation why two different values could be measured is that there is a small fraction of precipitates after the 2 h heat treatment condition that is fully coherent with the matrix. These are most likely the precipitates in Figure 3.5a with a size smaller than 5 nm. After a short heat treatment, hydrogen could be trapped here in C-vacancies on the coherent interface. These precipitates grow to a semi-coherent size after heat treatment conditions TiC_{LN} and TiC_{LNH} in which case the hydrogen is trapped in misfit dislocations instead of C-vacancies.

ORIGIN OF THE HIGH TEMPERATURE PEAKS

The high temperature peaks in the TiC desorption spectra can be attributed to hydrogen trapping by incoherent precipitates, like the studies by Vandewalle et al. and Pérez-Escobar et al. [22, 112]. A comparable study, which has similar TiC size distributions to those observed in this research, finds a reduced H absorption through electrochemical charging with increasing annealing time and consequently precipitate size [24]. They attribute this to trapping on the precipitate interface, which has a high activation energy and diffusion barrier, and decreases with increasing precipitate size. This could explain that the spectrum for TiC_{LNH} shows less trapped hydrogen at peaks between 350 and 700 °C than that for TiC_{SH} . The same conclusion is also reached by other authors [22, 27, 117], although direct observations were not made. The highest temperature peaks at roughly 450 °C and above are expected to belong to traps inside the largest precipitates of size >100 nm. In this study, these were seen to already be present in the AR material, and remain relatively unchanged after heat treatment. Vandewalle et al. attribute an increased concentration of incoherent TiC precipitates to an increased hydrogen uptake in the peaks between 500 and 900 °C [112]. Since precipitates of this size are not changed significantly in this research, the hydrogen uptake in these peaks stays relatively similar.

OBSERVATION OF TRAPPING IN INCOHERENT TiC

Vandewalle et al. assume trapping in bulk C-vacancies only [112], based on theoretical work by Di Stefano et al. who discuss hydrogen diffusion into the TiC bulk through continuous C-vacancy networks [118]. Incoherent TiC precipitates that have a continuous C-vacancy network throughout the bulk require a lower diffusion energy for hydrogen to migrate into the precipitate bulk than precipitates where C-vacancies are not connected but instead separated by interstitial sites. This creates a different hydrogen absorption behaviour per precipitate, even though the activation energy of the trap stays the same. Hydrogen trapping in incoherent TiC was directly observed in this study through SIMS imaging. Figures 3.8a and 3.8b show hydrogen and titanium secondary ion maps, respectively, of the same area on the surface of a TiC_{LNH} sample. It can be observed from these images that not all of the titanium rich precipitates in Figure 3.8b trap hydrogen identically. One precipitate appears to store hydrogen more in the bulk, whereas the others store more around the interface. This is highlighted especially in Figure 3.9a, which shows a SIMS hydrogen map from a different area. The image shows that the hydrogen is localised around the circumference of these precipitates rather than over the entire bulk. Figure 3.8d shows a line profile along the white arrow in Figure 3.8c. It is easy to see that, on one hand, a significant amount of hydrogen is trapped in the precipitate, while on the other hand the hydrogen concentration inside the bulk is much lower than towards the interface. In fact it is similar to the level in the matrix. Hydrogen absorption in TiC precipitates scaling with surface area is refuted by the work of Pérez-Escobar et al. [22] and Wei et al. [133], who state that hydrogen absorption is proportional neither to precipitate surface area nor volume since they do not see a clear relation between increasing precipitate size and reducing hydrogen absorption. While no direct link to decreasing surface area

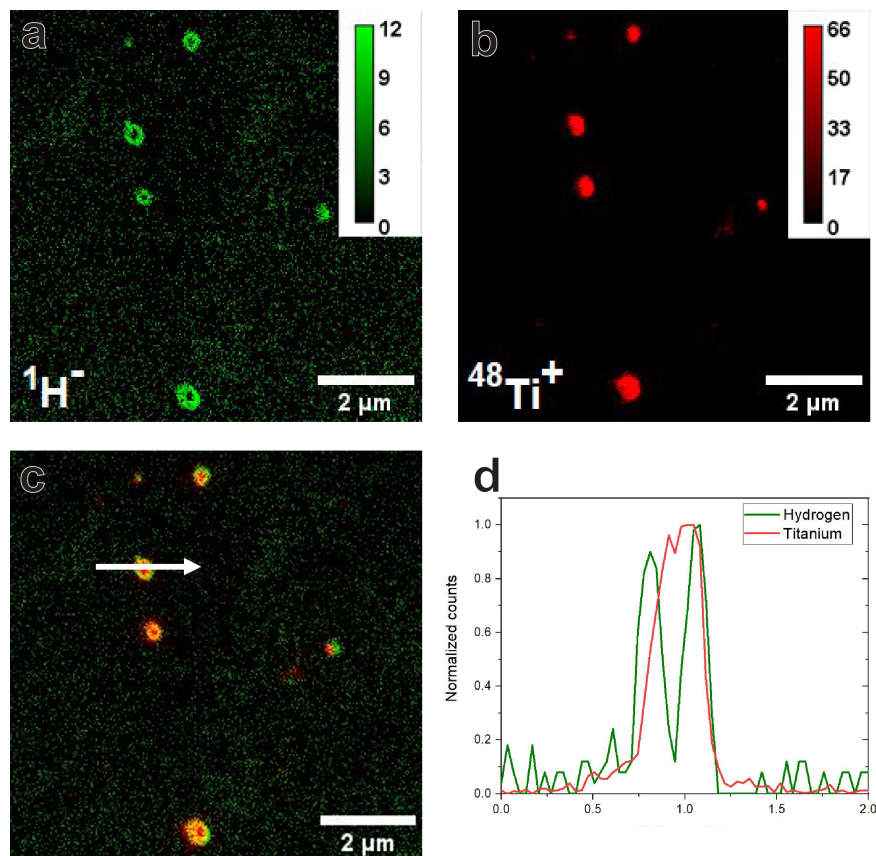


Figure 3.8.: SIMS images of a) $^1\text{H}^-$ map and b) $^{48}\text{Ti}^+$ map over the same area of acquisition in the TiC containing steel. Both the images were acquired using a beam current of 50 pA and a dwell time of 2.5 ms per pixel. The image resolution is 256 x 256 for a field of view $9\ \mu\text{m} \times 9\ \mu\text{m}$. c) shows merged elemental maps of $^1\text{H}^-$ (green) and $^{48}\text{Ti}^+$ (red) and d) shows a line profile of the region indicated by white arrow in c). The counts of the line profile diagram have been normalised for a qualitative comparison.

can be made from this work, the TDS spectra show that the TiC alloy absorbs less hydrogen in the incoherent precipitates with increasing annealing time, while SIMS images show a higher concentration near the interface. This indicates that incoherent TiC preferentially traps hydrogen near the interface, although SIMS is not a suitable technique to definitely prove trapping at the interface.

It should be noted that the time between hydrogen charging and analysis was significant for these images, with hydrogen charging happening some months before analysis. On one hand this shows that indeed these precipitates form very strong

hydrogen traps. On the other hand it does not clarify whether this distribution of hydrogen around the precipitate circumference is a result of hydrogen absorption during charging or desorption during storage. If fast diffusion through C-vacancy networks into TiC is assumed, off-stoichiometric precipitates with a high vacancy concentration would absorb more hydrogen over their entire bulk during the charging cycle, whereas precipitates with a lower vacancy concentration would trap most hydrogen near the interface. However, precipitates with a vacancy network allowing for fast diffusion would also release hydrogen more quickly during storage. Hydrogen release during storage is observed to be minimal, so the observation of hydrogen around the precipitate circumference is attributed to preferential trapping around the incoherent TiC/matrix interface. However, more analysis is required to fully validate this, including observations at different times after charging.

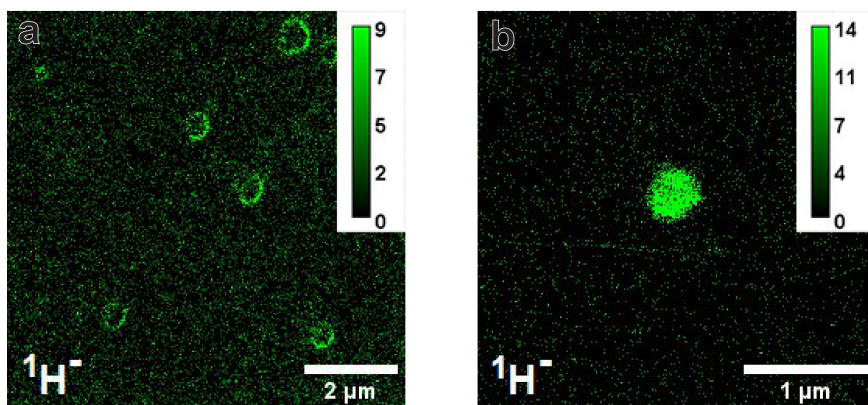


Figure 3.9.: Hydrogen maps obtained by SIMS analysis, showing a) localisation around TiC precipitates and b) trapping in a VC precipitate. Both the images were acquired using a beam current of 50 pA and dwell time 1 ms per pixel. a) has a resolution of 256 x 256 over a field of view 9 μm x 9 μm and b) has a resolution of 256 x 256 over a field of view 3 μm x 3 μm

3.3.5. ORIGINS OF HYDROGEN TRAPPING IN VC

ORIGIN OF THE FIRST PEAK

The TDS spectra for VC_{SH} and VC_{LNH} show a stark difference in the amount of hydrogen trapped in the lowest temperature peak. Like the TiC alloy, this peak can most likely be attributed to the trapping in smaller VC carbides. As discussed previously, the VC precipitates are still largely in the coherent domain after a 2 h heat treatment. Since no misfit dislocations are present in this case, the likely hydrogen trap is the C-vacancy on the coherent interface. The activation energy for C-vacancies measured by Takahashi et al. is approximately 60 kJ/mol [26], which matches reasonably well with the trapping energies of 53 and 72 kJ/mol measured in this research for the conditions VC_{SH} and VC_{LNH} , respectively. Experimentally,

Depover and Verbeken found an activation energy of 52 to 60 kJ/mol for V_4C_3 carbides, but only up to a size of 20 nm after electrochemical hydrogen charging [105]. Numerical studies have found activation energies for the trap at a coherent interface C-vacancy of 36.7 [103], 55.9 [104] and 51 kJ/mol [96]. Since all of the values are similar to what was measured in this work, the low temperature peak is attributed to the carbon vacancy on the coherent VC interface.

ORIGIN OF THE HIGH TEMPERATURE PEAKS

After having grown during the long heat treatments, as shown in Figure 3.6, most VC precipitates outgrow the coherent domain and become incoherent. The low temperature peak therefore largely disappears in the VC_{LNH} condition, as it did in the work by Depover and Verbeken [105]. At higher temperatures, however, the hydrogen uptake is slightly larger in the VC_{LNH} condition than in the VC_{SH} condition, which could be an effect of an increased amount of hydrogen trapped in the bulk of larger precipitates which increase in number with a longer heat treatment duration. To the authors' knowledge, no previous research has attempted high temperature charging of VC precipitates, and as such no trapping energies have been found for them in the literature. Unfortunately, due to strong peak overlap, no reliable trapping energies for these traps could be found in this research. Nonetheless, the high temperature peaks are attributed to trapping in carbon vacancies in the bulk of incoherent VC precipitates.

OBSERVATION OF TRAPPING IN INCOHERENT VC

Figure 3.9b shows a SIMS hydrogen map of the VC_{LNH} condition. The carbide can be seen to store hydrogen all throughout the bulk, contrary to the TiC carbides in Figure 3.9a which predominantly stores hydrogen near the interface. A comparison of the hydrogen trapping locations in the SIMS images suggests that H trapping in VC precipitates should scale with volume. This is supported by the TDS curve from Figure 3.7b, where the VC alloy stores more hydrogen at high temperatures after the longer treatment. Incoherent VC precipitates are therefore expected to be able to store more hydrogen overall than their TiC counterparts. However, since the total amount of incoherent vanadium carbides was much lower than that of the titanium carbides this was not observed in this study.

3.3.6. EFFECT ON MECHANICAL BEHAVIOUR

SSRT tests were used to characterise the extent of HE for each alloy and heat treatment condition, of which the results are summarised in Table 3.7. Representative tensile curves for each of the heat treatment conditions are shown in Figure 3.10. A first observation to note is that even the short heat treatments in the TiC alloy decrease its strength compared to the AR condition while ϵ_f is increased from 10.6 to 15.2 %. The long heat treatment in the TiC alloy further decreased both yield strength and UTS by approximately 10%. ϵ_f is only increased slightly in these conditions, but because of a larger scatter in values it is not a conclusive

Table 3.7.: Overview of the 0.2% proof yield strength $\sigma_{y, 0.2\%}$, UTS and strain at break ϵ_f for all heat treatment conditions. Errors are standard deviations.

Alloy	Heat Treatment	$\sigma_{y, 0.2\%}$ [MPa]	UTS [MPa]	ϵ_f [%]
TiC	AR	698 ± 2	804 ± 2	10.6 ± 0.39
	SN	638 ± 22	740 ± 18	15.2 ± 0.35
	SH	624 ± 10	727 ± 2	16.1 ± 0.53
	LN	533 ± 60	650 ± 39	17.6 ± 0.50
	LNH	579 ± 57	652 ± 27	18.5 ± 0.94
VC	AR	656 ± 7	736 ± 2	10.0 ± 0.13
	SN	656 ± 7	743 ± 7	16.5 ± 1.08
	SH	658 ± 10	758 ± 4	17.1 ± 0.88
	LN	583 ± 6	674 ± 12	18.4 ± 0.53
	LNH	567 ± 11	658 ± 6	16.6 ± 1.24

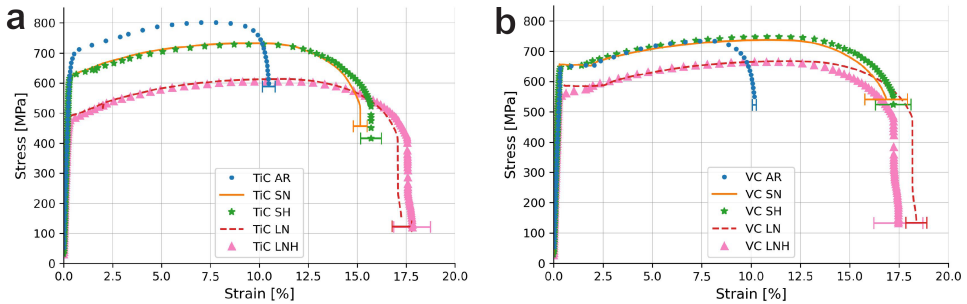


Figure 3.10.: Representative Slow Strain Rate Tensile (SSRT) curves for all conditions in a) the TiC alloy and b) the VC alloy. Error bars show standard deviations in the fracture strain [%].

increase. In the VC, the two hours heat treated samples do not show a reduction in strength compared to the AR condition, which is a result of limited precipitate growth after 2 h. It is only seen after the long heat treatments, where it drops by approximately 10 - 15 %. An increase in ϵ_f from 10 to 16.5 % is observed in the short heat treatments compared to the as received condition, but once again the scatter increases after long heat treatments. Therefore, no conclusive statements about an increase or decrease can be given. In the TiC alloy, the change in mechanical behaviour between the 2 h and 20 h heat treatments can be explained by precipitate over-aging [64], since Table 3.4 shows that the grain size did not significantly increase even after the long heat treatment, while the precipitates were found to increase in size. In the VC alloy, the grain size did show an increase, which mean the reduction in strength is likely a combination of grain growth and precipitate over-aging.

Hydrogen Embrittlement, which would become apparent as a reduction in ϵ_f in

the condition SH compared to SN, or LNH compared to LN, is not observed in any case for either alloy. It is known that different hydrogen concentration profiles are created depending on the charging method [22, 54]. Electrochemical charging creates a large concentration of diffusible hydrogen in sites like grain boundaries and interstitials, while high temperature gaseous charging also fills up traps with a high trap energy while providing the hydrogen with enough energy to overcome shallow traps [26, 112]. The lowest activation energy measured in this research was 43 kJ/mol for misfit dislocations around small TiC precipitates, which is not considered diffusible hydrogen, nor irreversibly trapped hydrogen [40, 132]. Similarly, C-vacancies on the coherent VC interface fall in this category with an activation energy of around 60 kJ/mol. Since these activation energies do not fall into the reversible category (<30 kJ/mol [56]), they are not expected to contribute to HE, which was also found in this study. Several specimens were subjected to a post-mortem TDS cycle after tensile testing to exclude the possibility that hydrogen effusion from the specimens during the test was the reason HE was not observed. These measurements showed no decrease of hydrogen content over the duration of the tensile test. These traps therefore contribute to preventing HE in the alloys even though they are not completely irreversible. Moreover, Depover et al. showed that these traps can be filled through electrochemical charging at room temperature [105], while they were also charged through high temperature gaseous charging in this study. This means that they can act as hydrogen sinks in different service conditions. Optimisation of these types of hydrogen traps could lead to creating more hydrogen resistant steels.

This work is unique compared to similar works [22, 112] in the fact that high temperature as well as low temperature peaks were observed after high temperature gaseous charging. This is most likely a result of performing both the heat treatment and the cooling down in hydrogen gas. During the cooling down, the available energy for hydrogen to overcome shallower traps gradually decreases, and hydrogen is expected to occupy these sites eventually. Depover et al. [105] showed that hydrogen traps belonging to misfit dislocations, the lowest energy traps found in this work, can also be charged through electrochemical methods. An effect of these traps on HE was observed in their study, whereas the material was not embrittled in this research. This suggests a more favourable hydrogen trap occupation after gaseous charging when compared to electrochemical charging, that does not result in any HE.

3.4. CONCLUSIONS

In this work, TiC and VC precipitate growth and hydrogen absorption as a result of high temperature gaseous hydrogen charging was successfully characterised using TEM, EBSD and TDS. Moreover, direct observation of hydrogen trapping in incoherent precipitates was made using SIMS. By combining these techniques, the following conclusions could be drawn on the hydrogen trapping and embrittlement behaviour of titanium and vanadium carbide containing steels:

- High temperature gaseous charging is shown to be a suitable way to charge steel containing deep hydrogen traps. The TiC and VC containing alloys were

charged with hydrogen up to 0.91 and 0.44 wppm, respectively.

- Little effect of TiC precipitate size on hydrogen trapping was found. All precipitates were either semi-coherent or incoherent even after a 2 h heat treatment duration. Coherent TiC precipitates trap hydrogen in misfit dislocations around the semi-coherent interface with an activation energy of 43 kJ/mol. Most hydrogen was trapped in carbon vacancies near the interface of larger incoherent particles, for which an activation energy was not obtained.
- An effect of VC precipitate size was observed in the form of a reduction in low temperature hydrogen trapping after 20 h of heat treatment. The hydrogen traps after the 2 h heat treatment were characterised as mainly carbon vacancies on the coherent VC interface with an energy of between 53 and 72 kJ/mol. After the 20 h treatment, most hydrogen is stored in the bulk of large incoherent vanadium carbides with a large amount of carbon vacancies, for which no activation energy was found in this work.
- Direct observation of hydrogen trapping in incoherent TiC and VC carbides was made using SIMS. Large TiC precipitates were shown to vary in the degree of hydrogen absorption and to preferentially trap hydrogen near the precipitate interface. VC precipitates were shown to trap hydrogen throughout the bulk, but were present in smaller quantities, leading to an overall lower absorbed hydrogen content. More SIMS analysis is required to further elaborate on the trapping characteristics of incoherent precipitates.
- Neither of the heat treatment conditions resulted in any observable HE after mechanical characterisation. This proves that nano-carbides can successfully be used as a hydrogen sink as well as a strengthening mechanism in steels after high temperature gaseous hydrogen charging. However, further study using electrochemical charging is recommended to compare the effects of different charging conditions on HE.

4

EFFECT OF TITANIUM AND VANADIUM NANO-CARBIDE SIZE ON HYDROGEN EMBRITTLEMENT OF FERRITIC STEELS

Tim BOOT, Pascal KÖMMELT, Hans (J.C.) BROUWER, Amarante BÖTTGER, Vera POPOVICH

The effect of TiC and VC nano-precipitate size on the hydrogen embrittlement of ferritic steels was studied in this work. Steels containing two size distributions (10 nm or less and 10 - 100 nm) of TiC and VC carbides are subjected to tensile tests in-situ in an electrochemical hydrogen charging environment. Hydrogen is found to be trapped in interstitial matrix sites on the precipitate/matrix interface with activation energies of 14 - 20 kJ/mol and inside misfit dislocation cores with energies of 27 - 37 kJ/mol. All steels are embrittled by 15 to 20 %, except the TiC steel with semi-coherent carbides up to 100 nm, which is embrittled by 37 %. This is caused by accelerated intergranular fracture as a result of hydrogen trapped in dislocation pile-ups around grain boundary precipitates. The steel with coherent VC nano-carbides retained the highest strength and ductility during in-situ testing. This is therefore the optimal carbide configuration for use in hydrogen environments.

This chapter has been published in NPJ Materials Degradation **9**, 1 (2025) [134].

4.1. INTRODUCTION

In the search for safer and more lightweight vehicles, the automotive industry has been engaged in development of Advanced High Strength Steels (AHSS) [3, 4, 135]. The goal for these steels is to obtain both high strength and high ductility to provide good formability and toughness. Many strengthening mechanisms in steels can, however, also cause Hydrogen Embrittlement (HE). Microstructural features like hard phases, retained austenite and refined grains attract hydrogen that can cause fracture [12–17]. HE shows as a reduction in ductility or strength in steels which leads to premature failure of components. A frequently researched mitigation method for HE is to trap hydrogen in the microstructure where it cannot lead to fracture [21–24]. Crucial in this method is to decrease the amount of diffusible hydrogen in the microstructure, which can diffuse towards critical areas and as such is considered the main cause of HE [24, 34, 105, 111, 114, 115, 136]. Carbide precipitates are one solution that is looked into in this regard, since they are expressly useful for precipitation strengthening of steel, while at the same time providing a wide range of hydrogen trapping capabilities [22, 27, 34, 67, 100, 105, 111–113].

The specific trapping strength of precipitates depends on where the hydrogen is trapped, which can be either in the elastic strain field around the precipitate, on the precipitate/matrix interface or in the precipitate bulk [137]. The strength with which hydrogen is trapped is determined by the activation energy E_A that is required for hydrogen to desorb from the trap. Experimental as well as numerical studies have attempted to identify these energies. The strain field around precipitates is generally considered the weakest trap with values ranging between 2 to roughly 30 kJ/mol [27, 95, 96]. The precipitate/matrix interface can host a number of trapping sites, including interstitial locations, vacancies and misfit dislocations. The activation energies for these types of traps have been found to range from approximately 20 to 30 kJ/mol for interstitial sites [24, 99, 100], to 60 up to 90 kJ/mol for carbon vacancies on the interface [21, 26, 96, 104, 118]. Misfit dislocations fall in a large range in between the two [27, 118, 138]. Lastly, carbon vacancies in precipitate bulk are found to be the strongest traps with energies of around 100 to as much as 145 kJ/mol [21, 27, 95, 96, 105, 112, 120, 123, 125]. Which types of traps are present depends on the type of precipitate as well as their size and morphology. Small coherent precipitates have a large elastic strain field but lack misfit dislocations. Upon precipitate growth, the misfit with the steel lattice becomes too large and misfit dislocations start forming. This happens around a size of 4.2 nm for TiC precipitates, but only around 20 nm for VC precipitates [26, 117]. Even larger precipitates become fully incoherent with the matrix, at which point there is a large concentration of carbon vacancies, but the interface starts forming a diffusion barrier for hydrogen diffusion into precipitate bulk [22, 27, 117].

The synergistic effect of precipitate size on strength of a steel as well as hydrogen trapping behaviour thus becomes an important field of study. Chapter 3 focused on comparing two types of precipitates, namely TiC and VC, of two different size distributions after hydrogen charging in a gaseous atmosphere [21]. Here, as well as in other studies, it was found that large incoherent precipitates store a significant amount of hydrogen at a high activation energy in bulk C-vacancies, that do not cause

any HE [21, 22, 112]. However, since small nano-sized carbides were not affected during gaseous charging, weaker reversible traps could not be studied. A different charging environment is therefore required to study the effect of nano-sized carbides, which are more beneficial for precipitate strengthening and hydrogen storage on interface traps [24, 26, 126]. The hydrogen trapping characteristics of TiC and VC precipitates has been studied in detail experimentally by for example Wei and Tsuzaki [27, 133], Depover and Verbeken [24, 34, 105] and numerically by Di Stefano [118] and Sagar [96]. It remains important, however, to consider the implications of precipitate size on the mechanical properties of steels and couple their hydrogen trapping capabilities to fracture mechanisms. This work characterises the effects of VC and TiC nano-precipitates of different sizes after in-situ tensile testing in an electrochemical hydrogen charging environment, and relates the trapping of hydrogen around nano-carbides to the mechanical behaviour and fracture mechanisms. A fracture micro-mechanism is presented that explains the detrimental effect of intergranular nano-carbides compared to those present in the grain interior. This information is integrated in order to find a preferred precipitate type and size distribution for design of steels for use in a hydrogen environment.

Table 4.1.: Summarised alloy contents of the TiC and VC alloys in weight %, determined using X-Ray Fluorescence (XRF).

Alloy type	C	Mn	Al	Si	Ti	V	Trace elements	Balance Fe
TiC	0.07	1.7	0.01	0.01	0.30	-	0.04	97.8
VC	0.07	1.8	0.01	0.02	-	0.31	0.03	97.8

4.2. METHODS

4.2.1. HEAT TREATMENT AND CHARACTERISATION

Two different ferritic steel compositions were used in this study, both of which were supplied in a hot-rolled condition by Tata Steel in IJmuiden. The alloy compositions are given in Table 4.1. Both alloys are fully ferritic but were alloyed with titanium and vanadium, respectively, in order to maximise precipitation of TiC and VC nano-precipitates. Each steel was subjected to a short (SN) and long (LN) heat treatment in nitrogen atmosphere, to realise two different precipitate size distributions. The heat treatments consisted of a heating rate of 5 °C/min to temperatures of 700 °C for the TiC alloy and 650 °C for the VC, followed by isotherms of 2 hours for the SN and 20 hours for the LN treatment. The temperatures were chosen in order to keep the steels below the A_{c1} temperature for austenite formation [21]. Cooling down was performed at approximately 1 °C/min, which was limited by the furnace.

The as-received steels were machined into either 2 mm x 20 mm x 110 mm sheets for microstructural characterisation and Thermal Desorption Spectroscopy (TDS), or dog-bone specimens to use in tensile testing. All sheets and dog-bone

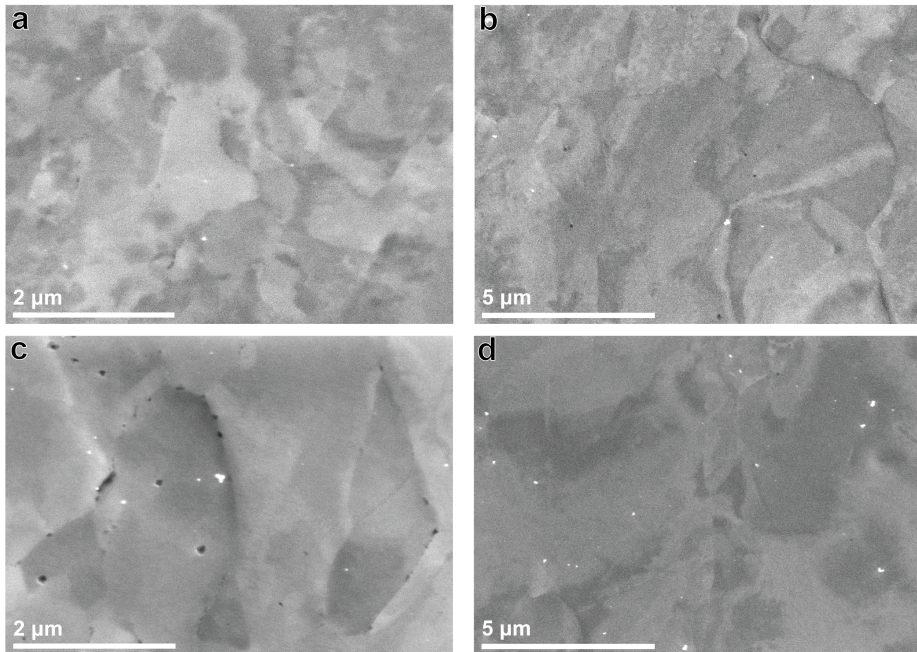


Figure 4.1.: SEM overview of the microstructures of a) TiC SN, b) VC SN, c) TiC LN and d) VC LN heat treatment conditions. Precipitates are visible in black.

specimens were sanded to a P1000 grit finish to ensure a repeatable surface finish before the heat treatments. Specimens for microstructural characterisation were cut from the sheets and further polished up to a $0.04 \mu\text{m}$ colloidal silica finish to allow for Scanning Electron Microscopy (SEM), Electron Dispersive X-ray Spectroscopy (EDS) and Electron Backscatter Diffraction (EBSD) analysis. EBSD and EDS were performed on a Thermo Fisher Scientific™ Helios™ G4 PFIB UxS SEM capable of performing simultaneous EBSD and EDS measurements. The acceleration voltage used was 20 kV , with a 3.2 nA probe current and a step size of 50 to 70 nm . EDS analysis of the fracture surfaces was performed at an acceleration voltage of 10 kV and a probe current of 1.6 nA . Transmission Electron Microscopy (TEM) analysis was performed to characterise precipitate sizes. This was done using a Thermo Fisher Scientific™ Cs corrected cubed Titan™ machine after polishing samples to $30 \mu\text{m}$ thickness and Ar^+ ion milling to electron transparency.

4.2.2. RESULTING MICROSTRUCTURES

Table 4.2 gives an overview of microstructural characteristics of the steels after heat treatment. All four microstructures were fully ferritic. Grain areas were obtained from EBSD, and precipitate sizes were obtained from TEM images where the size reported is the average size ($\sqrt{\text{length} * \text{width}}$) of manually measured precipitates.

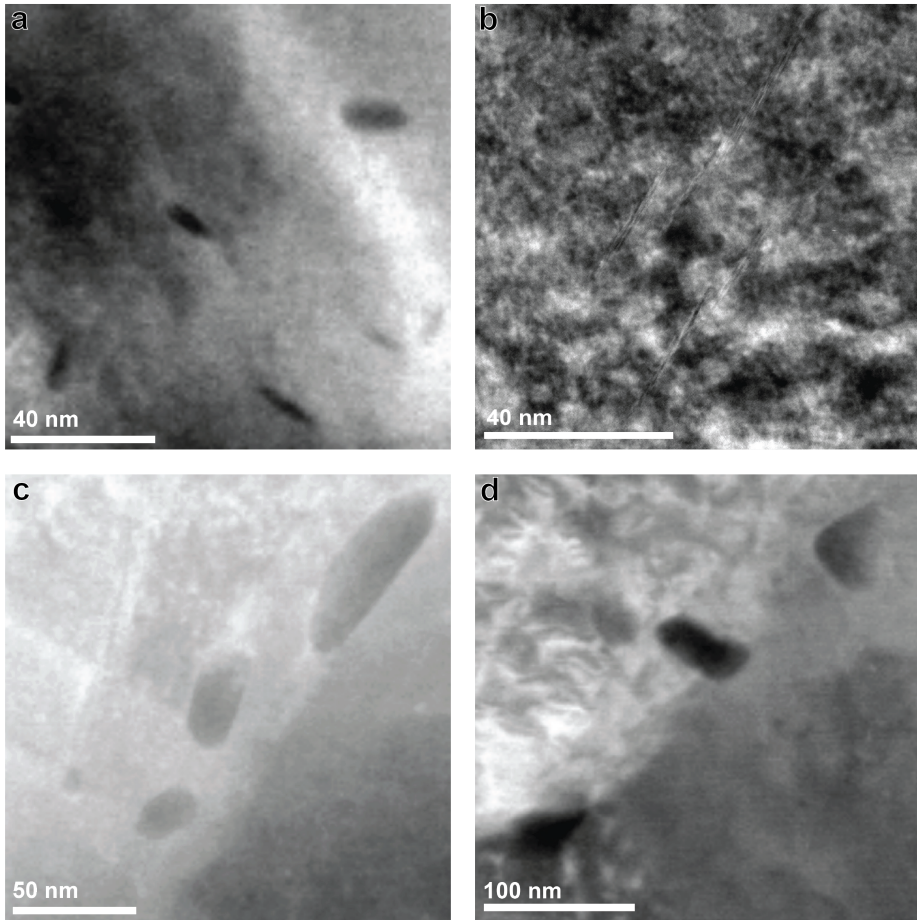


Figure 4.2.: High Angle Annular Dark Field (HAADF) TEM images of precipitates in a) TiC SN, b) VC SN, c) TiC LN and d) VC LN heat treatment conditions.

Since distributions of both the grain areas and precipitate sizes were very wide, they are reported in the way described in ASTM E1181 for randomly distributed grain sizes of large range [131]. A more in-depth description of microstructural characterisation was given in Chapter 3. The grain area in the TiC steel increases from an average of $3.8 \mu\text{m}^2$ in the TiC_{SN} to $5.0 \mu\text{m}^2$ in the TiC_{LN} condition. This is only a slight increase, which is attributed to grain boundary pinning by the nano-sized TiC precipitates found in TiC_{SN}. SEM microstructural overviews of both TiC_{SN} and TiC_{LN} are given in Figures 4.1a and 4.1c, respectively. It can be observed that the TiC_{LN} condition indeed contains a large amount of intergranular precipitates that have grown as a result of the long heat treatment and caused boundary pinning. The precipitates increase from 8.6 nm to 30.3 nm on average. At a size of approximately 4.2 nm , TiC nano-precipitates lose coherency with the matrix and misfit dislocations on the

Table 4.2.: An overview table with microstructural details for all heat treatment conditions. A minimum of 100 precipitates per steel were considered for the precipitate size and spacing measurements.

	HT	Hardness HV2	Grain area [μm^2]			Precipitate size [nm]			Precipitate spacing [nm]
			Low	Avg.	High	Low	Avg.	High	
TiC	SN	272 ± 3.1	0.1	3.8	160	2.8	8.6	290	44 ± 23
	LN	238 ± 1.6	0.1	5.0	192	5.7	30.3	235	50 ± 31
	Semi-coherent nano-carbides Homogeneously distributed incoherent >100 nm carbides								3.0 ± 2.0 μm
VC	SN	241 ± 1.2	0.1	12.5	223	3.8	9.9	522	24 ± 24
	LN	230 ± 0.7	0.1	24.9	231	2.5	17.6	349	49 ± 34
	Coherent nano-carbides, some semi-coherent in VC _{LN} Few incoherent >100 nm carbides								

matrix-precipitate interface are created [117]. Essentially all precipitates in TiC_{SN} and TiC_{LN} are therefore considered semi-coherent with the matrix. The average spacing between precipitates does not grow significantly after the heat treatments. Larger >100 nm precipitates that are fully incoherent with the matrix exist in the TiC steel from the as-received condition, which do not change in size during the heat treatments. These slightly skew the averages to higher numbers, which means that the majority of precipitates, even in TiC_{LN}, will be smaller than 30 nm. The average spacing for these large precipitates is 3 μm on average, which is 3 orders of magnitude higher than that of the small precipitates. The value is listed separately in Table 4.2 and does not change with heat treatment duration. Representative images of precipitates found in all four steels are shown in Figure 4.2. Since the grain size does not change with the longer heat treatment, the precipitate growth is responsible for the drop in hardness from 272 to 238 HV2 after the long treatment.

The VC steel has larger grains than its TiC counterpart, which do grow during the heat treatments, in contrast to those in the TiC steel. An average of 12.5 μm^2 in VC_{SN} grows to 24.9 μm^2 in VC_{LN}. The precipitates also increase in size from 9.9 nm to 17.6 nm on average. Vanadium carbides were observed in literature to be mostly coherent with the matrix up to a size of 20 nm [26], therefore most precipitates in VC_{SN} are considered coherent, as well as most precipitates in VC_{LN}. Precipitate spacing grows from an average of 24 nm to 49 nm. Large incoherent precipitates are much more scarce in the VC than in the TiC steel, so this number is a more accurate description of the average size of VC nano-precipitates present in the steels. Both grain and precipitate growth contribute to a drop in hardness from 241 to 230 HV2. SEM microstructural overviews of both VC_{SN} and VC_{LN} are given in Figures 4.1b and 4.1d, respectively. Table 4.2 includes a concise description of the precipitate distribution in all steels. EBSD representations of the microstructures as well as precipitate size

distributions have been shown in Figures 3.4 and 3.5.

4.2.3. IN-SITU SLOW STRAIN RATE TENSILE TESTING

In order to assess the amount of embrittlement in each steel, they were subjected to in-situ Slow Strain Rate Tensile (SSRT) tests in an electrochemical hydrogen charging environment. The setup that was designed for the test is shown in Figure 4.3a and the geometry of the tensile specimens is given in Figure 4.3b. The specimens were sanded with a P1200 grit paper before being submerged in a solution of 3.5 % NaCl as well as 3 g/L ammonium thiocyanate (NH₄SCN) to act as a recombination poison. Each specimen was charged with hydrogen at a current density of 1 mA/cm² for 2 hours prior to starting the test, with continued charging during the full duration of the test. Because of the design of the tensile grips, only the gauge length of the specimen was subjected to the current. The SSRT test was conducted at a crosshead displacement speed of 14.4 mm/h which corresponds to a maximum strain rate of 1·10⁻⁴s⁻¹ in the specimen gauge length. The tests were performed on a Zwick Z100 universal tensile tester with the strain being recorded using an Epsilon 4030 submersible extensometer. The bath and connectors were designed specifically for this research. Current was applied using a Bio-Logic VSP-300 potentiostat. Specimens were removed from the bath immediately after fracture, cleaned with demineralized water, dried with compressed air and stored in a freezer at - 86 °C until removed for TDS analysis. The strain at fracture of each specimen ($\epsilon_f^{H_2}$) was compared against that of non-hydrogen charged specimens (ϵ_f^{Air}) found in Chapter 3 and used to calculate the hydrogen embrittlement index *HEI*. The formula with which the *HEI* was calculated is listed in Equation 4.1.

$$HEI[\%] = \frac{\epsilon_f^{Air} - \epsilon_f^{H_2}}{\epsilon_f^{Air}} * 100\% \quad (4.1)$$

4.2.4. HYDROGEN ANALYSIS

In addition to post-mortem H analysis after the SSRT tests, each steel was also charged with hydrogen outside of the tensile testing environment to investigate the amount of hydrogen absorbed without any application of stress or strain. Sheet specimens subjected to the heat treatments were sanded with a P1200 grit paper to ensure a surface finish identical to that of the SSRT specimens before being charged in 3.5 % NaCl + 3 g/L NH₄SCN solution for 2 hours. Specimens were moved to the TDS analysis immediately after charging. Both the sheet specimens and the full SSRT specimens were subjected to TDS analysis in a Bruker G8 Galileo ONH analyser equipped with the IR07 infrared furnace for accurate temperature ramping. TiC specimens were measured up to 900 °C, the full range of the furnace, while VC specimens were ramped up to 700 °C because no H was desorbed above these temperatures for this steel. Heating rates of 1, 0.66 and 0.33 K/s were used in order to obtain peak shifting behaviour of the hydrogen desorption peaks. Fitting of peak

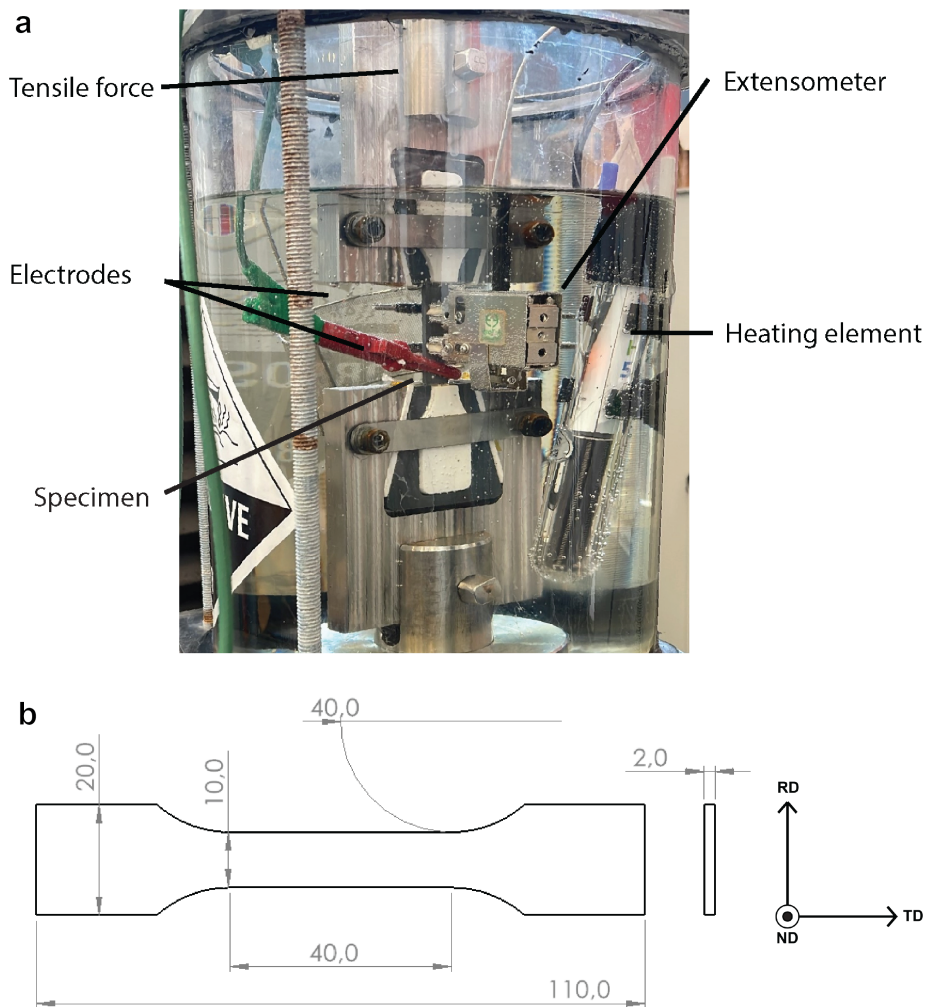


Figure 4.3.: a) Overview of the in-situ setup used for tensile testing and b) the dimensions (in mm) of the tensile specimen geometry used in this study.

temperatures obtained at different heating rates according to the simplified Kissinger equation [129], shown in Equation 4.2, allows for determination of activation energies for specific peaks that can be linked to microstructural hydrogen traps.

$$\frac{d \ln(\phi / T_{max}^2)}{d(1/T_{max})} = -\frac{E_A}{R} \quad (4.2)$$

In this equation T_{max} , ϕ , R and E_A are the peak temperature of a specific H desorption peak in K, the heating rate in K/s, the universal gas constant 8.3415

$J/mol^{-1}K^{-1}$ and the activation energy for hydrogen desorption of the specific hydrogen trap in kJ/mol , respectively. By fitting $\ln(\phi/T_{max}^2)$ to $(1/T_{max})$, E_A can be inferred from the slope.

4.3. RESULTS

4.3.1. HYDROGEN ABSORPTION

An overview of the hydrogen contents of all steels is given in Table 4.3, including activation energies calculated for desorption peaks of the non-strained samples which are shown in Figure 4.4. Overall, the TiC steels absorb more hydrogen than the VC steels, especially after the long heat treatment. All TiC steels contain a significant amount of hydrogen that is trapped at high temperatures, which was only found in one of the VC specimens. The amount of hydrogen that was released in the first desorption peak (chosen as 50 to 475 °C) was therefore calculated separately to compare the hydrogen trapped at low temperatures only. These values will be used to support further discussion in this article instead of the total hydrogen content. It becomes clear that with an absorbed H content of 2.18 wppm for TiC_{SN} and 1.82 wppm for VC_{SN}, the TiC steel absorbs more hydrogen at lower temperatures than the VC steel, and not all of the extra hydrogen absorbed by the TiC steels is that which is trapped at a high temperature. In both the TiC and VC steels, the SN steel absorbs significantly more H than the LN steel, which is likely a result of precipitate growth as well as grain growth which causes a reduction in grain boundaries available for trapping hydrogen. Activation energies obtained for the low temperature desorption peaks show good correspondence between SN and LN heat treatments. TiC_{SN} and VC_{SN} have similar energies of 14 and 19 kJ/mol while TiC_{LN} and VC_{LN} have energies of 37 and 27 kJ/mol , respectively. This suggests similar trap types between the two precipitate types, that change with heat treatment duration. The hydrogen trapped in the high temperature peaks above 500 °C was previously shown to be stored in large incoherent precipitates [21] and can be seen to be slightly reduced after the long heat treatment. It can be calculated from Table 4.3 to be 0.39 and 0.27 wppm for TiC_{SN} and TiC_{LN}, respectively, while it is only 0.19 for VC_{SN} and less than 0.01 wppm for VC_{LN}. Activation energies for the high temperature traps could only be determined for TiC_{SN} since the amount of hydrogen trapped in the other steels was insufficient to identify peaks at all heating rates. The energies obtained were 69 and 115 kJ/mol for two distinguished peaks that can be observed in Figure 4.6.

4.3.2. MECHANICAL BEHAVIOUR

In order to compare the mechanical behaviour of the specimens studied in this research, Figure 4.5 compares their SSRT curves to those obtained for their uncharged counterparts studied in Chapter 3. A more detailed overview of mechanical performance is given in Table 4.4. The specimens tested in-situ perform very similarly to the uncharged ones for the largest part of the tensile curve. No significant deviations in yield behaviour nor UTS are found except for experimental uncertainties.

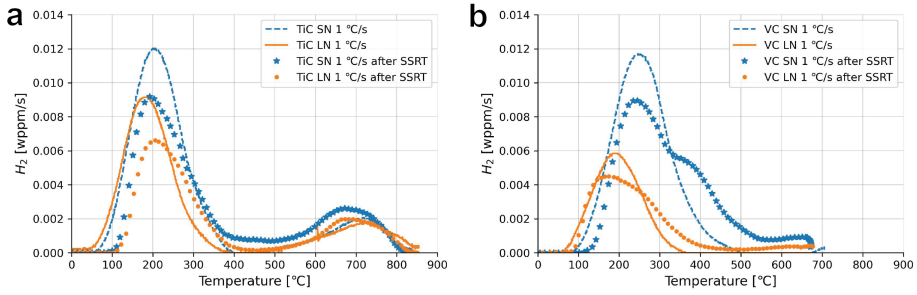


Figure 4.4.: TDS desorption curves of a) TiC and b) VC unstrained samples against the post-mortem sample including deformation.

Table 4.3.: Overview of the total amount of absorbed hydrogen, the amount of hydrogen in the low temperature desorption peaks (50 - 475 °C), the amount of hydrogen in high temperature peaks (>500 °C) and the activation energies obtained for the desorption peaks in the ex-situ charged samples.

HT Condition		Total H [wppm]	Low T peak H [wppm]	E_A [kJ/mol]	High T peak H [wppm]	E_A [kJ/mol]
TiC	SN	2.62 ± 0.32	2.18 ± 0.28	14 ± 4	0.39 ± 0.01	69 ± 7 115 ± 16
	LN	1.53 ± 0.17	1.26 ± 0.06	37 ± 3	0.27 ± 0.10	-
VC	SN	2.02 ± 0.03	1.82 ± 0.18	19 ± 5	0.19 ± 0.19	-
	LN	0.79 ± 0.04	0.79 ± 0.04	27 ± 8	< 0.01	-

A notable exception is TiC_{LN} , which has an early onset of necking that causes a lower UTS and higher HEI . In both cases for the VC steels, the longer heat treatment results only in a reduction in strength instead of an increase in ductility. This is true for both heat treatment durations. The largest effect of the in-situ hydrogen charging is observed as a reduction in strain at fracture ϵ_f . Both TiC_{SN} and VC_{SN} show an HEI value of around 15 %. VC_{LN} reduces in ductility by 19 %. TiC_{LN} , however, is evidently more embrittled with an HEI value of 37 %. This condition shows both a larger ductility without hydrogen, as well as the lowest ductility with hydrogen.

4.4. DISCUSSION

Characterising the specific microstructural features responsible for trapping hydrogen is often complicated by overlap of different desorption peaks [40]. Other than hydrogen traps in precipitate features, dislocations and grain boundaries often show desorption peaks at near identical temperatures [22, 105]. In this view, the TiC steel provides a good study case since the grain structure is not significantly changed between the SN and LN heat treatments. The reduction from 2.18 to 1.26 wppm of absorbed hydrogen at low temperatures can therefore confidently be ascribed to a

Table 4.4.: Overview of the 0.2% proof yield strength $\sigma_{y, 0.2\%}$, UTS, Onset point of necking ϵ_{UTS} and strain at break ϵ_f for all heat treatment conditions. Errors are standard deviations.

HT Condition	$\sigma_{y, 0.2\%}$ [MPa]	UTS [MPa]	ϵ_{UTS} [%]	ϵ_f [%]	HEI [%]	
TiC	SN	633 ± 13	711 ± 3	8.7 ± 0.4	12.9 ± 0.5	15.3 ± 6.4
	LN	480 ± 9	575 ± 14	7.7 ± 0.3	11.1 ± 0.8	37.0 ± 10.5
VC	SN	658 ± 6	739 ± 4	11.4 ± 0.3	14.1 ± 0.7	14.7 ± 11.6
	LN	570 ± 1	648 ± 6	11.3 ± 1.7	15.0 ± 1.4	18.7 ± 12.3

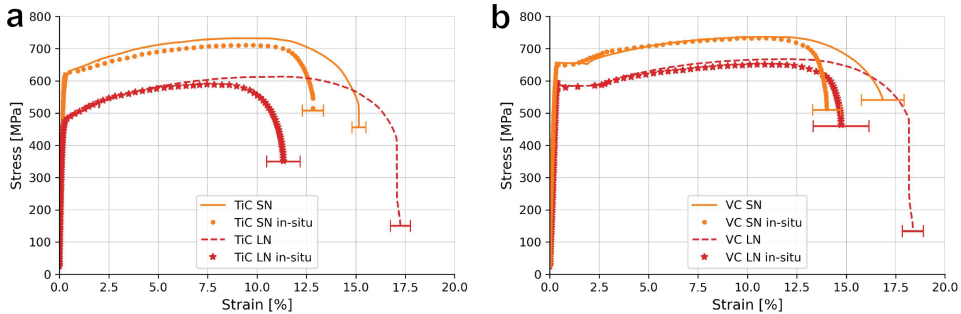


Figure 4.5.: Tensile curves of a) TiC and b) VC specimens tested in-situ during electrochemical hydrogen charging in comparison with uncharged specimens. Errors are standard deviations in fracture strain. Uncharged data was obtained in Chapter 3.

difference in trapping in or around the precipitates. The obtained activation energy of 14 ± 4 kJ/mol for TiC_{SN} is close to values obtained by DFT studies. Sagar et al. [96] found values of 11.5 kJ/mol (-0.12 eV) and 10.5 kJ/mol (-0.11 eV) for the activation energy of the tetrahedral interstices on the coherent precipitate/matrix interface and in the first iron layer, respectively. These fall within the range of 18 ± 12 kJ/mol found for the more general coherency strain field of TiC by Di Stefano et al [118]. The desorption peak of TiC_{LN} was measured as 37 ± 3 kJ/mol, which matches with several reported values from both DFT and experimental studies on the activation energy of hydrogen trapped within misfit dislocations on the semi-coherent interface. Di Stefano et al. calculate this value as 47 kJ/mol (-0.49 eV) [118] and Hammer et al. [138] calculate it as approximately 43 kJ/mol (-0.45 eV). An experimental value of 43 kJ/mol was also obtained in Chapter 3 where identical steels were charged in a high temperature H_2 environment [21].

Activation energies obtained for the VC steel were remarkably similar to that for the TiC steel. The VC_{SN} condition traps hydrogen with an activation energy of 19 ± 5 kJ/mol. Though modelling results on VC are more scarce, values of between 12 and 17 kJ/mol (-0.13 & -0.18 eV) were obtained by several authors for trapping

sites in the iron lattice near the matrix/precipitate interface [103, 118, 138]. Hammer et al. furthermore obtained a value of approximately $29 \pm 6 \text{ kJ/mol}$ (-0.30 eV) for the activation energy of hydrogen trapped in a misfit dislocation core on the semi-coherent interface. This matches well with a value of $27 \pm 8 \text{ kJ/mol}$ measured for the VC_{LN} condition in this research. The fact that values between SN and LN conditions in both steels are similar indicates that the trapping behaviour between the TiC and VC nano-carbides is similar as well. The hydrogen is stored in the first iron layers around the interface of small (semi-)coherent carbides after the SN treatment, but in misfit dislocation cores on the interface of semi-coherent carbides after the longer LN treatment when precipitates have grown. These are all interface traps. Since less interface is available as the nano-carbides increase in size this explains the reduction in absorbed hydrogen after the longer heat treatment for for TiC steel and partly for the VC steel. The reduction from 1.82 to 0.79 wppm in VC_{LN} is not only a result of reduced VC interface trapping, but also of a reduced grain boundary density in VC_{LN} resulting from grain growth. Grain boundaries have been shown to appear at similar desorption temperatures to what was measured in this research [22], so they can be expected to play a role even though their behaviour was masked by the desorption peak of the carbides.

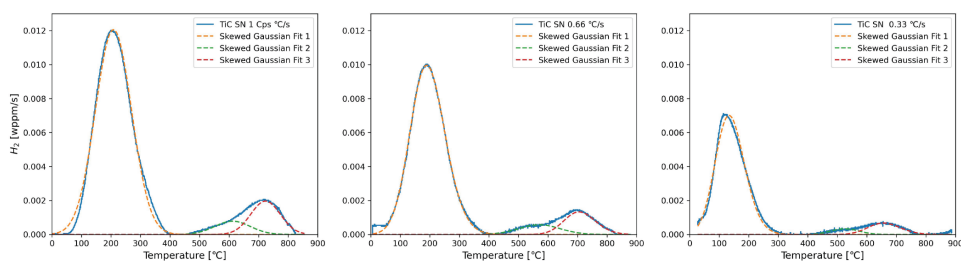


Figure 4.6.: Deconvoluted TDS peaks for all heating rates in the TiC_{SN} steel.

Both TiC_{SN} and TiC_{LN} are shown in Figure 4.4 to trap H at higher temperatures as well. Figure 4.4a shows the deconvoluted high temperature peaks for TiC_{SN} , which were calculated to have activation energies of 69 and 115 kJ/mol , respectively. Chapter 3 identified the hydrogen that desorbs at high temperatures to be trapped inside the bulk of large incoherent carbides [21], although no activation energies for these traps were obtained in that work. Electrochemical hydrogen charging at room temperature cannot overcome the diffusion barrier of the incoherent precipitate/matrix interface, which means that these traps are not affected by the charging in this work. The hydrogen is already present in the as-received material. The value of $115 \pm 16 \text{ kJ/mol}$ that is found here for the high temperature peaks corresponds well with numerically obtained values of 105 to 113 kJ/mol for H trapped in C-vacancies inside the precipitate bulk [96, 120]. The same trap has been studied experimentally, where energies of 80 to 90 kJ/mol were found [27, 112]. Incoherent TiC precipitates in general were found to have a wider range of trapping energies anywhere between 53

and 145 kJ/mol through different analytical means that could explain their difference [22, 101, 102]. Wei and Tsuzaki observe trapping energies for H trapped in incoherent TiC to range from 68 to 137 kJ/mol depending on austenization temperature and consequently precipitate size [27]. However, a difference in precipitate size does not indicate a difference in trap type, so varying activation energies are not expected. There is still uncertainty towards the nature of differently obtained activation energies for the seemingly identical trap site of the C-vacancy. The influence of connected vacancy networks is sometimes discussed in literature as an explanation for lower activation energies [112, 118], but a conclusive answer is not yet found.

Figure 4.4b shows peak broadening for the VC spectra obtained post-mortem after the SSRT test, and even the appearance of an extra shoulder in the desorption curve for VC_{SN} . Although the appearance of an extra peak suggests the creation of a new hydrogen trap, the activation energies for the first and second peaks were found as 17 and 21 kJ/mol . The full deconvoluted peaks can be found in Figure A.1. These energies are so similar that it is difficult to assign separate microstructural features to both individually. It is more likely that this is an effect of a high degree of plastic deformation, which was observed in DP1000 steel by Drexler et al. as peak broadening with increasing plastic strain [139]. A high degree of plastic deformation retards hydrogen diffusion from the bulk which delays the appearance of the desorption peak to higher temperatures. Since the coherent VC precipitates present in VC_{SN} and to a smaller degree in VC_{LN} were of a smaller size as well as more elongated than those seen in the TiC steels, they play a larger role in dislocation accumulation and precipitate strengthening. This is the main cause of the similar strength of the VC steels to that of the TiC steels, although the grain size is much larger in the VC steels. Increased dislocation accumulation around VC precipitates could therefore lead to a retardation in the desorption peak after straining to a larger degree that is not observed in the TiC steels. Since the average precipitate spacing in VC_{SN} is lower than in all other steels at 24 nm , these precipitates provide a larger barrier for dislocation movement. This causes a larger dislocation accumulation around the precipitates, such as observed by Gong et al. [140], which causes the most retardation of H desorption that shows in the TDS curve as a second peak. However, because the trap is still the precipitate itself, the activation energy does not change.

Both the TiC and VC steels are ductile steels without a large amount of strain hardening. Judging from Figure 4.5 and Table 4.4, the only observed effect is that of a reduction in fracture strain as indicated by the HEI . Both VC steels, as well as TiC_{SN} embrittle by 15 to 20 %. TiC_{LN} instead embrittles by 37 %, almost twice as much as all other steels. In order to investigate the reason, more metrics should be studied. Table 4.5 lists the UTS, onset points of necking and embrittlement indexes calculated for both metrics (HEI_{UTS} and HEI_{Neck} , respectively) in the same way as listed in Equation 4.1. The benchmark values on uncharged specimens used for the embrittlement indexes were obtained in Chapter 3 [21]. One important observation from this table is that the HEI_{Neck} is negligible for both VC steels, and insignificantly changed for TiC_{SN} . There is no evidence of an early onset of necking in these steels, meaning that the

Table 4.5.: Comparison of the UTS and onset point of necking ϵ_{UTS} against uncharged benchmark specimens from Chapter 3, as well as the embrittlement indexes calculated for each compared to the overall HEI[21].

HT Condition		UTS	UTS	HEI _{UTS}	ϵ_{UTS}	ϵ_{UTS}	HEI _{Neck}
		[MPa] Bench	[MPa]	[%]	[%]	[%]	[%]
TiC	SN	739 ± 18	711 ± 3	3.9 ± 2.9	9.5 ± 0.3	8.7 ± 0.4	8.24 ± 8.2
	LN	650 ± 39	575 ± 14	11.6 ± 8.5	11.2 ± 0.6	7.7 ± 0.3	30.6 ± 8.8
VC	SN	744 ± 7	739 ± 4	0.6 ± 1.5	10.8 ± 1.0	11.4 ± 0.3	-6.0 ± 12.2
	LN	674 ± 12	648 ± 6	4.0 ± 2.6	11.9 ± 0.4	11.3 ± 1.7	5.5 ± 17.8

absorbed hydrogen does not impact the ductility of these steels up until the point of necking. All reduction in ductility that constitutes the hydrogen embrittlement takes place after the point of UTS e.g. as accelerated necking. In contrast, the onset of necking is reduced by 30.6 % in TiC_{LN} after in-situ testing compared to the benchmark, which is of the same order as the 37 % total embrittlement of this steel. As a consequence of this early onset of necking, the UTS of TiC_{LN} is reduced by 11.6 % compared to the benchmark. The other three steels do not show any significant reduction of UTS outside of any variability that is expected between different sets. What this behaviour indicates is that the eventual localisation of plastic deformation is the governing factor in embrittlement for these steels. In order to elucidate exactly why TiC_{LN} behaves so differently, the fracture mechanisms need to be studied.

Figures 4.7a and b, which show frontal view of the post-mortem SSRT specimens, display significant side-cracking in TiC_{LN} compared to that in VC_{LN}. This indicates a reduced resistance to crack initiation and growth in the TiC steel, which serves as a cause for increased HE. Figures 4.8a and b show SEM fractographic images of the fracture surfaces of the same samples. The highlighted area corresponds to areas of brittle fracture around the edges of the tensile specimens that were in contact with the electrolyte, as is often seen in in-situ tests [43, 141, 142]. A higher magnification image of the brittle zone in TiC_{LN} is given in Figure 4.8c, where it can be observed that fracture is exclusively intergranular (IG) in this region. Extensive secondary cracking can be seen and all facets are of a size corresponding to the grain size. Although behaviour in VC_{LN} is very similar, as can be seen in Figure 4.8d, this fracture surface still exhibits some transgranular (TG) fracture that contains ridges characteristic of the quasi-cleavage (QC) fracture surface [71]. These facets are larger than any of the ones observed in TiC_{LN} which corresponds to the larger grain size found in the VC steel. In the hydrogen embrittlement model as proposed by Wasim et al. [79], embrittled fracture surfaces exhibit more IG fracture with increasing hydrogen content. This matches the higher hydrogen content of TiC_{LN} (1.26 wppm) compared to VC_{LN} (0.79 wppm). However, the hydrogen content is clearly not the only factor governing the emergence of intergranular fracture, since TiC_{SN} has an even higher H content but a much lower HEI.

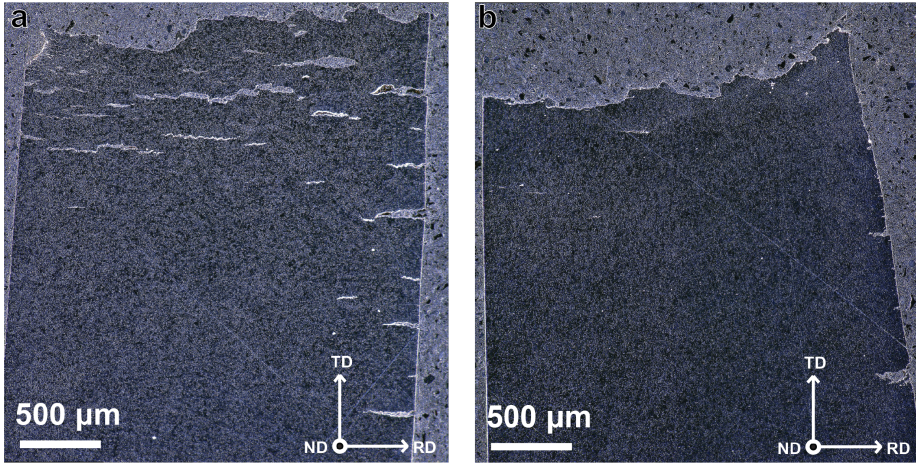


Figure 4.7.: Front views of post-mortem specimens from a) TiC_{LN} and b) VC_{LN} . The top surface in this figure is the fracture surface of the tensile specimens, crack that can be observed are secondary cracks on the side surfaces of the specimens.

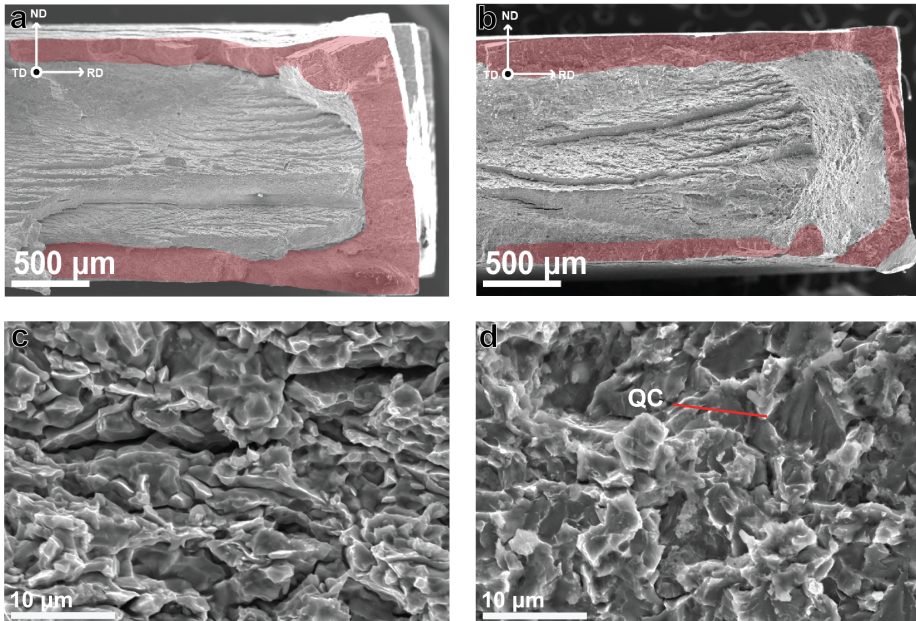


Figure 4.8.: Fractographic images of a, c) TiC_{LN} and b, d) VC_{LN} . Highlighted areas in a) and b) correspond to brittle fracture surface. Quasi-Cleavage (QC) fracture features are indicated in d).

Higher magnification SEM fractography was performed in order to investigate the nature of increased IG fracture in Ti_{CLN} compared to the other steels. Figure 4.9a shows an image of precipitates on a cracked grain boundary from the Ti_{CLN} steel, of which an EDS line scan is shown in Figure 4.9b. The precipitates on the grain boundary are identified as TiC , which shows that the intergranular fracture surface is in fact localised to boundaries that contain precipitates. A reference image of an intergranular surface of Ti_{SN} is shown in Figure 4.9c which does not contain any visible intergranular carbides. The fact that Ti_{CLN} contains a high degree of intergranular precipitates that are present on the fracture surface can explain the increased tendency for Ti_{CLN} to show IG fracture as compared to the other steels. However, Ti_{CLN} is not the only surface on which larger IG precipitates were observed. Figure 4.9d shows an occurrence of IG precipitation on the surface of VC_{LN} , although these precipitates could not be identified as VC definitively. This means that the localisation of fracture to the precipitate boundaries is not specific to TiC , but the fact that Ti_{CLN} contains many more causes its higher embrittlement.

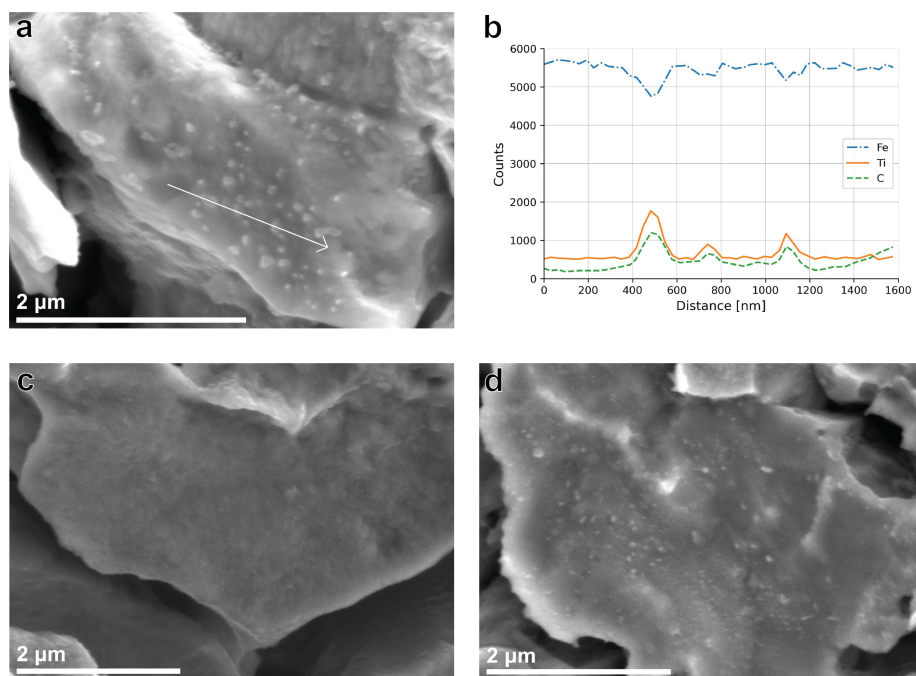


Figure 4.9.: In-depth fractographic observation of a) High magnification of TiC precipitates on a grain boundary on the Ti_{CLN} fracture surface. b) EDS linescan of the line segment shown in (a). c) Facet not showing any sign of precipitates on a Ti_{SN} IG fracture surface. d) Intergranular precipitates on the VC_{LN} fracture surface.

Furthermore the role of the larger $>100\text{ nm}$ incoherent precipitates should be

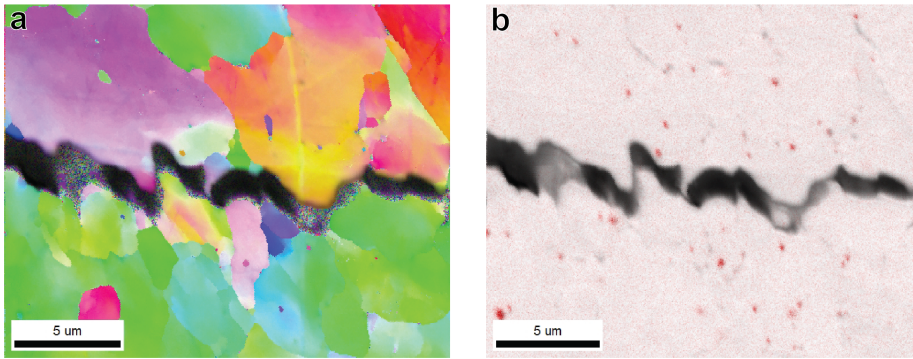


Figure 4.10.: a) An Inverse Pole Figure (IPF) of a secondary crack on the side surface of a TiC LN specimen, and b) an Electron Dispersive X-ray (EDS) image of the same area in (a) where Titanium is displayed in red.

discussed. Combined EBSD and EDS analysis was performed to investigate the presence of these precipitates around secondary cracks, the results of which are shown in Figure 4.10. EDS in Figure 4.10b furthermore shows the presence of homogeneously distributed TiC precipitates of sizes >100 nm. Although these precipitates are not localised around the crack formation, they have been observed to occasionally appear on the fracture surface as shown in Figure 4.11a. Large incoherent precipitates are therefore explained to not necessarily localise fracture, but to cause increased IG fracture if they are present on grain boundaries.

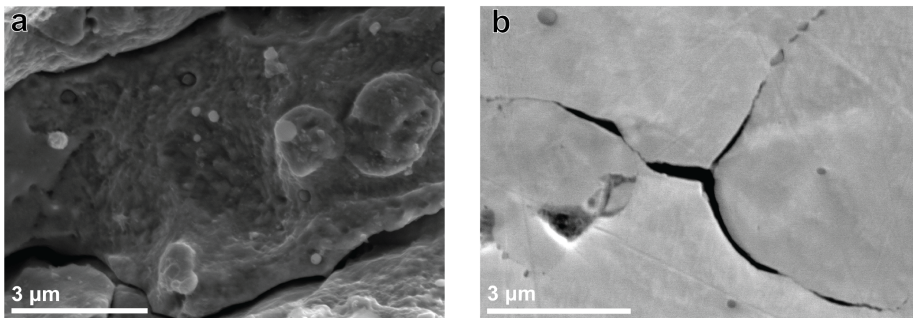


Figure 4.11.: SEM images of a) Observed incoherent TiC precipitates on an intergranular fracture surface. b) Nucleated secondary crack on a triple point boundary. Both images were obtained from the TiC_{LN} steel.

The role of intergranular precipitates in hydrogen fracture was investigated previously in literature. Elkot et al. investigated an austenitic high Mn-steel containing κ -carbides and concluded that IG fracture is facilitated on boundaries containing a high concentration of carbides [143]. They draw parallels to a study by Koyama et al.

on a similar steel [144]. The mechanism proposed by Koyama et al. proposes crack initiation on triple point boundaries, followed by preferential crack growth towards boundaries containing a high hydrogen concentration due to slip localisation. In the study by Koyama et al., the carbides cause increased slip localisation from the matrix, whereas Elkot et al. find them to be most detrimental when they are present on grain boundaries. The carbides act as blockages for dislocation cross-slip along grain boundaries and instead cause dislocation pile-ups that lead to void formation in combination with hydrogen. The void formation eventually causes enhanced IG fracture. Elkot et al. argue that instead of slip bands observed by Koyama et al. being the precursor to fracture, they are instead formed upon crack propagation.

4 Crack initiation on triple-point grain boundaries is something that was observed in this work as well, as indicated in Figure 4.11b which shows a secondary nucleated crack on a triple point boundary in TiC_{LN} . This figure also shows crack propagation along grain boundaries that contain precipitates. The mechanism as discussed by Elkot et al. is therefore likely also active in this steel although it contains different precipitates. The reason that this mechanism is only active for TiC_{LN} is because of the high amount of intergranular precipitates of increased size compared to those in TiC_{SN} . These form as a result of two mechanisms. Firstly, grain boundaries migrate during the heat treatment, but get pinned by existing nano-precipitates that are until then only present in the grain interior. This Zener pinning is also responsible for the negligible growth in grain size between TiC_{SN} and TiC_{LN} . This results in an increased amount of precipitates at grain boundaries. Secondly, the grain boundary precipitates undergo accelerated growth compared to those in the grain interior. It is clearly visible from SEM observations such as those in Figure 4.1c that interior precipitates are not visible at similar magnifications that reveal grain boundary precipitates. Precipitates present on the grain boundaries act as barriers to dislocation movement and dislocation pileup around the precipitates occurs. This localised plastic deformation, in combination with the hydrogen present, causes fracture around the precipitate and accelerates IG cracking compared to a steel where the precipitates are present in the grain interior such as TiC_{SN} . This mechanism reveals itself in the tensile curve as an early onset of necking, although the actual plastic deformation is happening on the grain boundaries. Although it has been found that smaller grains can be beneficial to increase HE mitigation [145], intergranular presence of carbides with reversibly trapped hydrogen could counter this effect and weaken the grain boundaries instead, causing increased HE. This process is shown in four steps in Figure 4.12. Whereas nano-carbides present inside grains are therefore beneficial, carbides present on the grain boundaries could cause increased HE instead. Excessive grain boundary precipitation should therefore be avoided when designing nano-steels for hydrogen service.

4.5. CONCLUSIONS

Through this research, some key aspects of hydrogen embrittlement were studied. In-situ mechanical testing in an electrochemical hydrogen charging environment

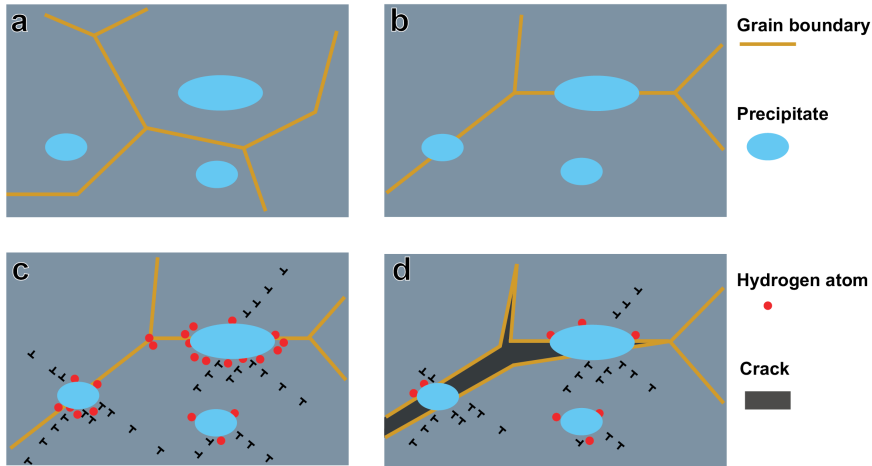


Figure 4.12.: Proposed model for enhanced hydrogen embrittlement by grain boundary precipitation. The a) starting microstructure, undergoes grain growth after which the b) grain boundaries are pinned. c) the precipitates accumulate dislocations and attract hydrogen that d) weakens the precipitate/grain interface and cause intergranular fracture.

allowed for obtaining the optimal precipitate type and size that retains mechanical properties as much as possible during hydrogen loading, namely the VC steel with a high density of coherent nano-carbides. Furthermore, the adverse effect of intergranular precipitates in relation to hydrogen fracture was discussed. A model was proposed to describe the creation of grain boundary precipitates and their effect on the hydrogen embrittlement of steels in contrast to the beneficial effect of nano-precipitation within grains. The following conclusions can be drawn from this work:

- Nano-carbides trap hydrogen in the iron layers near the interface with an activation energy of $14 - 19 \text{ kJ/mol}$, or inside the misfit dislocation core with an activation energy of 27 kJ/mol or higher. Since this hydrogen is stored on the interface between the precipitate and the matrix, the amount of absorbed hydrogen decreases with increasing precipitate size.
- Hydrogen charged through electrochemical means is trapped reversibly. Incoherent TiC precipitates of $>100 \text{ nm}$ in size trap hydrogen irreversibly in C-vacancies with energies of 69 and 115 kJ/mol . The irreversibly trapped hydrogen is present in the material before the heat treatment, and these traps are not influenced by the electrochemical charging.
- After in-situ Slow Strain Rate Tensile testing, VC_{SN} , TiC_{SN} and VC_{LN} are all embrittled by 15 to 20 %, while TiC_{LN} is embrittled by 37 %.

- The reduction in fracture strain is concentrated to the region of necking in the tensile curve for all steels except TiC_{LN} , which has an earlier onset of necking. Plastic strain localisation is therefore the governing factor for HE in these steels.
- The increased embrittlement in TiC_{LN} is shown to be a result of TiC nano-precipitates present on grain boundaries. These cause dislocation pileup, trap hydrogen there and consequently cause intergranular fracture around the precipitates that results in macroscopic brittle behaviour.
- VC_{SN} retained the highest strength and ductility out of all four steels while absorbing 2.0 wppm of hydrogen. This is therefore the optimal condition for use in both gaseous and liquid hydrogen environments.

5

EFFECT OF PLASTIC DEFORMATION ON THE HYDROGEN EMBRITTELEMENT OF FERRITIC HIGH STRENGTH STEEL

**Tim BOOT, Pascal KÖMMELT, Ruud (W.A.) HENDRIKX,
Amarante (J.) BÖTTGER, Vera POPOVICH**

The effect of hydrogen charging during plastic deformation was investigated on a ferritic steel containing TiC nano-precipitates. Specimens were subjected to a slow strain rate tensile test (SSRT) up to 0, 1 or 3% plastic engineering strain, held until a total duration of two hours to saturate with hydrogen, then fast fractured. The specimens pre-strained elastically absorbed 2.36 wppm of hydrogen, which increased to 3.69 wppm for 3% plastic strain. Only 0.72 wppm is stored in non-dislocation traps such as precipitates, grain boundaries and lattice sites which makes dislocations the main contributor to hydrogen trapping. The increased hydrogen uptake did not lead to a decrease in fracture strain, which remained between 6 and 10% for all pre-strains, compared to 60% for full SSRT tests that were charged for a shorter time. This research highlights the necessity of high plastic strains and the presence of hydrogen in the environment during crack growth to cause HE in ductile steels.

This chapter has been published in NPI Materials Degradation **9**, 39 (2025).

5.1. INTRODUCTION

The automotive industry is a considerable contributor to global CO₂ emissions, of which a large part is correlated to vehicle weight [3, 4]. Reducing vehicle weight will therefore lead to CO₂ reductions, but this has to be done without compromising passenger safety. For this reason, the industry has been on the forefront of using Advanced High Strength Steels (AHSS), which allow for critical parts in the vehicle to be manufactured from thinner material while retaining good mechanical properties to guarantee safety [6, 7]. Good formability of these steels is required to obtain the complex geometries of structural car parts. Many high strength steels contain microstructural features that cause HE by attracting hydrogen which causes a reduction in mechanical properties and potential sudden fracture [12–17]. Examples of these are hard phases, interfaces or regions of stress and/or strain concentrations [21–24]. Accumulation at these areas is why diffusible hydrogen is the primary cause of HE [24, 34, 105, 111, 114, 115, 136]. One solution in automotive steels is the use of nano-carbide precipitates in a ferritic matrix to realise steels with a high strength as well as ductility without relying on large amounts alloying elements. An added benefit of using nano-carbides is that they provide a mechanism for increasing resistance to Hydrogen Embrittlement (HE) by providing strong hydrogen trapping sites, without compromising on overall steel strength [22, 27, 34, 67, 100, 105, 111–113].

The effects of precipitate type and size on HE were the focus of our previous research that was discussed in Chapters 3 and 4 [21, 134]. There it was shown that large incoherent carbides provide strong hydrogen traps that do not cause HE, but that these traps cannot be charged at room temperature. The best performance was found in the case where nano-sized precipitates were present only in the grain interior [21]. In this case HE was minimal and the only loss in ductility was detected after the onset of necking, whereas the material behaviour was unchanged at low strain. Park et al. find similar results in a study where pre-strained specimens were subjected to Slow Strain Rate Tensile (SSRT) tests in hydrogen and their specimens show accelerated fracture only after the point of maximum stress [146]. HE was found to be most significant for specimens that had undergone strain hardening before being charged with hydrogen. Their results are supported by Li et al. who subject U-bent specimens to an acidic environment in a static test to observe the duration until fracture [82]. They find that fracture only happens in specimens strained until near the bending limit. Embrittlement in these studies is only seen in samples that are strained to the load limit. Takai et al. investigated the effect of straining during hydrogen charging, then unloading and annealing out the hydrogen before loading again to fracture [147]. They found that specimens that were strain hardened in hydrogen, but fractured without hydrogen, still showed a reduction in ductility compared to specimens only strained in air. Hydrogen charging during strain hardening is thus suggested to induce damage in the microstructure that reduces its total ductility regardless of whether hydrogen is being charged at the load limit. The discrepancy between these different studies raises the question whether the phenomenon of HE is only present at high plastic strains or whether it can be affected by hydrogen charged at low plastic strains.

It is known that straining during hydrogen charging increases hydrogen uptake. An increase in plastic deformation has the effect of increased hydrogen absorption since the defects that are created, such as dislocations and vacancies, provide hydrogen trap sites [139, 147–149]. Moreover, the presence of hydrogen during straining can also increase the creation of defects, which further aggravates HE. This is explained in the Hydrogen Enhanced Strain Induced Vacancy (HESIV) model proposed by Nagumo [76, 77]. Drexler et al. even found a hydrogen uptake of 9.09 wppm after straining a DP600 steel during hydrogen charging versus only 3.48 wppm after straining in air [139]. It can therefore be expected that straining during hydrogen charging affects HE since it induces a higher hydrogen absorption, although the local hydrogen concentration has been found to decrease temporarily upon the onset of dislocation motion by Fukunaga [150].

This work studies the effect of only the hydrogen that is absorbed during strain hardening to answer whether or not straining up to the load limit is required to induce HE. The approach is to strain a ferritic high strength steel to several degrees of plastic strain during an SSRT test and charge it with hydrogen until saturation. The hydrogen uptake is measured using Thermal Desorption Spectroscopy (TDS), before specimens are fast fractured to inhibit any further uptake of hydrogen at high plastic strains. The results are compared to both specimens strained in air and specimens strained in SSRT while hydrogen charging until fracture, and the hydrogen is correlated to deformation by both X-ray Diffraction (XRD) and Electron Backscattering Diffraction (EBSD) measurements to obtain a comprehensive understanding of the fracture mechanisms.

5.2. METHODS

5.2.1. HEAT TREATMENT AND MICROSTRUCTURE

Table 5.1.: Summarised alloy contents of the TiC alloy in weight %.

	C	Mn	Al	Si	Ti	Balance Fe
TiC	0.07	1.75	0.01	0.01	0.30	97.86

The steel used in this research was cast by Tata Steel in IJmuiden. The composition was measured on a Panalytical Axios Max Wavelength Dispersive X-ray Fluorescence (WDXRF) instrument and is shown in Table 5.1. This composition was chosen to obtain a ferritic microstructure with finely dispersed TiC nano-precipitates for which the atomic ratio of Ti:C was kept as close to 1:1 as possible. The steel was heat treated by the same process as used in the previous chapters in this thesis, which consists of a heat treatment in pure N₂ at 700 °C for 2 hours. This time excludes a warm-up at 5 °C/min and a cooling-down that was furnace limited at approximately 1 °C/min. Before the heat treatment, each specimen was sanded to a P1000 grit finish. The resulting microstructure can be observed in

Figure 5.1a, and Figure 5.1b shows the histogram of precipitate sizes measured using TEM. The average grain area is $3.8 \mu\text{m}^2$, but extremes can be found on both the low and high ends. The sizes were therefore chosen to be listed in Table 5.2 according to the ASTM E1181 standard for randomly distributed grain sizes of large range the total range of observed grain areas was between 0.1 and $160 \mu\text{m}^2$.

Precipitate sizes ($\sqrt{\text{length} \cdot \text{width}}$) and spacings were obtained using Transmission Electron Microscopy (TEM), [21], and are also listed in Table 5.2 by the same standard. Over 100 precipitates were measured manually on a Thermo Fisher Scientific™ Cs corrected cubed Titan™ TEM. The critical size for TiC precipitates to lose coherency with the iron matrix is 4.2 nm , which means that with an average size of 8.6 nm and an average spacing of 44 nm , virtually all precipitates in the steel are semi-coherent with the matrix [27]. Larger precipitates with sizes of $>100 \text{ nm}$ were also observed, but they are much more sparse with an average spacing of $3 \pm 2 \mu\text{m}$. These were previously shown to not have any effect on fracture, even when charged with hydrogen [21]. The largest precipitate observed was 290 nm in size.

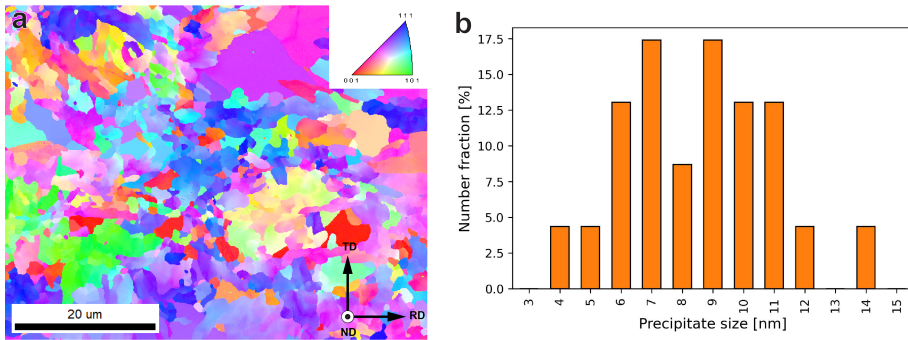


Figure 5.1.: a) An Inverse Pole Figure map of the microstructure of the undeformed steel, and b) a histogram showing the the distribution of semi-coherent precipitate sizes.

5.2.2. IN-SITU MULTI-STEP TENSILE TESTING

All tests performed for this research were conducted in a custom designed setup to allow for in-situ hydrogen charging during tensile loading. The setup and specimen geometry are shown in Figure 5.2. The specimens are submerged in a $3.5\% \text{ NaCl} + 3 \text{ g/L}$ ammonium thiocyanate (NH_4SCN) solution for the duration of the test to allow for hydrogen charging. The charging is performed galvanostatically with a current density of 1 mA/cm^2 for the entire duration of the test. A heating element is used to keep the basin at a constant temperature of $25 \text{ }^\circ\text{C}$. Before testing, each specimen is sanded up to P1200 grit for a repeatable surface finish. The test itself consists of three steps, which are displayed in Figure 5.3. The first step is a slow strain rate tensile (SSRT) test at a rate of $4 \cdot 10^{-5} \text{ s}^{-1}$ up to a pre-determined level of either stress or strain. The crosshead position is then put on hold while charging is

Table 5.2.: Microstructural details for all heat treatment conditions. A minimum of 100 precipitates were considered for the precipitate size and spacing measurements.

Hardness HV2	Grain area [μm^2]			Precipitate size [nm]			Precipitate spacing
	Low	Avg.	High	Low	Avg.	High	
272 ± 3.1	0.1	3.8	160	2.8	8.6	290	
Semi-coherent nano-carbides							44 ± 23 nm
Homogeneously distributed incoherent >100 nm carbides							3.0 ± 2.0 μm

continued until the total test duration reaches 2 hours, which was calculated as the saturation time for hydrogen charging of this steel in Chapter 4 [134]. Finally the specimen is subjected to a faster crosshead displacement of 10 mm/min until fracture which corresponds to a strain rate of $4.2 \cdot 10^{-3} \text{s}^{-1}$. This is done to avoid additional hydrogen entry into the steel during the fracture phase of the tests as well as to minimise the role of hydrogen diffusion during the fracture step. Any influence of hydrogen is thereby isolated to hydrogen absorbed during the first two steps of the test. The three threshold levels chosen were 0%, 1% and 3% plastic strain, where 0% was set to 80% of the 0.2% proof yield strength of the uncharged specimens taken from Chapter 4 [134]. Some specimens were subjected to a one step SSRT tests which consisted of a strain rate of $4 \cdot 10^{-5} \text{s}^{-1}$ until fracture, which have been designated as SSRT. Other than that, benchmark specimens were tested at a similar strain rate without any hydrogen charging. The extent of HE was calculated using the fracture strains as per Equation 5.1 and listed as the Hydrogen Embrittlement Index (HEI). Here ϵ_f^{Air} and $\epsilon_f^{H_2}$ designate the fracture strains of uncharged benchmark SSRT specimens and hydrogen charged specimens, respectively. Immediately after fracture of each specimen, both fractured halves were removed, rinsed with demiwater, dried with compressed air and cleaned in the ultrasonic bath in isopropanol for 5 minutes. All tests were performed using a Zwick Z-100 universal tensile tester and hydrogen charging was performed using a Bio-Logic VSP-300 potentiostat. Strain was measured using a submersible Epsilon 4030 extensometer.

$$HEI[\%] = \frac{\epsilon_f^{Air} - \epsilon_f^{H_2}}{\epsilon_f^{Air}} \cdot 100\% \quad (5.1)$$

5.2.3. HYDROGEN ANALYSIS

Several specimens were removed from the test setup after the controlled hold step and the gauge section of homogeneous strain was cut out. The gauge was then transferred to a Bruker G8 Galileo ONH thermal desorption analyser equipped with the IR07 furnace for accurate temperature ramping. Each strain condition was measured three times at heating rates of 1, 0.66 and 0.33 K/s from room temperature up to 600 °C. The amount of absorbed hydrogen were measured and the peak temperatures were

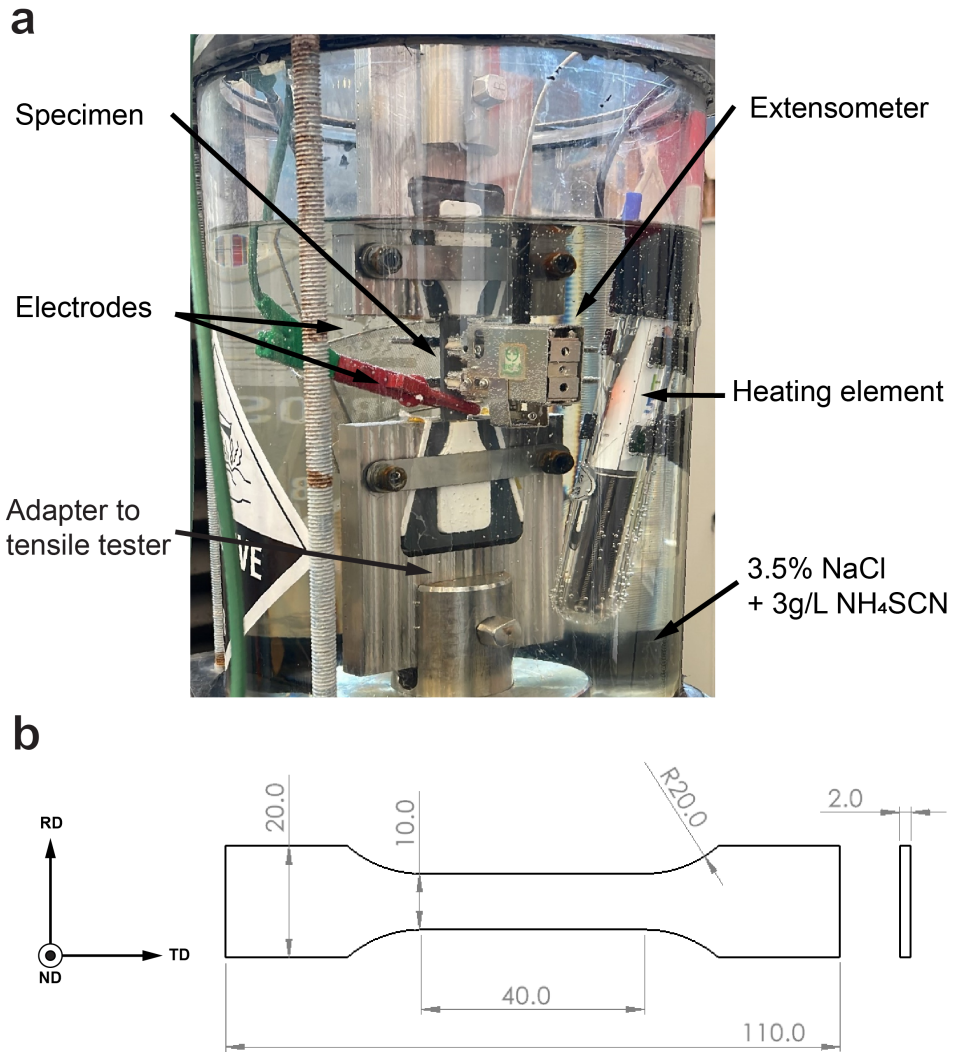


Figure 5.2.: a) Overview of the in-situ hydrogen setup used for tensile testing and b) the dimensions (in mm) of the tensile specimen geometry used in this study. Adapted from [134].

analysed using the simplified Kissinger equation [129], which is shown in Equation 5.2. This equation allows for determination of activation energies relating to individual peaks in the hydrogen desorption spectrum.

$$\frac{d \ln(\phi / T_{max}^2)}{d(1/T_{max})} = -\frac{E_A}{R} \quad (5.2)$$

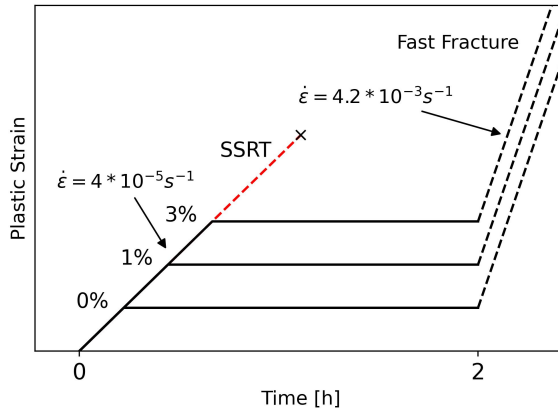


Figure 5.3.: Overview of the test procedure The entire test is performed during hydrogen charging, axes are not to scale.

In this equation T_{max} is the peak temperature of the H desorption peak in K, ϕ the heating rate in K/s, R the universal gas constant 8.3415 J/molK and E_A the activation energy for hydrogen desorption of the specific hydrogen trap in kJ/mol. E_A can be derived from the slope by fitting $\ln(\phi/T_{max}^2)$ to $(1/T_{max})$.

5.2.4. CHARACTERISATION

Several characterisation methods were used to study the material in its undeformed and deformed states. Fractured specimens were prepared by cleaning in an ultrasonic bath with isopropanol. For Electron Backscattering Diffraction (EBSD) images, the fracture surfaces were sectioned and embedded in a thermoplastic resin. The surface was polished up to a colloidal silica OPS finish of 0.04 μm and the samples were cleaned in the ultrasonic bath afterwards. Both Scanning Electron Microscopy (SEM) and EBSD were performed on a Thermo Fisher Scientific™ Helios™ G4 PFIB UXe SEM. Fractographic images were taken at an acceleration voltage of 20 kV and a probe current of 0.4 nA. EBSD maps were obtained at a voltage of 15 kV and current of 6.4 nA instead to increase signal quality. The step size for all EBSD images shown in this work was 70 nm in order to obtain several indexed points even for the smallest grains and a low cut-off angle of 5° was used for grain boundary identification. Selected EBSD specimens were used for X-ray Diffraction (XRD) measurements to obtain the dislocation density in all stages of deformation. The measurements were performed on a Bruker D8 Advance diffractometer using Co K α radiation, with a 2θ range of 40° - 135°, a step size of 0.02 ° and a counting time per step of 2 seconds. The modified Williamson-Hall method as used by Verma et al. was utilised to calculate the dislocation densities [151]. The smallest and largest crystallite sizes found were 75 nm and 260 nm for the necked area of a fractured SSRT specimen and an elastically deformed specimen, respectively. This means that the pixel size for the EBSD measurements was smaller than the crystallite size in all specimens.

To negate the influence of the pixel size on the Kernel Average Misorientation (KAM) measurements, the kernel included the 1st and 2nd nearest neighbour points, resulting in a kernel diameter of 350 nm which is larger than the largest crystallite. All points in a kernel were used for the KAM calculation. The crystallite sizes were exclusively used as a guideline to choose the KAM kernel size. All other discussion of grain sizes uses the grain sizes as measured from EBSD.

5.3. RESULTS

5.3.1. HYDROGEN ABSORPTION

Table 5.3 contains an overview of the amount of absorbed hydrogen in each specimen after the charging and holding time of 2 hours. The amount of H absorbed by the unstrained benchmark specimens was measured in our previous research, discussed in Chapter 4, under identical charging conditions and was found to be 2.18 ± 0.28 wppm [134]. It should be noted that the incoherent precipitates that are also present in the steel trap hydrogen in stronger sites that show desorption peaks at higher temperatures. These were, however, shown not to be further charged by the method of charging in this work and they do not influence the mechanical behaviour of the steel [21, 134]. Higher temperatures were therefore left out of the TDS measurements for this work. The hydrogen content found for the 0% pre-strained specimens is 2.36 ± 0.17 wppm, which is within spread of that of the benchmarks. In contrast, the absorbed hydrogen content rises significantly upon the application of plastic pre-strain. The 1% and 3% plastically pre-strained specimens were found to absorb 3.00 ± 0.11 and 3.69 ± 0.26 wppm, respectively. The differences in hydrogen absorption between elastic and plastic pre-strain shows the relative importance of dislocations as hydrogen trapping sites. The desorption curves for all specimens have been shown in Figure 5.4. Skewed Gaussian peaks were fit to the measurement data represented in the figure, of which the maximum peak temperatures were used to calculate the activation energy of desorbed hydrogen in the peak. Table 5.3 shows them to be 21.0, 23.1 and 25.2 kJ/mol for increasing plastic pre-strain. The activation energy increases with plastic strain, but the extra hydrogen that is absorbed is stored in the same type of trap, namely the dislocation. Since trap occupancy in dislocations increases significantly, the increase in calculated activation energy can be understood to be an effect of re-trapping of hydrogen by dislocations before final desorption occurs that lowers the effective diffusivity of hydrogen throughout the steel [148, 152]. The actual activation energy of a dislocation, however, would not change.

Observing the mechanical behaviour in Figure 5.5, it is evident that the increase in hydrogen uptake with increasing plastic pre-strain is not directly related to earlier final fracture. A trend is visible in the tensile curves, showing that, regardless of the amount of pre-strain, most tensile samples are not significantly more brittle than the uncharged benchmarks. Some individual samples are embrittled, but the degree of embrittlement is similar between specimens with different amounts of pre-strain or hydrogen uptake. The average HEI for the specimens was calculated to be 9.2, 6.6 and 9.5% for the 0, 1 and 3% pre-strained specimens, respectively. On the other hand,

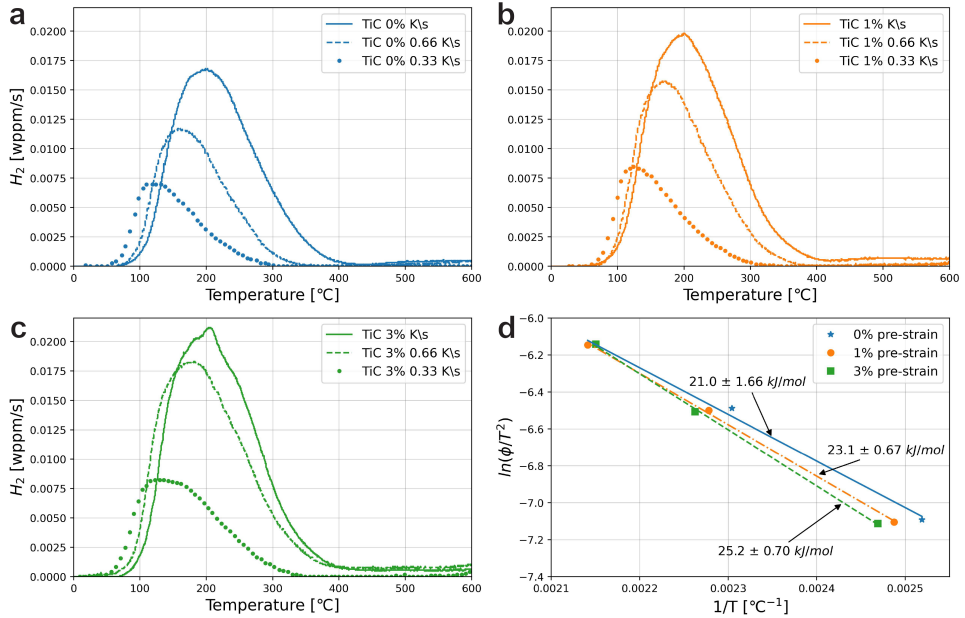


Figure 5.4.: Hydrogen desorption curves of a) 0%, b) 1% and c) 3% plastic strain as well as d) the Kissinger plot of the activation energies E_A for all pre-strains.

Table 5.3.: Hydrogen absorption and mechanical behaviour properties of all tested conditions. Errors are standard deviations.

	H content [wppm]	E_A [kJ/mol]	Fracture strain [%]	HEI [%]
Benchmark	2.18 ± 0.28	-	14.2 ± 0.47	-
0% Pre-strain	2.36 ± 0.17	21.0 ± 1.66	12.9 ± 2.08	9.2 ± 18.35
1% Pre-strain	3.00 ± 0.11	23.1 ± 0.67	13.2 ± 1.36	6.6 ± 13.13
3% Pre-strain	3.69 ± 0.26	25.2 ± 0.70	12.8 ± 2.01	9.5 ± 17.83
SSRT	3.48	-	5.7 ± 0.29	59.8 ± 4.02

the SSRT specimens are consistently embrittled and fail around a strain of 5% even though they have been exposed to the charging environment for approximately 1 hour, which is their time to fracture. A fractured SSRT specimen was measured in the TDS shortly after fracture and was found to have a hydrogen content of 3.48 wppm, which is within spread of samples strained to only 3% after two hours of charging. It therefore seems to have absorbed hydrogen more quickly. However, the strain after fracture is not homogeneous, so hydrogen is most likely segregated to regions of high ductility. Therefore no conclusive quantitative statements can be made about the hydrogen concentration in the fracture specimen. The SSRT specimens are severely

embrittled, and have a HEI of 60%.

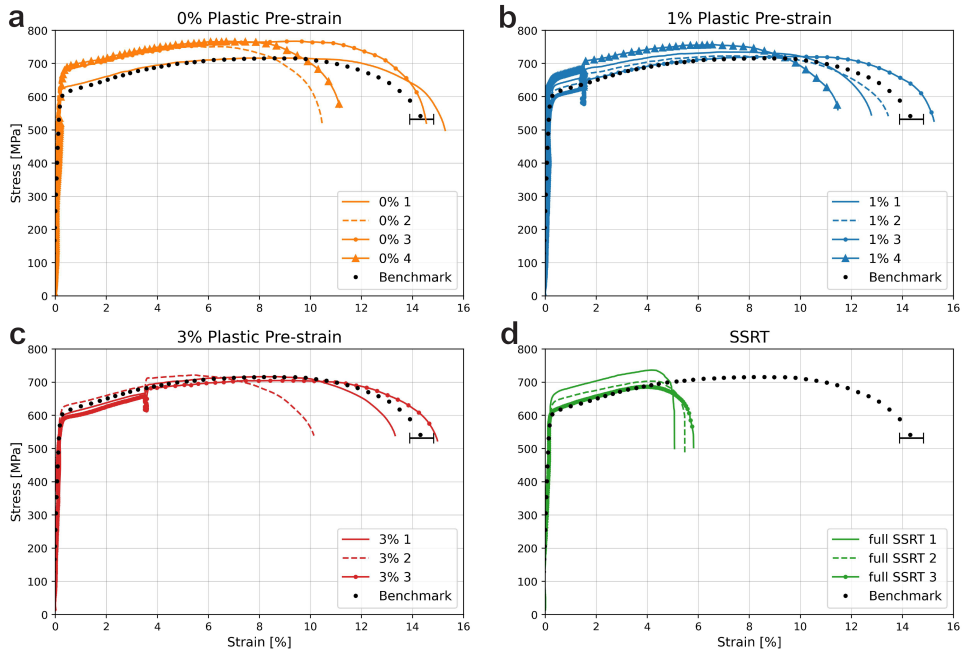


Figure 5.5.: Strain curves for a) 0%, b) 1% and c) 3% pre-strain, and d) full SSRT curves. All tests except for benchmarks were performed during hydrogen charging. The error bar for the benchmark tests indicates the standard deviation of final fracture strain.

5.3.2. MEASUREMENTS OF PLASTIC DEFORMATION

Other than hydrogen content, for specimens at pre-strains of 0, 1 and 3% the dislocation densities were determined through XRD and the KAM through EBSD. The necking area of an SSRT specimen was also characterised for both to provide data for a microstructure near fracture in hydrogen. The results are shown in Table 5.4 and an overview of the KAM measurements is shown in Figure 5.6. Although KAM measurements only include information on the density of Geometrically Necessary Dislocations (GNDs), and measurements from XRD also include Statistically Stored Dislocations (SSDs), the relative number of GNDs has been shown to constitute the majority of all dislocations up to the point of necking under tensile loading conditions [153]. The two techniques can therefore be used comparatively in this strain regime. Since the dislocation density is never zero, the specimen strained below the yield point already has a dislocation density of $1.8 \pm 0.3 \cdot 10^{14} \text{m}^{-2}$, which corresponds to an average KAM of 0.6° . Both values increase with strain, where the largest relative increase is found between 0 and 1% plastic strain. The maximum is found in the necking area where the dislocation density is $4.4 \pm 0.7 \cdot 10^{14} \text{m}^{-2}$ and the average

KAM is 1.4° . It should be noted that the XRD is a macroscopic characterisation technique with an analysed surface area of roughly 1 cm^2 . Since the necked region has strain heterogeneities, the measurement for the SSRT specimen therefore has a larger error than the other dislocation densities. The KAM measurement is much more localised and was therefore taken in an area close to the fracture surface. This as such gives a more localised indication of the deformation near the fracture surface of the specimen.

Table 5.4.: Dislocation density obtained from XRD, and Kernel Average Misorientation obtained from EBSD for specimens at 0, 1, and 3% plastic strain, as well as in the necked area of an SSRT specimen.

	Dislocation Density [$10^{14} m^{-2}$]	KAM [$^\circ$]
0% Plastic Strain	1.8 ± 0.3	0.60 ± 0.30
1% Plastic Strain	2.8 ± 0.4	1.02 ± 0.53
3% Plastic Strain	3.3 ± 0.5	1.16 ± 0.59
SSRT	4.4 ± 0.7	1.40 ± 0.62

5.4. DISCUSSION

In this work, we attempt to quantify deformation of the microstructure by plotting the dislocation density, KAM values and the hydrogen content as a function of plastic strain. Through measuring all three on specimens with known homogeneous macroscopic plastic strains for 0, 1 and 3%, a relation between them is established and the effect of dislocations can be isolated. Figure 5.7a shows a graphical overview of the dislocation density, the KAM and the hydrogen content of the specimens as a function of the plastic strain. The amount of plastic strain for the SSRT specimen is denoted as 'Neck', for which the location on the axis was determined as 4.8% by fitting it to the KAM measurements obtained for that area. Upon plastic straining, the amount of hydrogen traps increases in the form of newly generated dislocations. Figure 5.7b shows the hydrogen content as a function of the dislocation density to illustrate this effect. The data closely follows a linear regression, which has been extrapolated to both the average dislocation density in the neck region as well as a theoretical density of 0 for a dislocation-free polycrystal. The hydrogen content in the most deformed portion of the neck can be estimated to be 4.55 wppm if it were charged to saturation, but this was likely not the case. It is more interesting to consider the amount of absorbed hydrogen at a theoretical 0 dislocation density by extrapolating the curve to lower strain values. Although the actual dislocation density can never be zero due to entropic effect, the number gives an indication of the amount of hydrogen that would be trapped in sites that are not dislocations. Examples of these sites could be lattice positions and grain boundaries, but also hydrogen that is stored in and on the interface of TiC nano-precipitates. From the linear extrapolation, this amount is calculated to be 0.72 wppm. This means that 1.64 wppm of hydrogen is stored in dislocations even in the 0% pre-strained specimens,

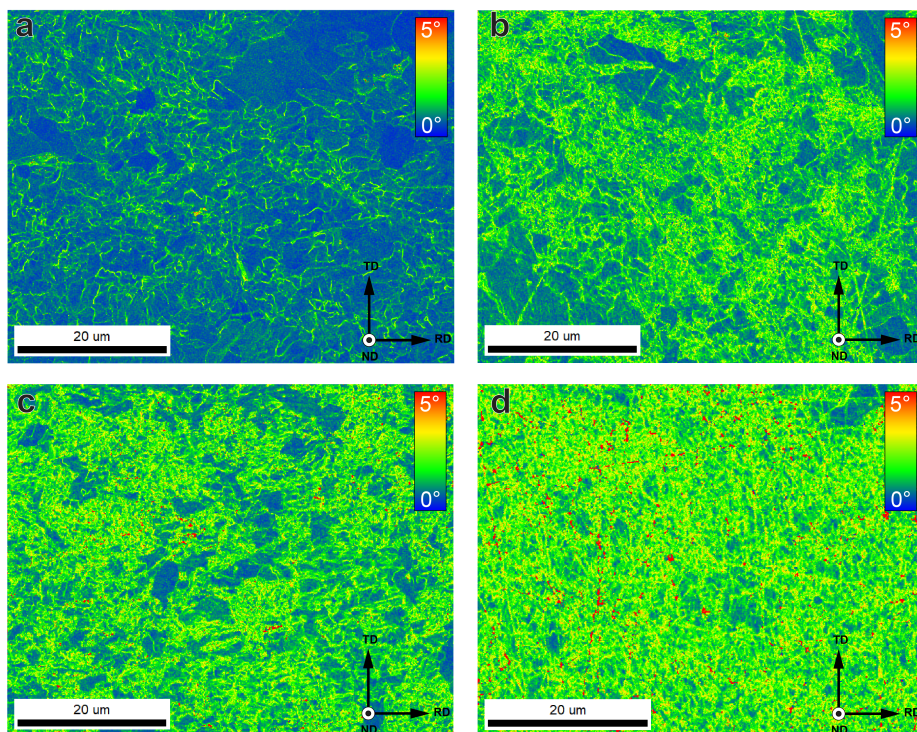


Figure 5.6.: Kernel Average Misorientation maps of Specimens strained at a) 0%, b) 1%, c) 3% plastic strain and d) in the necked area of a fractured SSRT sample.

which increases to 2.97 wppm for 3%. Even if precipitate traps would be the only other traps than dislocations, the hydrogen trapped in them would thus be less than a third of the amount of hydrogen that was absorbed in the 0% plastically strained specimen. The added hydrogen trapping capacity of the precipitates in this steel is therefore only of minor influence on the total capacity of the steel, especially when plastic deformation occurs. Furthermore, the traps that they present are considered diffusible with activation energies of less than 50 kJ/mol [21]. This means that while the TiC precipitates provide additional strength to the microstructure, their benefit to HE resistance could be limited. Perhaps their largest benefit is in retarding hydrogen diffusion throughout the microstructure, but it should be studied whether this makes up for the extra absorption of hydrogen.

An important finding is that the increased hydrogen concentration caused by the increase in dislocation density from 2.36 ± 0.17 wppm to 3.69 ± 0.26 wppm does not increase the amount of embrittlement observed in the mechanical tests. Embrittlement was instead much larger in the SSRT specimens, although the hydrogen charging time for these specimens was the shortest. This means that, first of all, hydrogen charging to full saturation is not a prerequisite for HE. It also means that

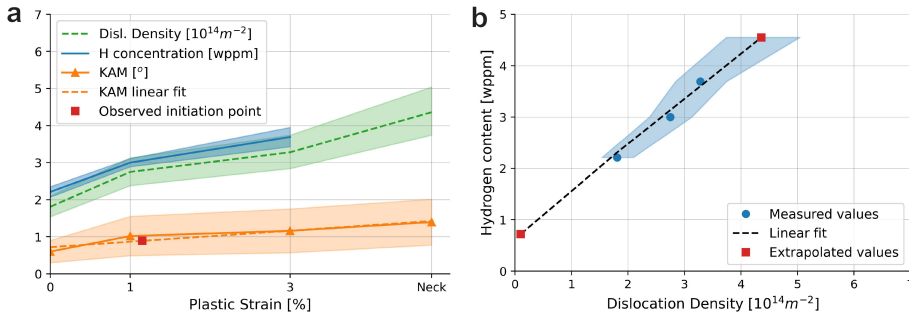


Figure 5.7.: a) The hydrogen content, dislocation density and Kernel Average Misorientation (KAM) as a function of the amount of Plastic Strain. Data for the 'Neck' point on the x axis was obtained on a necked area of an SSRT specimen. The average KAM value underneath brittle crack surfaces was indicated as the 'Observed initiation point'. b) the H content as a function of the Dislocation Density with extrapolated data for the ideal case of no dislocations, as well as a H content in the necked area of an SSRT specimen.

the steel can accommodate a higher hydrogen content than what is required to cause fracture, given that the plastic deformation is kept below a certain limit, in this case approximately 5%. This raises the question, however, what happens at this level of deformation to cause sudden fracture of the specimen. The fracture surfaces of post-mortem specimens can indicate the progression of a crack in the specimen. Figures 5.8a and 5.8b show the fracture surfaces of the 3% 2 specimen and an SSRT specimen, respectively. As is also frequently observed in literature, brittle fracture initiation zones were discovered around the edges that were exposed to the hydrogen environment [43, 82, 141, 142, 146]. These zones correspond to the macroscopically brittle quasi-cleavage (QC) fracture mode, and are indicated in red. The length of the brittle crack initiation zone corresponds to the width of the QC fracture zone on the fracture surface. This was measured to be in between 30 and 50 μm for the pre-strained specimens, and it was found to be independent of the degree of plastic pre-straining. The SSRT specimens on the other hand, show a brittle zone of up to 500 μm , as can be seen in Figure 5.8b. The fracture surface outside the brittle zones shows micro-void coalescence (MVC) type fracture that forms when the crack growth speed is too high to allow for continuous hydrogen diffusion to the crack tip. This can therefore only be formed during the fast fracture stage of the test. Since brittle fracture initiation occurs even in the 3% specimens, this is not the cause of failure that happens in the SSRT specimens. A higher magnification overview of the transition zone from QC to MVC fracture in a 3% specimen is given in Figure 5.9.

To find out at what point brittle initiation occurs, EBSD measurements were performed on cross-sections of selected specimens post-mortem. KAM maps of the sub-fracture surface microstructure beneath the brittle initiation zone were obtained.

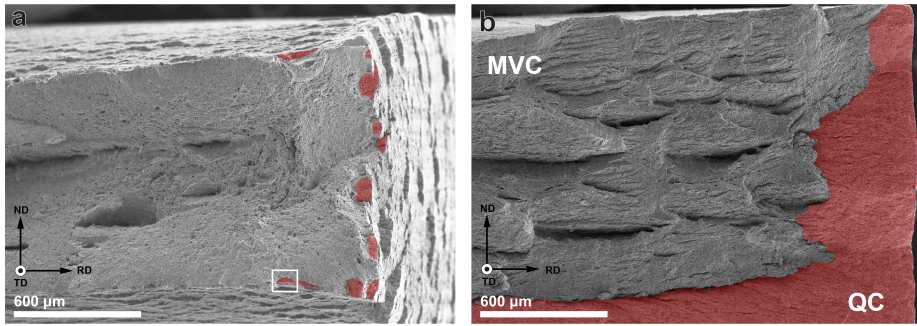


Figure 5.8.: Fractographic overviews of specimens a) 3% and b) SSRT where brittle Quasi-Cleavage (QC) crack initiated zones are indicated in red and Microvoid Coalescence (MVC) regions remain unmarked.

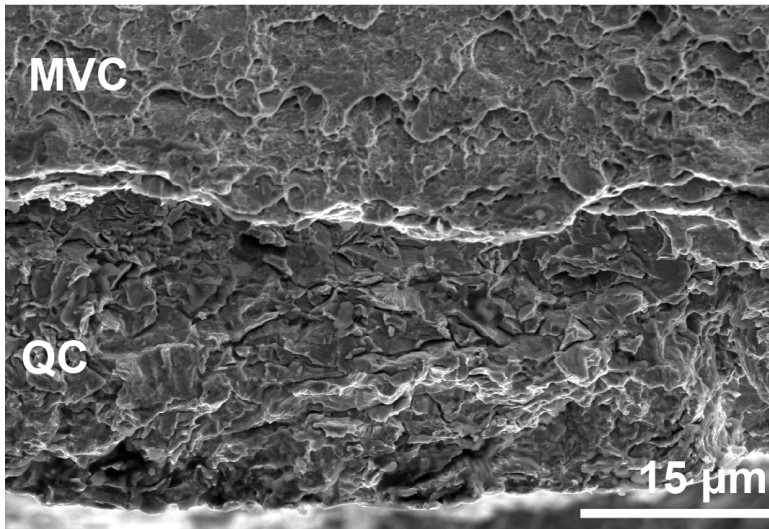


Figure 5.9.: Fracture surfaces showing the transition zone from Quasi-Cleavage (QC) to Microvoid Coalescence (MVC) fracture in a 3% specimen, taken from the area indicated in Figure 5.8a.

Figures 5.10a and 5.10b show two examples of these KAM maps. Figure 5.10b corresponds to the same sample shown in Figure 5.8b, while 5.10a was taken from a 0% specimen that shows clear crack initiation on one side, providing a good study case to observe the amount of deformation required for brittle crack initiation. The average KAM values calculated beneath the crack surface is $0.89 \pm 0.47^\circ$. This point is indicated in Figure 5.7a to belong to a plastic deformation just over 1% if fit to the regression. This value itself, however, is markedly below that of 1.02° obtained for a homogeneous plastic strain of 1%. This indicates that first crack initiation in the tests

takes place early on during the deformation, when a homogeneous strain of 1% is reached. Evidently these cracks do not propagate in the 3% specimens, but do in the SSRT specimens where they grow large enough to cause macroscopic fracture.

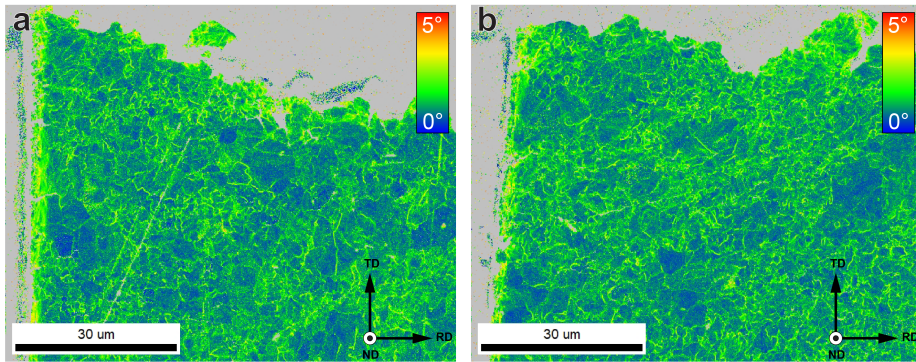


Figure 5.10.: Post-mortem Kernel Average Misorientation maps of areas below a brittle initiation point on the fracture surface of a) 0% and b) SSRT specimens. Grey pixels were not included in the KAM measurement.

This finding is supported by Figures 5.11a and 5.11b, which show the sides of the 3% 2 specimen and a SSRT specimen, respectively. The 3% pre-strained specimen shows a high amount secondary cracks on the side surface, with significant crack mouth opening. In the SSRT specimen, on the other hand, the fracture is entirely localised to a single crack. Some secondary cracks can be observed, but they have not been opened. The opening of the secondary cracks in the 3% specimen is shown at a higher magnification in Figure 5.11c. Here the crack clearly displays a brittle fracture initiation zone that transitions in to a region of ductile tearing. This is supported by an IPF map obtained from EBSD shown in Figure 5.11d which shows the contrast between the relatively equiaxed grains beneath the brittle surface and the heavily deformed grains in the plastic region. These findings indicates that brittle cracks initiate at several locations during either the straining or hold time of the 3% specimen, but they arrest and are only opened during the further straining in the fast fracture stage of the test. Here the strain rate is high enough that no more hydrogen is absorbed, diffusion towards the moving crack tip is too slow and therefore the material retains its ductility. The SSRT specimens, on the other hand, were continuously strained at a low strain rate while being charged with hydrogen. This induces continuous crack growth where the crack tip can be supplied with hydrogen from the electrolyte, which causes brittle fracture even if the steel is not saturated with hydrogen. The extent of HE is therefore more correlated to the opening of the crack during hydrogen charging than the duration of charging itself and the resulting saturated hydrogen content.

The reason that the cracks initiated around 1 % deformation do not propagate during the hold phase is unknown. A brittle crack that has initiated could be expected

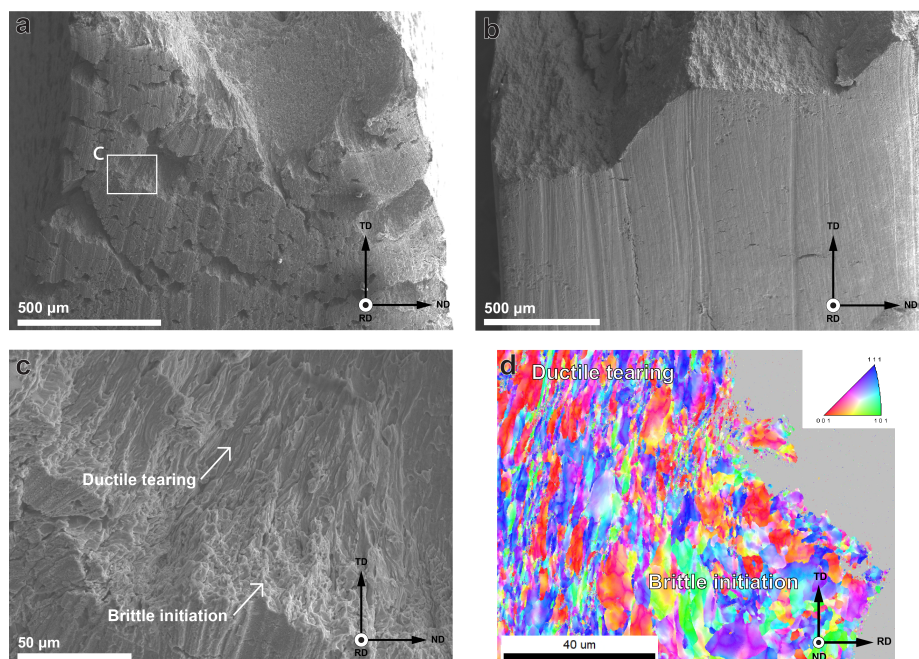


Figure 5.11.: Fractographic images of 45° tilted specimens a) 3% and b) SSRT. c) shows a zoomed in section of a crack in (a) to highlight the transition from brittle to ductile fracture. An Inverted Pole Figure (IPF) map of the cross-section of a similar transition is shown in d) where the start of plastic deformation can be observed.

to grow under a constant opening in a hydrogen environment since new hydrogen is absorbed and the stress concentration presented by the crack tip attracts hydrogen from the nearby bulk material. A possible reason for crack arrest could be a small force drop during the hold phase of the tests as a result of relaxation of the specimen and grips. This drop in force can be seen in Figure 5.5 to occur for specimens strained above the yield point and could cause crack tip closure, depending on the degree of plastic deformation near the crack tip. The plastic deformation would be microscopic, however, given that QC fracture surface is not formed from large-scale plastic deformation [71].

5.5. CONCLUSIONS

This research shows that an increased internal hydrogen concentration does not necessarily increase HE. Instead, it is largely governed by the presence of hydrogen in the environment during crack initiation and propagation. The steel can absorb a significant amount of hydrogen without showing signs of embrittlement, provided it is

not plastically deformed above a certain threshold. By varying the amount of plastic deformation, the trapping capacity of dislocations could be isolated from that of other features like precipitates, showing that the effect of dislocations on hydrogen trapping is much more significant than that of nano-precipitates. The following conclusions can be drawn from this work:

- Increasing load within the elastic region has little impact on the absorbed hydrogen content, which was 2.36 ± 0.17 wppm in the 0% pre-strained condition versus 2.18 ± 0.28 wppm in an undeformed specimen.
- Even small amounts of plastic deformation notably increase the H absorption in the steel from 3.00 ± 0.11 wppm for 1% up to 3.69 ± 0.26 wppm for 3% plastic strain.
- Up to 2.97 wppm of hydrogen is stored in dislocations, with only 0.72 wppm of hydrogen stored in other traps such as lattice sites, grain boundaries and precipitates.
- Although beneficial for precipitation hardening mechanisms, precipitates do not play a dominant role in the hydrogen trapping capacity of ductile steels since significantly more hydrogen is stored in dislocations.
- Increased H absorption does not immediately lead to higher hydrogen embrittlement. All three levels of pre-straining resulted in 6 to 10% of ductility loss.
- Small brittle cracks begin to form around 1% global plastic strain, initiating on the outside surface of the steel that is in contact with the electrolyte and showing a Quasi-Cleavage fracture surface. These cracks only propagate in a brittle manner during continued slow strain rate tests. In such cases, the loss in ductility is 60%.

6

HYDROGEN EMBRITTLEMENT IN DUAL PHASE STEELS

Previous chapters discussed the influence of carbide precipitates on reducing the hydrogen embrittlement in ferritic steels. Steels that are currently in use in the automotive industry, however, combine ferrite with different harder phases like martensite or bainite. This chapter adds to the overall discussion of HE in steels by dealing with the hydrogen embrittlement (HE) behaviour of Dual Phase steels with varying martensite content. Steels with martensite contents of 25 ± 5 , 50 ± 4 and $78 \pm 7\%$ were realised by intercritically annealing an as-received DP steel. These steels were charged with hydrogen and consequently subjected to an in-situ slow strain rate tensile test to characterise the embrittlement. It was found that the 50% martensitic steel showed most ductility in air, but the higher embrittlement of $86 \pm 10\%$. The extent of embrittlement does not increase further after martensite forms a continuous network in the microstructure. The presence of martensite on the surface is linked to the formation of brittle crack initiation sites in DP steels, even at low hydrogen contents. Furthermore it was found that the anisotropic banded structure in the annealed steels promotes brittle crack propagation along the direction of banding, which originates from rolling process. This research shows that anisotropic martensite distributions as well as surface martensite should be avoided when developing DP steels to maximise HE resistance.

This chapter is in preparation for journal submission.

6.1. INTRODUCTION

Previous chapters have dealt with the in-depth characterisation of the Hydrogen Embrittlement (HE) behaviour of ferritic nano-precipitate steels for use in the automotive industry. These steels provided a simple single phase ferritic system that allowed for separate study of the effect of precipitates. However, the approach of using single phase ferritic steel in the car body is a recent development and is not used in practice to the extent that more developed Advanced High Strength Steels (AHSS) are [10]. They contain phases other than ferrite, which also play a large role in hydrogen embrittlement susceptibility since they interact with hydrogen differently. Therefore there is benefit in also studying the HE behaviour of currently widely implemented AHSS to elucidate the influence of their microstructural features in HE.

The most widely used types of AHSS with a ferritic matrix are the Dual Phase (DP) steels. DP steels combine the ductility of the ferritic phase with the strength of an interdispersed martensitic phase to obtain a low initial yield point, but a high strength with high initial strain hardening [154]. This results in good properties for formability and energy absorption [7]. DP steels make up around a third of the body-in-white of a modern car chassis [10], and are used in various components such as panels, pillars and shock reinforcement parts [11]. However, DP steels have been found to be susceptible to HE like other AHSS [28, 155–157]. Its susceptibility is related to the martensitic fraction of which both the interphase boundary with ferrite as well as the grains itself can be hydrogen trap sites [158]. Decades of experience with DP steels have created a good understanding on how to alter the martensitic fraction and grain sizes, which has led to multiple studies characterising their effects on the HE of DP steels. A comprehensive understanding, however, has still not completely been achieved [7, 14].

Different literature sources suggest a HE behaviour that is divided into three regimes, based on martensite content [28, 29]. At martensite below 10%, no HE is found, since the majority of the microstructure is ferritic and martensite islands are therefore spaced apart. The ferrite/martensite (F/M) interphase boundary is found to be the main hydrogen trap for this microstructure [28, 139, 159]. As the martensite content increases, martensite grains grow, the interphase area increases, and more H is stored. When martensite grains grow large enough to connect to each other, a continuous martensite network is formed within the ferrite matrix. Wang et al. reason that at such martensite concentrations, 68.3% in their study, the F/M interphase area decreases and the hydrogen is stored inside the martensite instead [28]. HE is found to no longer increase at higher martensite fractions from this point by Davies, although Wang et al. find that it does increase as the amount of absorbed hydrogen still increases and the diffusivity of hydrogen decreases.

The fracture in DP steels charged with hydrogen is found to initiate either on the F/M interphase, or within martensite grains. DP grades with a high ferrite fraction can accommodate more strain, but develop significant strain partitioning at the interphase boundary between the ductile ferrite and the hard martensite [28]. A local high plastic

strain increases the capacity for hydrogen absorption [139, 146, 147], finally leading to decohesion of the interphase. Ferrite between martensite islands acts as a crack propagation barrier, but it decreases in effectiveness as martensite grains grow and the ferrite in between them decreases in thickness [28]. Moreover, the ferrite reduces in capacity to act as a barrier when hydrogen is introduced into the microstructure, as shown by Koyama et al. [65]. Higher martensite fractions give the DP steel a higher strength, but sacrifice in strain since the martensitic network supports the applied stress and does not allow the ferrite to deform. Furthermore, cracks can propagate purely through the martensite at this point, and the crack growth inhibiting role of the ferrite disappears. The exact point at which this happens, though, seems to vary between microstructures. Davies reports it to be around 30% martensite [29], whereas Wang et al. report it to be 68.3%.

The effects of microstructural morphology were reported by Rodoni et al, who observed crack initiation on the F/M interphase [160]. Cracks propagated through bands of martensite within a DP matrix, perpendicular to the rolling direction. The cracks were arrested upon meeting a ferrite grain. This anisotropy is often found in rolled sheets, and could provide better HE resistance in a particular direction. Sun et al, for example, engineered a microscale lamellar structure of ferrite and martensite grains perpendicular to the tensile direction, which improved HE resistance compared to an untreated material [161]. Microstructural anisotropy should therefore be considered when investigating fracture behaviour of a DP steel.

There are two points of ongoing discussion in the literature that require further research. Firstly, opposing views have been published on whether HE in DP steels increases past the point of formation of a connected martensitic matrix. This means that the effects of anisotropy should be considered, since rolling texture influences the formation of martensite bands in the rolling direction. This chapter addressed these issues by discussing results regarding DP steels steel in a hot-rolled sheet. It elucidates on the role of the anisotropic martensite configuration in hydrogen embrittlement, as well as fracture initiation and propagation within the microstructure.

6.2. MATERIALS AND METHODS

The as-received DP steel studied in this work is a 1 mm thick commercial grade DP1000 steel, of which the composition is shown in Table 6.1. The microstructure, shown in Figure 6.1, is made up of a connected network of martensite with refined $1.7 \pm 0.7 \mu\text{m}$ ferrite grains in between. The martensite content in the as-received alloy is approximately 68% as determined by using the ImageJ analysis software on Figure 6.1. Heat treatment experiments were performed to vary the martensitic content of the DP steel in order to study the effect of martensite fraction and structure on the HE behaviour.

Table 6.1.: Alloy content of the as-received DP steel used in this research in wt%.

Fe	C	Mn	Cr	Si	Al	Nb	Ti	P	S
96.98	0.14	2.15	0.54	0.13	0.02	0.02	0.01	0.01	0.01

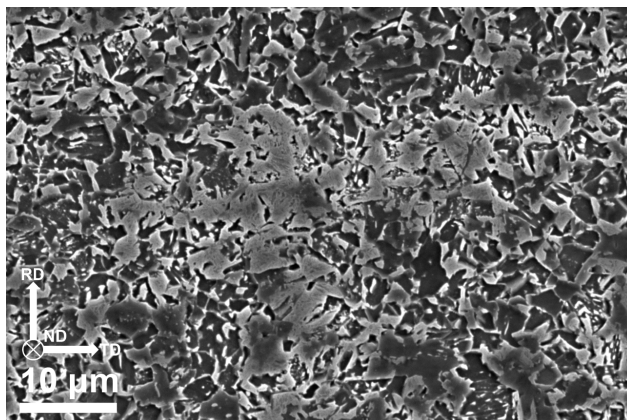


Figure 6.1.: The as-received microstructure. Martensite is shown as the lighter phase, and ferrite as the darker.

6.2.1. HEAT TREATMENTS AND CHARACTERISATION

The focus of the work discussed in this chapter is to tailor DP steels with different martensite fractions in order to assess their HE susceptibility. Heat treatments were performed in a Gleeble 3800-GTC thermomechanical simulator, which consisted of a heating step to 900 °C with 10 °C/s per second, holding there for 3 minutes, cooling down to three different intercritical annealing temperatures with 1 °C/s, holding for 10 minutes and finally air quenching to room temperature. Intercritical annealing temperatures of 590, 610, 630, 650 and 670 °C were chosen for trial heat treatments on a Bähr FIL805A/D quenching and deformation dilatometer, based on the Ac_1 and Ac_3 temperatures that were determined as 686 °C and 571 °C. Three final heat treatments temperatures of 590, 630 and 670 °C were then chosen for Gleeble simulation.

The martensite fraction was determined through both optical (OM) and electron microscopy (SEM), as well as electron backscattering diffraction (EBSD). For all these techniques, samples were embedded in thermoset resin, sanded and polished to a 1 µm finish, and finally etched in a 5% nital solution for 8 seconds. Instead of etching, EBSD specimens were further polished to a 0.04 µm colloidal silica OPS finish. Optical microscopy images were taken on a Keyence VHX-7000 digital microscope which includes automated measurement of area fractions based on brightness. Electron Microscopy images were taken on a JEOL JST-IT100 dekstop SEM. In this case images were exported and analysed externally using the ImageJ software. EBSD was performed inside a Thermo-Fisher Helios G4 PFIB UXe HRSEM equipped with a

EDAX Technology APED camera. Measurements were performed at an acceleration voltage of 15 kV, with a probe current of 6.4 nA and a step size of 100 nm. The ferritic and martensitic phases were distinguished by color in OM, by brightness in SEM and by image quality in EBSD. Three different areas were measured for each heat treatment condition for all techniques. Martensite fractions were found to correspond well between techniques, and the average of the techniques will be used throughout this chapter. All fractographic images throughout this chapter were also obtained on the JEOL JST-IT100 desktop SEM. Vickers Hardness measurements with a force of 1 kg were performed on a Struers Durascan automatic hardness tester.

6.2.2. HYDROGEN CHARGING AND MECHANICAL TESTING

Specimens heat treated in the Gleeble were electron discharge machined (EDM) to a double neck-geometry that is depicted in Figure 6.2, where TD is both the transverse rolling direction as well as the tensile direction. Double necking is necessary because the edges of a single-necked specimen are not heat treated homogeneously in the Gleeble, and would have a different microstructure from the centerline. Moreover, it localises fracture to the zone that was treated in the Gleeble and that has the desired microstructure. The specimens were subjected to slow strain rate tensile (SSRT) tests in a ZwickRoell Z100 universal tensile tester fitted with the same setup that is discussed in Chapters 4 and 5. The bath is filled with a solution of 3.5% NaCl + 3g/L ammonium thiocyanate (NH_4SCN), which is used to charge the specimen at a current density of 1 mA/cm^2 . Each specimen is pre-charged for 2 hours, before being strained until fracture at a strain rate of $3.125 \cdot 10^{-5}/\text{s}$.

Benchmark tests to obtain the mechanical properties of the DP steels without hydrogen were performed ex-situ on specimens containing a single gauge section similar to the outer dimensions of the sample shown in Figure 6.2. This was done to obtain more accurate data for the whole stress-strain curve of the non-hydrogenated specimens on a longer specimen gauge.

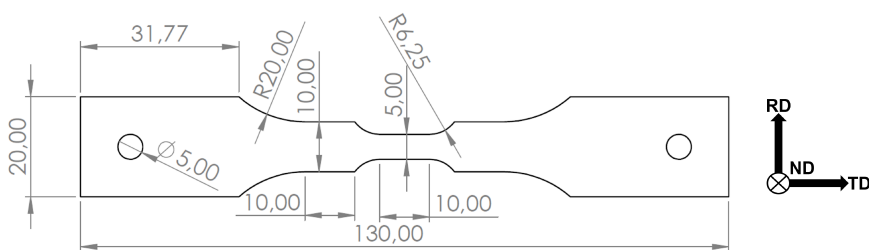


Figure 6.2.: Sample geometry after Gleeble testing. The axis system is relative to the rolling direction (RD), Transverse direction (TD) and normal direction (ND) of the hot-rolled sheet. All dimensions are in mm.

Hydrogen contents were measured on a Bruker Galileo G8 with added IR07 infrared furnace. Specimens taken from the second neck of the in-situ tested samples were measured in the impulse furnace of the G8. This is a melt extraction measurement performed at approximately 1700 °C where all hydrogen trapped in the specimen is released, measured over time and integrated into a total hydrogen content. This means that there is no distinction between diffusible and trapped hydrogen in the latter measurements, but since the amount of trapped hydrogen in DP steels has been shown to be negligible, they can be both qualitatively and quantitatively compared [40].

6.3. RESULTS AND DISCUSSION

6.3.1. CREATION OF MICROSTRUCTURES

Initial heat treatments to vary the martensite content in the DP steel were conducted in the dilatometer. The martensite content was measured through OM, SEM and EBSD methods, of which the results are shown in Figure 6.3. It is immediately visible that there is an increasing trend in martensite content with increasing annealing temperature from a minimum of 25% at 590 °C to a maximum of 78% at 670 °C. The average martensite content calculated from each technique are given in Table 6.2. In order to limit control parameters while retaining sufficiently distinct martensite contents, the heat treatments at 590, 630 and 670 °C were repeated on tensile samples in the Gleeble. Overviews of the resulting microstructures obtained from SEM are displayed in Figure 6.4. The martensite islands in the 590 °C specimen exist within a connected network of ferritic grains. This changes in the 630 °C specimen where all martensite grains are in contact with each other, although ferrite grains do still contact each other as well. The complete isolation of ferrite into separate islands is observed in the 670 °C specimen where martensite forms most of the microstructure. Connected martensite network formation thus forms here around 50% martensite, which is higher than the 30% that Davies reported [29], but lower than the 68% that Wang et al. found [28]. Since this is where both authors found the hydrogen embrittlement reach a maximum, it can be expected to level off after 50% in this research.

Other than the martensite content, the density of the ferrite/martensite interphase in $\mu\text{m}/\mu\text{m}^2$ or μm^{-1} could also be calculated from micrographs. It can be seen from Table 6.2 that the interphase density keeps increasing even at a martensite content of 78%, which directly opposes findings in literature. The unexpected increase in F/M interphase is a result of the change in size and shape of ferritic grains as the annealing temperature increases. Figure 6.4c shows that the ferrite grains that exist in between the martensite matrix have a very small size as well as an elongated shape, which can both contribute to a high interphase density for a relatively low ferrite content.

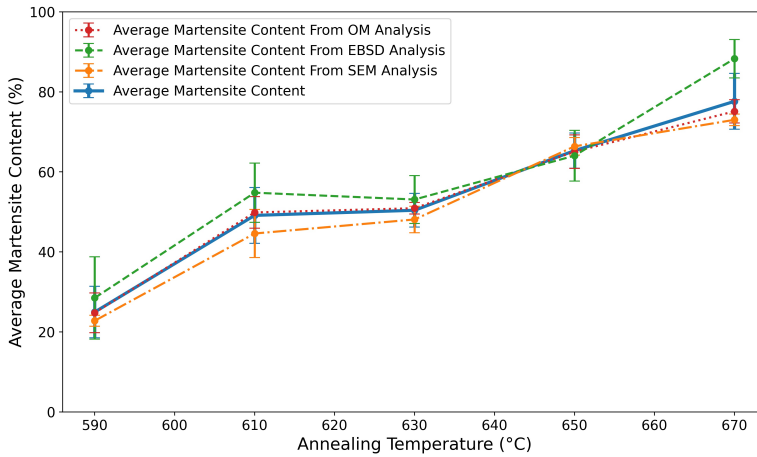


Figure 6.3.: Martensite content after intercritical heat treatments. Three separate methods, namely optical microscopy (OM), scanning electron microscopy (SEM), and electron backscatter diffraction (EBSD) were used to separately calculate the martensite content.

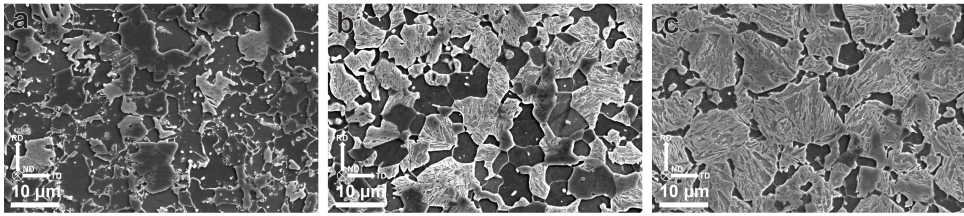


Figure 6.4.: Microstructural overviews of tensile specimens annealed at a) 590 °C, b) 630 °C, c) 670 °C during the Gleeble treatment.

Table 6.2.: Hardness, Martensite content, Martensite grain size, ferrite/martensite interphase density and hydrogen content for the investigated microstructures.

Annealing temp. [°C]	Hardness [HV1]	Martensite content [%]	Ms grain size [μm]	F/M interphase [μm ⁻¹ ·10 ⁻²]	H content [wppm]
590	238 ± 25	25 ± 5	3.9 ± 2.6	2.65 ± 0.61	1.16 ± 0.11
630	286 ± 13	50 ± 4	5.9 ± 3.2	3.12 ± 0.57	1.29 ± 0.13
670	344 ± 12	78 ± 7	7.4 ± 3.4	3.83 ± 0.44	1.58 ± 0.27

6.3.2. HYDROGEN TRAPPING

The total hydrogen concentrations are listed in Table 6.2 together with the other microstructural characteristics. They are visually represented in Figure 6.5 which shows that all three measures increase with increasing annealing temperature. In

literature, the F/M interphase is often proposed as the main microstructural feature responsible for hydrogen trapping in DP steels [28, 139, 156, 159]. These studies, however, consider the F/M interphase to decrease in density at high martensite contents. Wang et al. propose a shift in hydrogen trapping from the interphase towards the interior of the martensite grains. As can be observed in Figure 6.5, however, the F/M interphase density keeps increasing at high martensite contents in this study. This is likely caused by the refinement of the ferrite grains, which causes an increase in aspect ratio, which can be seen in Figure 6.4c. This results in an increase in F/M interphase area relative to their size. The increasing trend also matches that of the hydrogen content more closely than the increase in martensite content. This suggests that the F/M interphase remains the main contributor to hydrogen trapping even at a martensite content of 78%. In reality, however, the martensite will always trap some hydrogen, so the increased absorption will be due to both factors. In order to distinguish between their relative contributions, TDS measurements should be performed on a larger sample mass for higher accuracy to be able to distinguish between hydrogen desorbed from these separate traps.

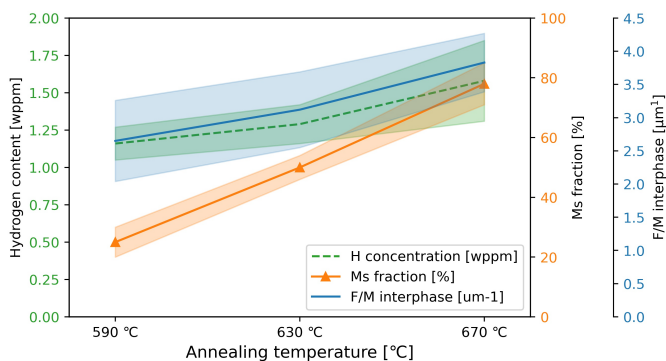


Figure 6.5.: The total hydrogen concentration in wppm, martensite content in % and ferrite/martensite interphase density in μm^{-1} for the steels annealed at all three temperatures.

6.3.3. MECHANICAL BEHAVIOUR

Representative curves of the Slow Strain Rate Tensile (SSRT) tests for all three specimen sets are shown in Figure 6.6, and an overview of all data is shown in Table 6.3. As the martensite content increases, it has more capacity to accommodate the stress and the strength of the steels increases. The 630 °C steel in particular shows beneficial properties of a relatively high strength and a considerable fracture strain of up to $12.6 \pm 0.6\%$. Unexpectedly, both strength and ductility for this steel are higher than that for the 590 °C steel, which fractures at $8.4 \pm 1.7\%$. The 670 °C has similar strain to the 590 °C steel, but at a higher strength of 1115 ± 15 MPa. As is characteristic of DP steels, plastic deformation in the ferritic phase starts early on

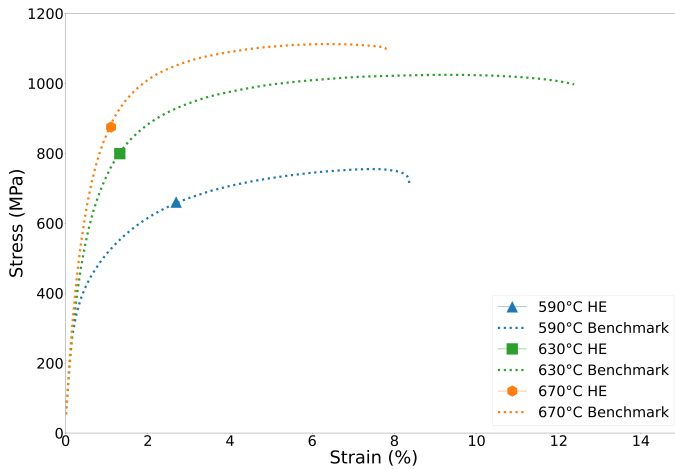


Figure 6.6.: Slow Strain Rate Tensile (SSRT) benchmark curves of the three steels tested in air, as well as the points of fracture when tested in hydrogen.

in the tensile curve which creates a gradual yield point and significant strain hardening.

Table 6.3.: Ultimate Tensile Strength (UTS) and fracture strains for all the investigated microstructures in air and charged with hydrogen, as well as the Hydrogen Embrittlement Index (HEI).

Annealing temperature [°C]	UTS [MPa]	Fracture strain [%]	UTS in H [MPa]	Fract. strain in H [%]	HEI [%]
590	756 ± 20	8.4 ± 1.7	677 ± 21	4.1 ± 0.7	51 ± 39
630	1025 ± 8	12.6 ± 0.6	798 ± 35	1.8 ± 0.2	86 ± 10
670	1115 ± 15	8.2 ± 0.8	877 ± 20	1.6 ± 0.1	80 ± 19

Behaviour in a hydrogen environment differs significantly from that in air for all tested steels. Fracture occurs during strain hardening, which results in a reduction of both strength and ductility. The 590 °C retains most of its ductility with a fracture strain of $4.1 \pm 0.7\%$ which corresponds to a HEI of $51 \pm 39\%$. The ferritic phase can accommodate more strain in a hydrogen environment than the martensitic phase. Since the ferrite still forms a connected network in the 590 °C steel, this is the reason for its relatively mild degree of embrittlement compared to the other steels. An interesting finding in these curves is that the fracture strain of the 630 °C and 670 °C steels are very similar at $1.8 \pm 0.2\%$ and $1.6 \pm 0.1\%$, respectively. The HEI factors of these steels are relatively similar at $86 \pm 10\%$ and $80 \pm 19\%$ for the 630 and 670 °C steels, respectively. While the steels therefore seem to perform comparably, it means that the 630 °C loses the higher ductility that made it perform better in the benchmark tests. The HEI stabilises from a certain martensite content, in this

case 50%, which has been explain as a result of the fact that the martensite forms a connected network that allows for easy crack propagation [28, 29]. Fracture initiation presumably happens at a similar plastic deformation for the 630 °C and 670 °C steels, and since both have martensitic networks, any difference in ferrite content or distribution becomes unimportant for the final fracture. Since the 670 °C retains a higher strength at a similar fracture strain, it is arguably the more favourable steel for hydrogen environments, although the overall performance is significantly reduced compared to its a case without hydrogen.

Even though plastic deformation seems to only occur in the 590 °C annealed specimen, it can be observed in the other specimens as well. The plastic deformation becomes visible in Kernel Average Misorientation (KAM) maps obtained 150 μm below the fracture surface of the 630 °C and 670 °C annealed specimens, as shown in Figure 6.7. KAM maps give an indication of the present of Geometrically Necessary Dislocations (GNDs) that are induced upon tensile plastic deformation to accommodate strain. Figure 6.7a shows a specimen annealed at 630 °C where it can be observed that localised areas of deformation are present around martensitic grains within the ferrite matrix, whereas larger ferrite grains remain relatively undeformed. In the 670 °C annealed specimen shown in Figure 6.7b the deformation is strongly present on the interphase boundary between the martensite and interdispersed ferrite grains, whereas it is lower in the grain interior. The localisation of plastic strain, and therefore dislocations, on and around the F/M interphase has two effects. Firstly, it masks the appearance of global plastic strain in the tensile curve, which gives the appearance that the role of plastic strain is minor. Secondly, dislocations generated during deformation cause a significantly increased hydrogen absorption as discussed in detail in Chapter 5. This means that hydrogen concentrations will also be localised to the F/M interphase boundary, which could cause accelerated fracture initiation on the interphase and propagation through the martensite grain.

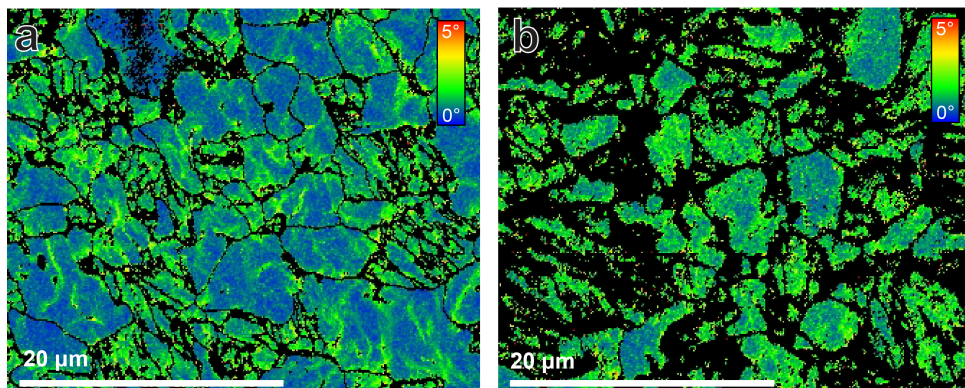


Figure 6.7.: Kernel Average Misorientation (KAM) maps made 150 μm beneath the fracture surface of specimens annealed at a) 630 °C and b) 670 °C.

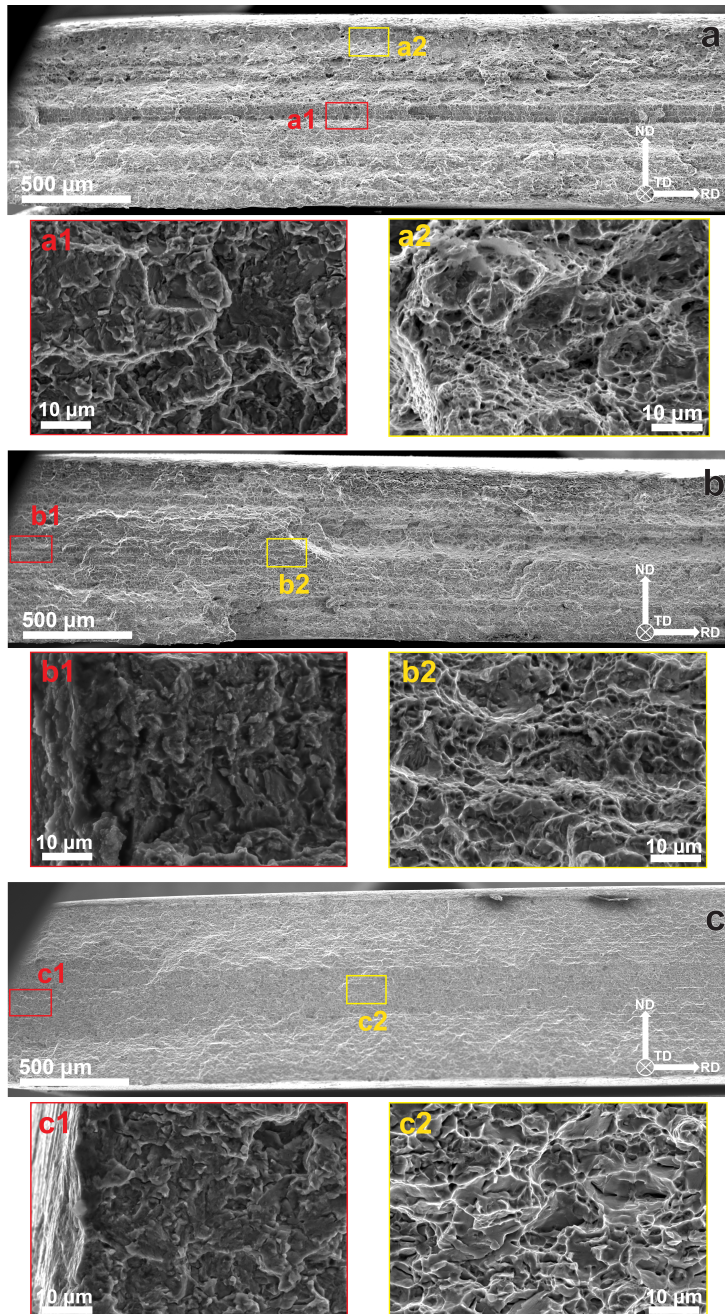


Figure 6.8.: Fracture surface overviews of the a) 590 °C, b) 630 °C, c) 670 °C steels. Insets are shown in red and yellow of brittle and ductile fracture surfaces, respectively.

6.3.4. THE ROLE OF MARTENSITE IN FRACTURE

In order to study the role of martensite on the fracture behaviour of these steels, the fracture surfaces were observed for traces of brittle fracture in the martensitic phase. They are shown in Figure 6.8 which includes higher magnification insets of brittle and ductile fracture zones specifically. A first observation to be made is that there is a distinct fracture band present in the 590 °C steel, that corresponds to a sample-wide zone of brittle fracture relating to the Quasi-Cleavage (QC) fracture mode. Around the band, the fracture surface shows dimples. Similar bands seem to arise in the 630 °C specimens, but the higher magnification insets show a brittle fracture surface only around the short edge of the specimen, whereas the middle exhibits a seemingly mixed-mode fracture between dimples and brittle facets. The 670 °C specimen conversely shows a wider band, but brittle fracture is once again only found near the short edge. The fact that brittle fracture emerges on the short side of all specimens indicates that the crack likely initiated here and propagated along the thickness of the steel sheet towards the middle. It is counter-intuitive, however, that the specimen showing a QC fracture surface most explicitly is the one with the lowest HEI.

In order to elucidate why, cross-sectional SEM micrographs are shown in Figure 6.9. These micrographs show distinct microstructural banding along the rolling direction of the sheet that is still present after the additional heat treatments performed for this work. The 590 °C sample in Figure 6.9a has a similar banding structure to the 630 °C specimen in 6.9b, but since the total martensite content is lower, there is a lesser degree of connection between martensite bands in the ferrite matrix. In other words, there are more uninterrupted sections of ferrite between martensite bands compared to the 630 °C specimen which results in an anisotropic martensitic network structure. This promotes fast fracture propagation within the rolling plane rather than through it, leading to banding on the QC fracture surface. The microstructure is most isotropic in the 670 °C specimen in Figure 6.9c, which translates into more homogeneous crack growth and hydrogen distribution. The effect of a banded microstructure on hydrogen desorption and diffusion has been discussed previously in literature [162], but it has only sparingly been connected to crack propagation paths [163].

Other than the anisotropic martensite distribution, the extent of plastic strain that the 590 °C specimen displays during the in-situ tensile tests also contributes to the formation of the QC fracture band. Chapter 5 of this thesis described how the hydrogen concentration can quickly increase upon plastic deformation in a hydrogen charging environment. KAM maps such as in Figure 6.7 could not be obtained for the specimens annealed at 590 °C, since deformation was too high. However, given that the 590 °C specimens exhibit average fracture strains significantly into the plastic regime, the hydrogen content is likely elevated during the test. This effect was not directly observed, however, since all hydrogen absorption measurements were only performed on undeformed specimens. An elevated martensite concentration near the centre band of the specimen thickness was not observed in Figure 6.9, which suggests that the presence of the brittle QC fracture band in the centre is instead a result of a stress-concentration during deformation or the presence of intermetallic inclusions

such as observed by Depover et al. [164].

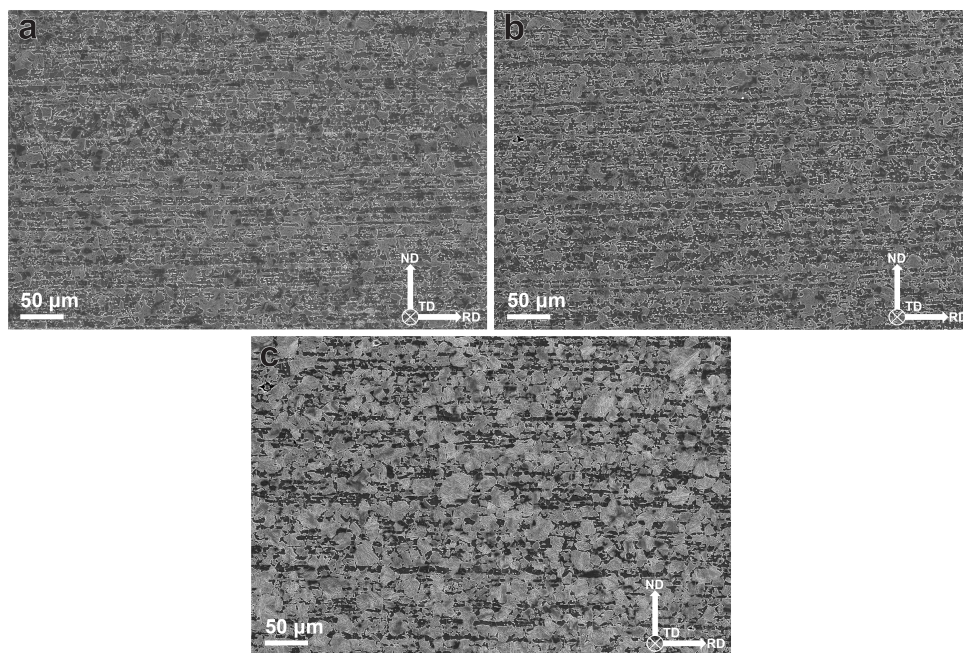


Figure 6.9.: Cross-sectional SEM images of the banded ferrite-martensite structures in the a) 590 °C, b) 630 °C, and c) 670 °C specimens.

6.3.5. THE ROLE OF MARTENSITE IN FRACTURE INITIATION

The banding of brittle fracture surfaces shows the role of martensite in crack propagation, but it also has a significant influence on crack initiation. This effect is clearly observable in fractographic images taken of samples tested as part of a separate study on the as-received DP steel [30]. Figure 6.10 shows two fracture surfaces of samples subjected to conventional tensile tests (strain rate of 0.01 mm/s) after hydrogen charging, where areas showing brittle features are highlighted in red. Figure 6.10a shows the surface of a specimen with an estimated hydrogen content of 3.2 ± 1.0 wppm, based on unfractured identical samples. Fracture initiation can be seen to happen on the right side of the image, after which it propagates into the specimen in a triangular way until the point that crack propagation speed outgrows hydrogen diffusion speed and brittle surface is not formed. This is a common fracture surface as it is seen in literature for higher hydrogen contents of approximately 2 wppm and above [43, 141, 142, 165, 166]. Interestingly, brittle crack initiation also occurs in the specimen shown in Figure 6.10b, which is estimated to have a hydrogen content of only 0.6 ± 0.1 wppm. It is important to note that this test is not performed in-situ, which could cause crack initiation as discussed in Chapter 5, but is instead pre-charged and zinc coated to avoid effusion during the test. It is

therefore surprising that brittle fracture initiation still occurs, especially since the strain rate in this test is high, which would not cause hydrogen accumulation at the notch. Both specimens in Figure 6.10 furthermore show the brittle initiation zone as a rectangularly shaped zone of roughly 100 μm in width.

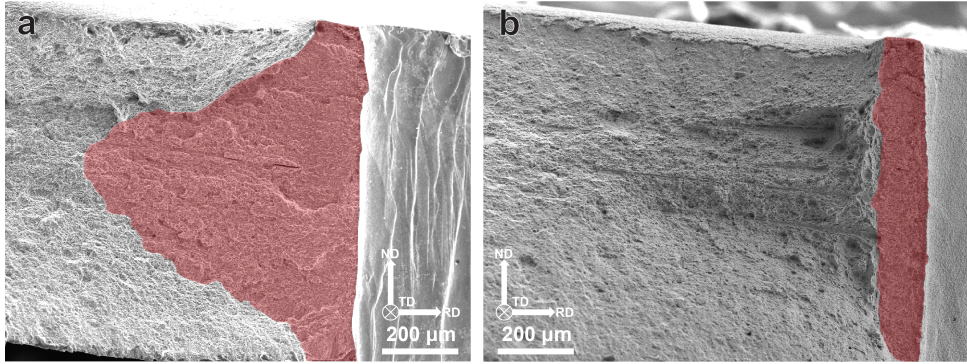


Figure 6.10.: Fracture surfaces as-received DP specimens subjected to a tensile test. Estimated hydrogen contents for these specimens were a) 3.2 ± 1.0 wppm and b) 0.6 ± 0.1 wppm. Brittle fracture surfaces are highlighted in red.

In order to elucidate on the reasons for the formation of the brittle rectangular zone in all specimens, cross-sectional cuts were made on a different specimen, which is shown in Figure 6.11. Image 6.11b shows the geometry of a laser cut notch that was introduced to localise fracture. The figure clearly shows the existence of a surface region that is fully martensitic around the notch. This is a direct result of the laser cutting that was used to machine the notch, which causes local heating and cooling fast enough for martensite to form. Figure 6.11c shows a cross-section of the fracture surface shown in 6.11a that visualises the brittle fracture through the martensitic region. The fracture surface is flat, which is characteristic of brittle QC fracture [71, 167], until it reaches the DP microstructure beyond the martensitic band. After this point it deviates upward and exhibits more deformation of the microstructure that can be observed by the sheared grains. The length of the flat brittle crack surface moreover corresponds to the width of the rectangular brittle zone on the fracture surface in 6.11a. Since this zone even appears on the fracture surface of samples with a low hydrogen concentration as in Figure 6.10b, it can be assumed that the martensite at the surface is supersaturated with hydrogen during charging, and that it does not require slow strain rate testing to initiate brittle fracture.

The same reasoning can be similarly applied to the intercritically annealed samples with varying martensitic content tested in-situ. Cross-sectional electron micrographs of the short and long sides of a 590 $^{\circ}\text{C}$ annealed specimen are shown in Figure 6.12. 6.12a shows the microstructure beneath the surface of the double neck that was cut

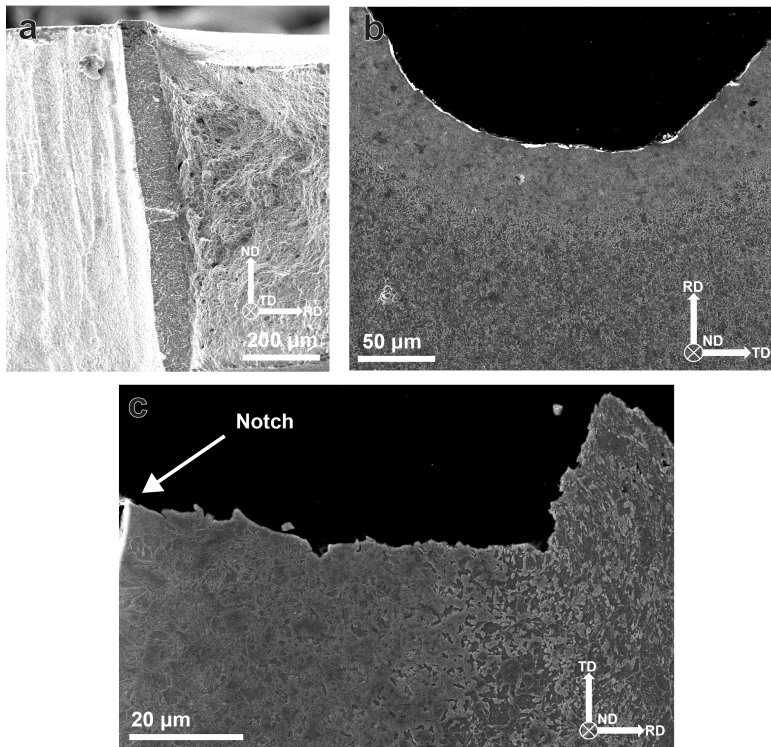


Figure 6.11.: Cross-sections of the as-received DP steel subjected to 40% of the UTS. a) shows a martensitic structure around the notch surface, which corresponds to the brittle fracture zone on b) the fracture surface and c) the fracture cross-section.

using EDM. This method of sample cutting is preferred in hydrogen embrittlement research since it does not induce any deformation nor heat onto the resulting surface except for an oxide layer that can be polished off easily. Since these specimens exhibit a banded microstructure, this means that the martensitic bands will be in contact with the EDM machined surface, as can be seen in 6.12a. On the other hand, the surfaces that were present in the hot-rolling and during the intercritical annealing treatment do not show any presence of martensite in Figure 6.12b. This is likely a result of carbon effusion from the near-surface regions during the intercritical annealing, which inhibited any martensite formation during quenching. Taking into account the presence of martensite on the side surface, it follows that cracks preferentially initiated here since the surface martensite would be saturated with hydrogen during pre-charging of the specimens. Afterwards, the cracks can readily propagate along pre-existing martensite bands to cause high HE in the specimens by the mechanism discussed in Section 6.3.4.

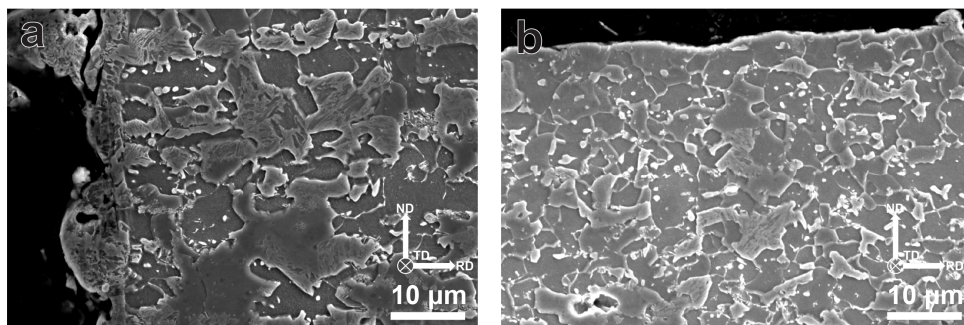


Figure 6.12.: Cross-sections of the microstructure around the surface of a 590 °C specimen. a) the short side edges of the specimen that was machined with EMD and b) the surfaces created after hot rolling.

6.4. CONCLUSIONS

This research shows that increasing the martensitic fraction of DP steels leads to a further uptake in hydrogen, but does not increase the extent of HE any further from the moment a connected martensitic network occurs. The increased uptake is a result of the increase in F/M interphase area, which forms the hydrogen trap in the microstructure and causes fracture initiation. The banded anisotropic microstructure is found to cause preferential crack propagation in the rolling direction, which is most pronounced for DP steels containing approximately 50% martensite. Furthermore, it was found that martensite has a large influence on early crack initiation when it is present on the surface that is being charged with hydrogen. The following conclusions can be drawn from the research performed on DP steels:

- The steel annealed at 630 °C showed the most favourable combination of strength and ductility, with a strength of 1025 ± 8 MPa and a fracture strain of $12.6 \pm 0.6\%$. This steel, as well as that annealed at 670 °C contain connected martensite networks.
- The ferrite/martensite interphase density keeps increasing even after the martensite reaches the required density to form a connected network. This is a result of refinement of ferritic grains resulting in a high aspect ratio and interphase area.
- The steel annealed at 630 °C showed the highest HEI of $86 \pm 10\%$, which is mainly caused by the larger ductility without hydrogen.
- The HEI does not increase further with a higher martensite content since fracture is dominated by crack propagation through the martensitic phase that is connected in the steels with higher martensite content. This has the added effect that the fracture strain of the specimens annealed at 630 and 670 °C are similar.

- Although the steel annealed at 590 °C had the lowest HEI at $51 \pm 39\%$, brittle fracture was most evident on the fracture surface of this steel. The localisation of brittle fracture is a result of an anisotropic microstructure in the rolling direction, combined with plasticity effects that increase and localise the hydrogen content.
- Martensite that is present on the surface acts as a brittle fracture initiation point even at high strain rates. Cracks then readily propagate through connected martensite bands. Martensite present on the surface should therefore be avoided to minimise risk of HE in DP steels.

7

GENERAL DISCUSSION AND CONCLUSIONS

This project was started with the aim of understanding the effects of different microstructural features on the Hydrogen Embrittlement (HE) susceptibility of ferritic Advanced High Strength Steels (AHSS). Research objectives focusing on different microstructural features within ferritic AHSS were outlined in Chapter 1, after which a technical background was established in Chapter 2. Chapters 3 and 4 discuss steels including TiC and VC nano-carbides and discuss the effects of precipitate type and size as well as the charging environment on HE susceptibility. Chapter 5 focuses on the effects of plastic deformation on the extent of HE in a TiC nano-carbide steel, and Chapter 6 deals with the effects of a varying martensite concentration on the HE susceptibility of ferrite/martensite Dual Phase (DP) steels. This chapter has been outlined according to the research objectives for this thesis, listed below:

1. The effect of size and type of nano-precipitates on HE.
2. The effect of different charging environments on precipitate hydrogen trapping.
3. The effects of plastic deformation on HE.
4. The effects of different martensite concentrations on HE in DP steels.

Each following section provides a general discussion relating to one of the research objectives. General conclusions overarching individual chapter contents are given afterwards. Lastly, this chapter provides recommendations, both for steel design to mitigate HE and for opportunities for future research.

7.1. DISCUSSION

7.1.1. THE EFFECTS OF PRECIPITATE SIZE

Precipitate size, and consequently their coherency, were found to be the most important parameters controlling the amount of H absorbed by precipitates. Heat treatments were utilised to create two different size distributions of two precipitate types: TiC and VC. This

resulted in four different steels, that were charged during the heat treatment using high temperature hydrogen gas in Chapter 3. It was observed that incoherent precipitates, especially those larger than 100 nm in size, trap hydrogen inside the precipitate bulk after high temperature charging. The hydrogen trap for both TiC and VC is likely the carbon vacancy. These incoherent precipitates trapped hydrogen exclusively at high activation energies of over 60 kJ/mol which are regarded as irreversible traps that do not desorb hydrogen at room temperature. Larger precipitates have been known to act as crack-initiators [168], but this was not found for the incoherent precipitates in this work. They are both not of a sufficient size to cause crack initiation, and their shape was generally globular, which decreases the amount of stress concentration around their edges compared to cubic or elongated precipitates. In Chapter 4 it was shown that incoherent precipitates do not trap hydrogen at room temperature. This limits their applicability for hydrogen trapping to cases where high temperatures are present, such as the steelmaking processes or transporting high temperature steam. Cases of high temperature gas transport, however, could not be sufficiently tested in the thesis as in-situ testing in gas was not performed.

Room temperature electrochemical charging was shown to be effective in loading (semi-)coherent precipitates with hydrogen in Chapter 4. (Semi-)coherent precipitates of both types were found to trap hydrogen with low activation energies on the order of 20 kJ/mol, which was linked to interface vacancies or misfit dislocations on the precipitate interface as trapping sites. Coherent or semi-coherent precipitates were found to trap more hydrogen than larger incoherent precipitates. Both TiC and VC (semi-)coherent nano-precipitates trap hydrogen on or around the precipitate-matrix interface. Since the surface to volume ratio of smaller precipitates is larger, steels containing the smallest precipitates store more hydrogen than those with larger carbides (2.62 vs 1.53 wppm for the TiC steels). However, this is not the only contributing factor, as the type of hydrogen trap also changes with precipitate size and as a result its coherency with the matrix.

The effects of precipitate hydrogen trapping on mechanical behaviour and embrittlement are also dependent on precipitate size. No embrittlement was found for steels subjected to high temperature gaseous charging where only incoherent precipitates were charged with hydrogen, which is a direct result of their high activation energies for hydrogen desorption. Steels containing (semi-)coherent precipitates were expected to show embrittlement because of their lower activation energies. However, they only showed embrittlement of around 15% in the tensile tests even though they absorbed more hydrogen. Their relative resistance to HE is therefore likely a result of a decreased hydrogen diffusivity due to their high density of (semi-)coherent precipitates. A lower diffusivity causes retardation of hydrogen accumulation at critical regions, which limits HE in these steels even at higher hydrogen contents. Furthermore, steels with smaller precipitates showed a higher strength since smaller precipitates contribute more to precipitation strengthening. These steels therefore performed better overall during the tensile tests.

7.1.2. THE EFFECTS OF PRECIPITATE TYPE

TiC and VC precipitates generally performed similarly during the tests, but some differences were found. The VC precipitates were found to have a higher aspect ratio than their TiC counterparts, which means they can reach a larger critical size before they lose coherency with the matrix. This supports the precipitation strengthening mechanism that gives the VC steels a similar strength to the TiC steels while retaining more ductility, which leads to better overall performance. In terms of hydrogen trapping and embrittlement, however, the difference becomes more pronounced at a larger precipitate size. Firstly, it was observed that incoherent VC precipitates store H all throughout the bulk, whereas incoherent TiC precipitates tend to store it more around their circumference. This is explained to be a result of a higher C-vacancy content in the VC precipitates that can form a connected network that promotes H diffusion further into the precipitate bulk. More importantly, it was found that TiC precipitates have a larger tendency to pin grain boundaries during the heat treatment than their VC counterparts. This results in an elevated concentration of precipitates on grain boundaries after longer heat treatments. These intergranular TiC precipitates cause plasticity localisation during deformation which traps hydrogen and causes increased intergranular fracture. The effect of larger size intergranular TiC precipitates during in-situ testing is therefore detrimental to HE, showing a 37% reduction in ductility, whereas the VC containing steel only showed a reduction of 19%. The overall best performing steel was that containing the smallest VC precipitates, which showed a loss in ductility of only 15% at a higher hydrogen content. Between the two steels with a larger precipitate size, the VC steel also performed better than the TiC steel in terms of both strength and ductility.

7.1.3. THE EFFECTS OF CHARGING ENVIRONMENT

The main finding regarding the hydrogen charging environment is its pivotal role in causing brittle crack propagation and embrittlement. It was shown that if a growing crack tip is cut off from the charging environment through slight crack closure, even if the stress localisation around the crack tip remains, brittle crack propagation does not occur. Hydrogen diffusion from the bulk towards the crack tip in the TiC steel was insufficient to cause further crack growth. In the case that the crack was not closed, and hydrogen could still be absorbed at the crack tip, brittle crack growth was accelerated and significant HE was observed. The presence of hydrogen in environment around the crack tip is therefore more influential in causing HE than the internal hydrogen concentration in this steel. The main difference between gaseous and electrochemical charging is the difference in their capability of charging incoherent carbides with hydrogen. Extra charged hydrogen was found after high temperature gaseous charging, while electrochemical charging was not capable of charging more hydrogen into incoherent carbides than what was already present from the steelmaking process. This is a result of the diffusion barrier that the incoherent precipitate/matrix boundary presents, which can only be overcome at elevated temperatures.

7.1.4. THE EFFECTS OF PLASTIC DEFORMATION

The effects of plastic deformation on the HE of the precipitate steels is significant. It was shown in Chapter 4 that the effects of HE only become apparent after the onset of necking in slow strain rate tests. Necking and fracture were found to be accelerated after the tensile strength was reached but behaviour before this point remained identical regardless of the hydrogen content. Chapter 5 furthermore shows that even after hydrogen charging and plastically deforming a TiC steel up to 3%, which traps significantly more hydrogen (3.69 wppm) than undeformed specimens, it does not embrittle significantly after fast fracture. These findings indicate that hydrogen absorption alone is not enough to cause HE in the precipitate steels. It is only when significant plastic deformation is induced that embrittlement occurs. Moreover, it was discovered through correlation between the dislocation densities and hydrogen contents that the amount of hydrogen stored in dislocations is significantly higher than that observed in precipitates. Even within the elastic regime, only 0.72 wppm of hydrogen could be stored in precipitates out of the total of 2.36 wppm of absorbed hydrogen. This finding shows that the contribution of precipitates to hydrogen trapping is small in the steel. The main postulated reason for the benefit of precipitates against HE, namely their ability to trap hydrogen strongly to avoid hydrogen diffusion, could thus be questioned. Their benefit in precipitation strengthening remains, but for trapping purposes, a higher number of precipitates should ideally be used to provide a more significant benefit to trapping and HE in general.

The requirement of plasticity for hydrogen related fracture mechanisms is something that was found from the research in both the precipitation hardened ferritic steels studied in Chapter 4 and the DP steels studied in Chapter 6. The mechanism that was identified for the accelerated fracture in steel containing intergranular TiC precipitates is a combination between localised plastic deformation around grain boundary precipitates and its interaction with hydrogen. Fracture in the DP steels tested in Chapter 6 also exhibited plasticity localisation around the ferrite/martensite interphase boundary. The steel with a 50% martensite content showed the largest embrittlement with a 89% reduction in ductility. At a fracture strain of 1.8%, high plastic deformation is not observed in the tensile curve. Kernel Average Misorientation (KAM) was used to determine, however, that there is a high degree of plastic deformation localisation around the ferrite/martensite (F/M) interphase boundary. This interphase is argued to be the main hydrogen trapping feature in this steel, as well as the probable location of fracture initiation within the microstructure. This shows similarities to the dislocation pileup around precipitates discussed in Chapter 4, although the martensite content is much higher than that of the precipitates, and plastic strain localisation happens much earlier in the tensile curve for the DP steels. The existence of hard phases in a soft matrix could therefore be seen as a detrimental feature for steels in a hydrogen environment, although successfully dispersing them throughout the microstructure can be a way of partially mitigating HE as well [169].

7.1.5. THE EFFECTS OF MARTENSITE

The presence of martensite in the microstructure was found to be important for both crack initiation and propagation. Of three DP steels with varying martensite content, that with the lowest content of 25% had the highest remaining ductility in a hydrogen environment. 50% martensite content was found to be an optimal amount for both strength and ductility in an environment without hydrogen, but it showed the highest embrittlement of 86% in hydrogen. In fact the fracture strain of the steel with 50% martensite in hydrogen was similar to that of the 78% steel, while the higher martensite content yielded a higher strength. The extra ductility observed in the 50% martensite steel without hydrogen was therefore negated in hydrogen, where the 78% martensite steel retained higher properties overall.

Early fracture initiation was found to happen in locations where martensite was present on the surface, from where continuous martensite bands act as fast crack propagation paths throughout the material. Thus, in this case, the banded microstructure as a result of rolling resulted in preferential crack propagation along the rolling plane. Inside the microstructure, crack initiation and propagation is likely to happen along the F/M interphase because of its role in plasticity localisation and hydrogen trapping. Although hydrogen absorption was found to increase with increasing martensite content, and the consequential increase in F/M interphase density, the embrittlement levelled off at 50% martensite content, when a continuous martensite network is formed within the microstructure.

7.1.6. THE ROLE OF CRACK INITIATION

An important finding from both the precipitation hardened and the DP steels, even though it was not a research objective, was the role of crack initiation and subsequent exposure to the hydrogen environment in causing HE. In the case of electrochemical charging, hydrogen absorption is typically faster than diffusion throughout the microstructure. This creates a localised layer of high hydrogen content around the interface with the electrolyte that is frequently observed to cause brittle fracture some distance into the steel [54]. Phases with a lower diffusivity, such as martensite, are more prone to this effect. The fracture initiation point in DP steels is therefore significantly affected by the presence of martensite on the surface, as was found in Chapter 6. Surface martensite was shown to cause brittle fracture after hydrogen charging even at high strain rates, because it creates a sharp crack that easily propagates along bands of connected martensite. In this case, martensite was connected preferentially along the rolling plane of the steel sheet. Brittle fracture initiation was also observed on the TiC containing steel in Chapter 5, where it was discovered that initiation happened early on in the tensile curve around 1% plastic strain. During the hold phase of the test, brittle crack propagation was hindered by a slight drop in force. Although a significant tensile strength remained, hydrogen supply from the material bulk alone was insufficient to cause further crack growth. Subsequent opening of the crack at a high strain rate caused ductile propagation rather than brittle, as seen in Figure 5.11. Slow Strain Rate tests where the brittle micro-crack was opened while in contact with the electrolyte showed a significantly higher loss in ductility of 60% versus 37%, even though the total hydrogen exposure time was only half as long. Brittle crack

initiation and the interaction between the micro-crack and the hydrogen environment are therefore found to play a pivotal role in HE testing. The overall performance of the steels in an SSRT tests were found to be dependent on the time when fracture initiation occurs, rather than on the amount of absorbed hydrogen, which were found to be independent of each other.

Since the initiation of sharp brittle cracks plays such an important role in HE fracture, the applicability of SSRT testing comes into question. This issue is discussed by Martínez-Pañeda et al. who couple numerical results to trends observed in experimental works to show that microcrack initiation occurs in many different materials at levels far below the failure stress [170]. They mention that "the onset of such cracking can alter the assessment of SSRT results by complicating the interpretation of typical metrics like time-to-failure, breaking stress, and ductility.", and argue that the SSRT test should not be used as a general indication of HE performance. This provides a caveat to the methodologies used in this thesis, although the SSRT test remains an easy, fast and cheap way of testing a material for its general HE performance and its hydrogen-related fracture mechanisms. For more in-depths studies of effect of hydrogen on material performance, however, tests that incorporate the existence of micro-cracks, such as fracture toughness tests, should be included in the scope.

7.2. CONCLUSIONS

The following general conclusions can be drawn from the combined work presented in this thesis:

- Incoherent TiC and VC precipitates can only be charged at high temperature. They trap hydrogen inside carbon vacancies in the precipitate bulk with activation energies of at least 60 kJ/mol and as such do not contribute to embrittlement.
- Coherent and semi-coherent TiC and VC precipitates trap hydrogen on interface interstitials and dislocations, respectively, with trapping energies on the order of 20 kJ/mol. Because the trap sites are present on the interface, more hydrogen is stored in these precipitates than in incoherent ones. Smaller carbides furthermore provide a higher strength as a result of precipitation hardening, without resulting in higher HE susceptibility. Steels containing VC precipitates retain a higher strength and ductility in hydrogen than those containing TiC in this thesis because VC precipitates are more elongated and have a larger critical size for coherency loss.
- TiC precipitates have a larger tendency to pin grain boundaries than their VC counterparts. TiC grain boundary precipitates cause dislocation pile-up upon deformation of the steel. The interaction between these zones of localised plasticity and hydrogen causes accelerated intergranular fracture.
- The TiC containing steel can accommodate increased hydrogen concentrations at low levels of plastic deformation. High levels of plastic deformation in combination with slow strain rates are required to cause HE in this steel.

- Dislocations play a more significant role in hydrogen trapping than precipitates in this work, even in the elastic regime. The main benefit of including precipitates is therefore likely not their hydrogen trapping capacity, but rather their function in retarding hydrogen diffusion throughout the microstructure.
- The main hydrogen trapping site in DP steels is the ferrite/martensite interphase boundary. Plasticity localisation on the boundary interacts with hydrogen to cause crack initiation.
- Martensite present on the steel surface creates zones of early crack initiation in a hydrogen charging environment. Anisotropy in the microstructure causes continuous martensite bands to be present in the rolling plane, which results in preferential crack propagation along the plane.
- All steels tested in this thesis exhibit early crack initiation during in-situ SSRT tests. Crack opening during hydrogen charging is found to govern whether early crack initiation leads to a higher degree of HE. Early crack initiation and propagation during hydrogen charging is of a larger influence to HE performance than the internal hydrogen content.

7.3. RECOMMENDATIONS

The work performed for this thesis has resulted in an increased understanding of the hydrogen related fracture mechanisms in ferritic AHSS. This has led to several recommendations that can be made to guide the design for steels with improved hydrogen resistance. This section lists recommendations for both hydrogen resistant steel design as well as opportunities for future research. The latter has been subdivided further into material-specific recommendations and those applicable to general HE research.

RECOMMENDATIONS FOR HYDROGEN RESISTANT STEEL DESIGN

- Favour the inclusion of small (semi-)coherent precipitates over incoherent ones for room temperature applications. Other than stronger precipitation hardening effects, hydrogen trapping on the interface of (semi-)coherent carbides leads to a higher hydrogen absorption capacity without a reduction in ductility compared to larger precipitates.
- Utilise incoherent carbides for high temperature applications only, since they do not provide any hydrogen trapping capacity at room temperature.
- Avoid the accumulation of precipitates on grain boundaries since they promote plastic deformation localisation and related accelerated intergranular fracture in hydrogen environments.
- Prioritise use of VC instead of TiC precipitates since they provide near identical hydrogen trapping capacity and HE resistance at room temperature at higher strength and ductility levels. At high temperature, incoherent VC precipitates are likely to trap more hydrogen than TiC precipitates.

- Minimise the presence of hard phases such as martensite in surface regions, since they provide sites for accelerated crack initiation.
- Avoid anisotropy in Dual Phase steels. Martensite distribution in DP steels should be well dispersed to avoid preferential crack propagation along martensitic bands.

MATERIAL SPECIFIC RECOMMENDATION FOR FUTURE RESEARCH

- Precipitate types of other elements and stoichiometries should be studied. The precipitates studied in this project were of a relatively simple stoichiometry of 1:1 metal and carbon. Precipitates can be of off-stoichiometric composition, but they can also attract other species to form carbonitrides (e.g. Ti(C,N)) and other compounds. Liu et al. have recently conducted a study on combined Ti and Mo carbides, which increases the amount of hydrogen absorbed by the carbides [171]. Alternatively to different carbides, steels with higher precipitate densities could be studied.
- The effects of precipitates on hydrogen diffusivity should be studied further. It was postulated in this thesis that the contribution of precipitates to diffusivity reduction is of larger influence to HE resistance than to the hydrogen trapping capacity. Studies on diffusivity, however, were not in the scope of the thesis and should therefore be systematically performed to confirm the hypothesis.
- In DP steels, the F/M interphase boundary should be investigated further as a large contributor to hydrogen trapping and crack initiation. Studies done by authors such as Cho et al. have performed in-depth characterisation of fracture in the martensitic phase [172], but crack initiation on the interphase is still a topic that is not fully explored. In this thesis it was shown that the dislocation accumulation at the interphase is the main reason for hydrogen trapping, which suggests that the trap is a dislocation, but the contribution of the F/M interphase itself could not be touched upon in this work, which remains to be determined in future research.
- Microstructural grading should be investigated since it could delay the onset of sub-critical crack initiation. Surface treatments to decrease the presence of surface martensite could for example delay the likelihood of sub-critical cracking in DP steels, resulting in extra ductility for steels that are relatively brittle in hydrogen environments.

RECOMMENDATIONS FOR GENERAL HE RESEARCH

- Extensive microstructural characterisation is required for hydrogen embrittlement research. Since every microstructural feature has some interaction with hydrogen, knowledge of the microstructure beyond the feature of study is important. Exact knowledge of the residing places for hydrogen is hard to obtain beyond simulations or observations of single features. Even hydrogen activation energies obtained from TDS can often be assigned to a range of features with similar energies. Understanding of the interactions between different microstructural features and hydrogen is therefore essential.

- Sub-critical micro-crack initiation should be assumed even for smooth specimens. This project only studied specimens with polished surfaces with the aim of reducing roughness induced effects on sub-surface hydrogen concentrations. However, micro-crack initiation at low strain levels as a result of elevated sub-surface hydrogen concentrations were still observed on most samples. Test methods that include cracks, such as fatigue or fracture toughness tests, should therefore be included to obtain an accurate and in-depth characterisation of a material's resistance to HE.
- The testing environment should mirror the operational environment of the steel as closely as possible. Hydrogen absorption can occur from many different sources. The hydrogen distribution in the steel can differ depending on the source, the temperature and the duration of exposure to hydrogen, as was shown in this case using precipitates. If research is being performed for a specific application, such as corrosion or fatigue, other factors become of interest. Factors such as whether the part is continuously exposed, what the loading conditions are, if the part is coated and if there is any pre-existing deformation. Utilising a testing environment that is different from the operational environment will not lead to a situation where the hydrogen distribution coupled with the load history is entirely representative of the operational environment.
- Hydrogen Embrittlement testing should be performed as if specimens will fail in a brittle way. Throughout this thesis, the importance of plastic deformation in HE fracture has been emphasized. On a macroscopic scale, however, specimens become sensitive to small geometrical defects that can accelerate crack initiation. Ideally notches should be used to force fracture in a pre-defined part of the specimen, to avoid influence of machining defects.
- The influence of elastic and plastic deformation in combination with hydrogen charging should be investigated further. The research performed for this thesis shows that localised plastic strain can lead to early fracture initiation, whereas homogeneous plastic strain can allow for increased hydrogen absorption without microstructural degradation. It discussed the effect of macroscopic plastic deformation before and during hydrogen charging, but did not perform any studies on for example pre-existing localised plasticity or residual stresses from forming operations. These topics are highly relevant for many applications of AHSS and should therefore be investigated more thoroughly.
- Research should be performed on the influence of trace elements on HE in steels. Since the industry is increasingly shifting to manufacturing green steel from scrap, trace elements like boron and copper are expected to increase in concentration over time. The effects of microstructural features involving trace elements are not yet sufficiently understood.

A

SUPPLEMENTARY FIGURES TO CHAPTER 4

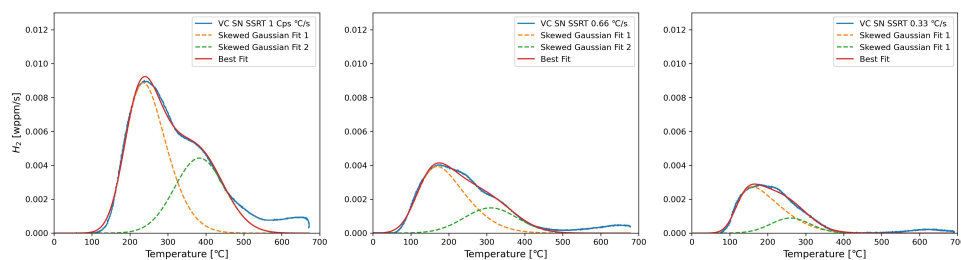


Figure A.1.: **TDS desorption curves.** Curves from all three heating rates including the two deconvoluted skewed gaussian peaks used for calculation of activation energies.

BIBLIOGRAPHY

- [1] International Energy Association. *As their sales continue to rise, SUVs' global CO2 emissions are nearing 1 billion tonnes*. Accessed on April 29th, 2025. Feb. 27, 2023. URL: <https://www.iea.org/commentaries/as-their-sales-continue-to-rise-suvs-global-co2-emissions-are-nearing-1-billion-tonnes>.
- [2] H. Saidpour. "Lightweight high performance materials for car body structures". In: *NTI Technology Conference* (2006).
- [3] J. Galán, L. Samek, P. Verleysen, K. Verbeken, and Y. Houbaert. "Advanced high strength steels for automotive industry". In: *Revista de metalurgia* 48.2 (2012), p. 118.
- [4] A. C. Serrenho, J. B. Norman, and J. M. Allwood. "The impact of reducing car weight on global emissions: the future fleet in Great Britain". In: *Philosophical Transactions of the Royal Society A: Mathematical, Physical and Engineering Sciences* 375.2095 (2017), p. 20160364.
- [5] WorldAutoSteel. *Advanced High-Strength Steel (AHSS) Definitions*. Accessed on April 28th, 2025. URL: <https://www.worldautosteel.org/steel-basics/automotive-advanced-high-strength-steel-ahss-definitions/>.
- [6] W. Zhang and J. Xu. "Advanced lightweight materials for Automobiles: A review". In: *Materials & Design* (2022), p. 110994.
- [7] J. Zhao and Z. Jiang. "Thermomechanical processing of advanced high strength steels". In: *Progress in Materials Science* 94 (2018), pp. 174–242.
- [8] International Energy Association. *How the 2020 Toyota Highlander Hybrid 3-row crossover gets compact-car economy*. Accessed on April 29th, 2025. Apr. 29, 2019. URL: https://www.greencarreports.com/news/1122793_how-the-2020-toyota-highlander-hybrid-3-row-crossover-gets-compact-car-economy.
- [9] Climate TRACE. *Distribution of carbon dioxide emissions produced by the transportation sector worldwide in 2023, by sub sector*. Accessed on May 22nd, 2025. Jan. 23, 2025. URL: <https://www.statista.com/statistics/1185535/transport-carbon-dioxide-emissions-breakdown/>.
- [10] C. T. Sezgin and F. Hayat. "The microstructure and mechanical behavior of TRIP 800 and DP 1000 steels welded by electron beam welding method". In: *Soldagem & Inspeção* 25 (2020), e2526.
- [11] SSAB. *Dual phase (DP) steel: excellent ductility and energy absorption*. Mar. 7, 2025. URL: <https://www.ssab.com/en/brands-and-products/docol/automotive-steel-grades/dual-phase-steel>.

- [12] G. Lovicu, M. Bottazzi, F. D'aiuto, M. De Sanctis, A. Dimatteo, C. Santus, and R. Valentini. "Hydrogen embrittlement of automotive advanced high-strength steels". In: *Metallurgical and Materials Transactions A: Physical Metallurgy and Materials Science* 43.11 (2012), pp. 4075–4087.
- [13] Q. Liu, Q. Zhou, J. Venezuela, M. Zhang, and A. Atrens. "Hydrogen influence on some advanced high-strength steels". In: *Corrosion Science* 125.March (2017), pp. 114–138. ISSN: 0010938X. DOI: [10.1016/j.corsci.2017.06.012](https://doi.org/10.1016/j.corsci.2017.06.012).
- [14] S. K. Dwivedi and M. Vishwakarma. "Effect of hydrogen in advanced high strength steel materials". In: *International Journal of Hydrogen Energy* 44.51 (2019), pp. 28007–28030. ISSN: 03603199. DOI: [10.1016/j.ijhydene.2019.08.149](https://doi.org/10.1016/j.ijhydene.2019.08.149).
- [15] D. Raabe, B. Sun, A. Kwiatkowski Da Silva, B. Gault, H. W. Yen, K. Sedighiani, P. Thouden Sukumar, I. R. Souza Filho, S. Katnagallu, E. Jägler, P. Kürnsteiner, N. Kusampudi, L. Stephenson, M. Herbig, C. H. Liebscher, H. Springer, S. Zaef-ferer, V. Shah, S. L. Wong, C. Baron, M. Diehl, F. Roters, and D. Ponge. "Current Challenges and Opportunities in Microstructure-Related Properties of Advanced High-Strength Steels". In: *Metallurgical and Materials Transactions A: Physical Metallurgy and Materials Science* 51.11 (2020), pp. 5517–5586. ISSN: 10735623. DOI: [10.1007/s11661-020-05947-2](https://doi.org/10.1007/s11661-020-05947-2).
- [16] A. Drexler, B. Helic, Z. Silvayeh, K. Mraczek, C. Sommitsch, and J. Domitner. "The role of hydrogen diffusion, trapping and desorption in dual phase steels". In: *Journal of Materials Science* 57.7 (2022), pp. 4789–4805. ISSN: 15734803. DOI: [10.1007/s10853-021-06830-0](https://doi.org/10.1007/s10853-021-06830-0).
- [17] L. E. Faucon, T. Boot, T. Riemslog, S. P. Scott, P. Liu, and V. Popovich. "Hydrogen-Accelerated Fatigue of API X60 Pipeline Steel and Its Weld". In: *Metals* 13.3 (2023). ISSN: 20754701. DOI: [10.3390/met13030563](https://doi.org/10.3390/met13030563).
- [18] W. H. Johnson. "On some remarkable changes produced in iron and steel by the action of hydrogen and acids". In: *The Royal London Society* (1875). URL: <https://doi.org/10.1098/rspl.1874.0024>.
- [19] D. Casellas, A. Lara, D. Frómeta, D. Gutiérrez, S. Molas, L. Pérez, J. Rehrl, and C. Suppan. "Fracture Toughness to Understand Stretch-Flangeability and Edge Cracking Resistance in AHSS". In: *Metallurgical and Materials Transactions A: Physical Metallurgy and Materials Science* 48.1 (2017), pp. 86–94. ISSN: 10735623. DOI: [10.1007/s11661-016-3815-x](https://doi.org/10.1007/s11661-016-3815-x).
- [20] D. Fan, P. Kaushik, and H. Piolet. "Bend failure mechanism of zinc coated advanced high strength steel". In: *ISIJ International* 58.8 (2018), pp. 1538–1544. ISSN: 09151559. DOI: [10.2355/isijinternational.ISIJINT-2018-132](https://doi.org/10.2355/isijinternational.ISIJINT-2018-132).
- [21] T. Boot, A. Suresh Kumar, S. Eswara, P. Kömmelt, A. Böttger, and V. Popovich. "Hydrogen trapping and embrittlement of titanium- and vanadium carbide-containing steels after high-temperature hydrogen charging". In: *Journal of Materials Science* 59.18 (2024), pp. 7873–7892. ISSN: 15734803. DOI: [10.1007/s10853-024-09611-7](https://doi.org/10.1007/s10853-024-09611-7).

- [22] D. Pérez Escobar, E. Wallaert, L. Duprez, A. Atrens, and K. Verbeken. “Thermal desorption spectroscopy study of the interaction of hydrogen with TiC precipitates”. In: *Metals and Materials International* 19.4 (2013), pp. 741–748. DOI: [10.1007/s12540-013-4013-7](https://doi.org/10.1007/s12540-013-4013-7).
- [23] K. Takai and R. Watanuki. “Hydrogen in trapping states innocuous to environmental degradation of high-strength steels”. In: *ISIJ International* 43.4 (2003), pp. 520–526. ISSN: 09151559. DOI: [10.2355/isijinternational.43.520](https://doi.org/10.2355/isijinternational.43.520).
- [24] T. Depover and K. Verbeken. “The effect of TiC on the hydrogen induced ductility loss and trapping behavior of Fe-C-Ti alloys”. In: *Corrosion Science* 112 (2016), pp. 308–326. DOI: [10.1016/j.corsci.2016.07.013](https://doi.org/10.1016/j.corsci.2016.07.013).
- [25] S. P. Lynch. “Hydrogen embrittlement (HE) phenomena and mechanisms”. In: *Stress corrosion cracking: Theory and practice i* (2011), pp. 90–130. DOI: [10.1533/9780857093769.1.90](https://doi.org/10.1533/9780857093769.1.90).
- [26] J. Takahashi, K. Kawakami, and Y. Kobayashi. “Origin of hydrogen trapping site in vanadium carbide precipitation strengthening steel”. In: *Acta Materialia* 153 (2018), pp. 193–204. ISSN: 13596454.
- [27] F. G. Wei and K. Tsuzaki. “Quantitative analysis on hydrogen trapping of TiC particles in steel”. In: *Metallurgical and Materials Transactions A: Physical Metallurgy and Materials Science* 37.2 (2006), pp. 331–353. DOI: [10.1007/s11661-006-0004-3](https://doi.org/10.1007/s11661-006-0004-3).
- [28] Z. Wang, J. Liu, F. Huang, Y. J. Bi, and S. Q. Zhang. “Hydrogen Diffusion and Its Effect on Hydrogen Embrittlement in DP Steels With Different Martensite Content”. In: *Frontiers in Materials* 7 (2020). ISSN: 22968016. DOI: [10.3389/fmats.2020.620000](https://doi.org/10.3389/fmats.2020.620000). URL: www.frontiersin.org.
- [29] R. G. Davies. “Influence of martensite content on the hydrogen embrittlement of dual-phase steels”. In: *Scripta Metallurgica* 17.7 (1983), pp. 889–892. ISSN: 00369748. DOI: [10.1016/0036-9748\(83\)90255-7](https://doi.org/10.1016/0036-9748(83)90255-7).
- [30] S. Fernández Iniesta. *Fractographic Study on the Effect of Hydrogen Content in a Dual Phase AHSS on the Mechanism of Hydrogen Embrittlement*. External Research Project Report. Delft University of Technology, TATA steel in IJmuiden, June 2023.
- [31] Y. S. Chen, D. Haley, S. S. Gerstl, A. J. London, F. Sweeney, R. A. Wepf, W. M. Rainforth, P. A. Bagot, and M. P. Moody. “Direct observation of individual hydrogen atoms at trapping sites in a ferritic steel”. In: *Science* 355.6330 (2017), pp. 1196–1199. ISSN: 10959203. DOI: [10.1126/science.aal2418](https://doi.org/10.1126/science.aal2418).
- [32] O. De Castro, J.-N. Audinot, H. Q. Hoang, C. Coulbary, O. Bouton, R. Barrahma, A. Ost, C. Stoffels, C. Jiao, M. Dutka, *et al.* “Magnetic Sector Secondary Ion Mass Spectrometry on FIB-SEM Instruments for Nanoscale Chemical Imaging”. In: *Analytical Chemistry* 94.30 (2022), pp. 10754–10763.
- [33] D. Andersen, H. Chen, S. Pal, L. Cressa, O. De Castro, T. Wirtz, G. Schmitz, and S. Eswara. “Correlative high-resolution imaging of hydrogen in Mg₂Ni hydrogen storage thin films”. In: *International Journal of Hydrogen Energy* 48.37 (2023), pp. 13943–13954.

- [34] T. Depover and K. Verbeken. “The detrimental effect of hydrogen at dislocations on the hydrogen embrittlement susceptibility of Fe-C-X alloys: An experimental proof of the HELP mechanism”. In: *International Journal of Hydrogen Energy* 43.5 (2018), pp. 3050–3061. DOI: [10.1016/j.ijhydene.2017.12.109](https://doi.org/10.1016/j.ijhydene.2017.12.109).
- [35] E. Wallaert, T. Depover, M. Arafin, and K. Verbeken. “Thermal desorption spectroscopy evaluation of the hydrogen-trapping capacity of NbC and NbN precipitates”. In: *Metallurgical and Materials Transactions A: Physical Metallurgy and Materials Science*. Vol. 45. 2014, pp. 2412–2420.
- [36] M. B. Djukic, G. M. Bakic, V. S. Zeravcic, A. Sedmak, and B. Rajicic. “Hydrogen embrittlement of industrial components: Prediction, prevention, and models”. In: *Corrosion* 72 (7 2016), pp. 943–961. ISSN: 00109312. DOI: [10.5006/1958](https://doi.org/10.5006/1958).
- [37] M. Panico, D. Baker, S. Nawathe, A. Bahrami, and D. Fairchild. “Effect of testing variables on fracture toughness in sour environment”. In: *Proceedings of the International Offshore and Polar Engineering Conference 2015-Janua* (2015), pp. 134–139. ISSN: 15551792.
- [38] M. Mohtadi-Bonab, M. Eskandari, K. Rahman, R. Ouellet, and J. Szpunar. “An extensive study of hydrogen-induced cracking susceptibility in an API X60 sour service pipeline steel”. In: *International Journal of Hydrogen Energy* 41 (7 Feb. 2016), pp. 4185–4197. ISSN: 0360-3199. DOI: [10.1016/J.IJHYDENE.2016.01.031](https://doi.org/10.1016/J.IJHYDENE.2016.01.031).
- [39] Z. Liu, X. Wang, C. Du, J. Li, and X. Li. “Effect of hydrogen-induced plasticity on the stress corrosion cracking of X70 pipeline steel in simulated soil environments”. In: *Materials Science and Engineering: A* 658 (Mar. 2016), pp. 348–354. ISSN: 0921-5093. DOI: [10.1016/J.MSEA.2016.02.019](https://doi.org/10.1016/J.MSEA.2016.02.019).
- [40] A. Drexler, L. Vandewalle, T. Depover, K. Verbeken, and J. Domitner. “Critical verification of the Kissinger theory to evaluate thermal desorption spectra”. In: *International Journal of Hydrogen Energy* 46.79 (2021), pp. 39590–39606. DOI: [10.1016/j.ijhydene.2021.09.171](https://doi.org/10.1016/j.ijhydene.2021.09.171).
- [41] C. F. Dong, X. G. Li, Z. Y. Liu, and Y. R. Zhang. “Hydrogen-induced cracking and healing behaviour of X70 steel”. In: *Journal of Alloys and Compounds* 484.1-2 (Sept. 2009), pp. 966–972. ISSN: 09258388. DOI: [10.1016/j.jallcom.2009.05.085](https://doi.org/10.1016/j.jallcom.2009.05.085). URL: <https://www.sciencedirect.com/science/article/pii/S0925838809010627>.
- [42] J. Venezuela, E. Gray, Q. Liu, Q. Zhou, C. Tapia-Bastidas, M. Zhang, and A. Atrens. “Equivalent hydrogen fugacity during electrochemical charging of some martensitic advanced high-strength steels”. In: *Corrosion Science* 127 (2017), pp. 45–58. ISSN: 0010938X. DOI: [10.1016/j.corsci.2017.08.011](https://doi.org/10.1016/j.corsci.2017.08.011). URL: <http://dx.doi.org/10.1016/j.corsci.2017.08.011>.
- [43] J. Sanchez, S. F. Lee, M. A. Martin-Rengel, J. Fullea, C. Andrade, and J. Ruiz-Hervías. “Measurement of hydrogen and embrittlement of high strength steels”. In: *Engineering Failure Analysis* 59 (2016), pp. 467–477. ISSN: 13506307. DOI: [10.1016/j.engfailanal.2015.11.001](https://doi.org/10.1016/j.engfailanal.2015.11.001).

- [44] L. Péter, E. Szücs, L. Filák, B. Verö, and H. Schneider. “Electrochemical hydrogen permeation on steel sheets with in situ electrodeposition of a Pd layer at the exit side”. In: *Journal of Applied Electrochemistry* 33.7 (2003), pp. 613–617. ISSN: 0021891X. DOI: [10.1023/A:1024990905361](https://doi.org/10.1023/A:1024990905361).
- [45] M. Wang, E. Akiyama, and K. Tsuzaki. “Effect of hydrogen and stress concentration on the notch tensile strength of AISI 4135 steel”. In: *Materials Science and Engineering A* 398.1-2 (2005), pp. 37–46. ISSN: 09215093. DOI: [10.1016/j.msea.2005.03.008](https://doi.org/10.1016/j.msea.2005.03.008).
- [46] Q. S. Allen and T. W. Nelson. “Microstructural evaluation of hydrogen embrittlement and successive recovery in advanced high strength steel”. In: *Journal of Materials Processing Technology* 265. September 2018 (2019), pp. 12–19. ISSN: 09240136. DOI: [10.1016/j.jmatprotec.2018.09.039](https://doi.org/10.1016/j.jmatprotec.2018.09.039). URL: <https://doi.org/10.1016/j.jmatprotec.2018.09.039>.
- [47] S. Zhang, E. Fan, J. Wan, J. Liu, Y. Huang, and X. Li. “Effect of Nb on the hydrogen-induced cracking of high-strength low-alloy steel”. In: *Corrosion Science* 139 (2018), pp. 83–96. ISSN: 0010938X. DOI: [10.1016/j.corsci.2018.04.041](https://doi.org/10.1016/j.corsci.2018.04.041).
- [48] M. A. Mohtadi-Bonab, J. A. Szpunar, and S. S. Razavi-Tousi. “A comparative study of hydrogen induced cracking behavior in API 5L X60 and X70 pipeline steels”. In: *Engineering Failure Analysis* 33 (Oct. 2013), pp. 163–175. ISSN: 13506307. DOI: [10.1016/j.engfailanal.2013.04.028](https://doi.org/10.1016/j.engfailanal.2013.04.028). URL: <https://www.sciencedirect.com/science/article/pii/S1350630713001647>.
- [49] Y. Murakami and S. Matsuoka. “Effect of hydrogen on fatigue crack growth of metals”. In: *Engineering Fracture Mechanics* 77.11 (July 2010), pp. 1926–1940. ISSN: 00137944. DOI: [10.1016/j.engfracmech.2010.04.012](https://doi.org/10.1016/j.engfracmech.2010.04.012). URL: <https://www.sciencedirect.com/science/article/pii/S0013794410001980>.
- [50] M. Koyama, D. Yamasaki, T. Nagashima, C. C. Tasan, and K. Tsuzaki. “In situ observations of silver-decoration evolution under hydrogen permeation: Effects of grain boundary misorientation on hydrogen flux in pure iron”. In: *Scripta Materialia* 129 (2017), pp. 48–51. ISSN: 13596462. DOI: [10.1016/j.scriptamat.2016.10.027](https://doi.org/10.1016/j.scriptamat.2016.10.027). URL: <http://dx.doi.org/10.1016/j.scriptamat.2016.10.027>.
- [51] Y. Wang, S. Hu, Y. Li, and G. Cheng. “Improved hydrogen embrittlement resistance after quenching–tempering treatment for a Cr-Mo-V high strength steel”. In: *International Journal of Hydrogen Energy* 44.54 (2019), pp. 29017–29026. ISSN: 03603199. DOI: [10.1016/j.ijhydene.2019.09.142](https://doi.org/10.1016/j.ijhydene.2019.09.142). URL: <https://doi.org/10.1016/j.ijhydene.2019.09.142>.
- [52] A. Sieverts. “The absorption of gases by metals”. In: *Zeitschrift für Metallkunde* 21 (1929), pp. 37–46.
- [53] J. P. Hirth. “Effects of hydrogen on the properties of iron and steel”. In: *Metallurgical Transactions A* 11.6 (1980), pp. 861–890. ISSN: 03602133. DOI: [10.1007/BF02654700](https://doi.org/10.1007/BF02654700).

- [54] Y. Zhao, M. Y. Seok, I. C. Choi, Y. H. Lee, S. J. Park, U. Ramamurty, J. Y. Suh, and J. I. Jang. "The role of hydrogen in hardening/softening steel: Influence of the charging process". In: *Scripta Materialia* 107 (Oct. 2015), pp. 46–49. DOI: [10.1016/j.scriptamat.2015.05.017](https://doi.org/10.1016/j.scriptamat.2015.05.017).
- [55] I. Maroef, D. Olson, M. Eberhart, and G. Edwards. "Hydrogen trapping in ferritic steel weld metal". In: *International Materials Reviews* 47.4 (2002), pp. 191–223.
- [56] M. Dadfarnia, P. Sofronis, and T. Neeraj. "Hydrogen interaction with multiple traps: Can it be used to mitigate embrittlement?" In: *International Journal of Hydrogen Energy* 36.16 (2011), pp. 10141–10148.
- [57] P. Castaño Rivera, V. Ramunni, and P. Bruzzoni. "Hydrogen trapping in an API 5L X60 steel". In: *Corrosion Science* 54 (2012), pp. 106–118. ISSN: 0010-938X. DOI: <https://doi.org/10.1016/j.corsci.2011.09.008>.
- [58] A. Turnbull. "Hydrogen diffusion and trapping in metals". In: *Gaseous hydrogen embrittlement of materials in energy technologies*. Elsevier, 2012, pp. 89–128.
- [59] A. R. Troiano. "The role of hydrogen and other interstitials in the mechanical behavior of metals". In: *trans. ASM* 52 (1960), pp. 54–80.
- [60] R. Oriani and P. Josephic. "Equilibrium aspects of hydrogen-induced cracking of steels". In: *Acta Metallurgica* 22.9 (1974), pp. 1065–1074.
- [61] A. Arora, R. Kumar, H. Singh, and D. K. Mahajan. "Hydrogen assisted crack initiation in metals under monotonic loading: A new experimental approach". In: *Theoretical and Applied Fracture Mechanics* (2021), p. 102917.
- [62] H. Najam, M. Koyama, B. Bal, E. Akiyama, and K. Tsuzaki. "Strain rate and hydrogen effects on crack growth from a notch in a Fe-high-Mn steel containing 1.1 wt% solute carbon". In: *International Journal of Hydrogen Energy* 45.1 (Jan. 2020), pp. 1125–1139. ISSN: 03603199. DOI: [10.1016/j.ijhydene.2019.10.227](https://doi.org/10.1016/j.ijhydene.2019.10.227).
- [63] H. Liu, S. Hamada, M. Koyama, and H. Noguchi. "Distinguishing geometric and metallurgic hydrogen-embrittlement susceptibilities in pre-cracked structures made of interstitial-free steel under monotonic tension". In: *Theoretical and Applied Fracture Mechanics* 108 (2020).
- [64] X. Sun, J. Kang, and Q. Yong. "Revealing the difference of precipitation kinetics between TiC and VC in low-carbon tempered martensitic steels". In: *Journal of Materials Science* 55.33 (2020), pp. 16018–16032. ISSN: 15734803. DOI: [10.1007/s10853-020-05176-3](https://doi.org/10.1007/s10853-020-05176-3).
- [65] M. Koyama, C. C. Tasan, E. Akiyama, K. Tsuzaki, and D. Raabe. "Hydrogen-assisted decohesion and localized plasticity in dual-phase steel". In: *Acta Materialia* 70 (May 2014), pp. 174–187. ISSN: 13596454. DOI: [10.1016/j.actamat.2014.01.048](https://doi.org/10.1016/j.actamat.2014.01.048).
- [66] M. Wang, C. C. Tasan, M. Koyama, D. Ponge, and D. Raabe. "Enhancing Hydrogen Embrittlement Resistance of Lath Martensite by Introducing Nano-Films of Interlath Austenite". In: *Metallurgical and Materials Transactions A: Physical Metallurgy and Materials Science* 46.9 (2015), pp. 3797–3802.

- [67] A. Nagao, M. L. Martin, M. Dadfarnia, P. Sofronis, and I. M. Robertson. “The effect of nanosized (Ti,Mo)C precipitates on hydrogen embrittlement of tempered lath martensitic steel”. In: *Acta Materialia* 74 (2014), pp. 244–254.
- [68] J. Lee, T. Lee, D. J. Mun, C. M. Bae, and C. S. Lee. “Comparative study on the effects of Cr, V, and Mo carbides for hydrogen-embrittlement resistance of tempered martensitic steel”. In: *Scientific Reports* 9.1 (2019).
- [69] C. D. Beachem. “A New Model for Hydrogen-Assisted Cracking (Hydrogen "Embrittlement")”. In: *Metallurgical Transactions* (1972), pp. 437–451.
- [70] I. M. Robertson. “The effect of hydrogen on dislocation dynamics”. In: *Engineering Fracture Mechanics* 64.5 (1999), pp. 649–673.
- [71] M. L. Martin, J. A. Fenske, G. S. Liu, P. Sofronis, and I. M. Robertson. “On the formation and nature of quasi-cleavage fracture surfaces in hydrogen embrittled steels”. In: *Acta Materialia* 59.4 (2011), pp. 1601–1606. ISSN: 13596454. DOI: [10.1016/j.actamat.2010.11.024](https://doi.org/10.1016/j.actamat.2010.11.024).
- [72] C. Hwang and I. Bernstein. “Dislocation transport of hydrogen in iron single crystals”. In: *Acta Metallurgica* 34.6 (1986), pp. 1001–1010.
- [73] J. A. Clum. “The role of hydrogen in dislocation generation in iron alloys”. In: *Scripta Metallurgica* 9.1 (1975), pp. 51–58.
- [74] S. P. Lynch. “Environmentally assisted cracking: Overview of evidence for an adsorption-induced localised-slip process”. In: *Acta Metallurgica* 36.10 (1988), pp. 2639–2661.
- [75] S. P. Lynch. “Mechanisms of hydrogen assisted cracking—a review”. In: *Hydrogen effects on material behaviour and corrosion deformation interactions* (2003), pp. 449–466.
- [76] M. Nagumo. “Hydrogen related failure of steels - A new aspect”. In: *Materials Science and Technology* 20.8 (2004), pp. 940–950.
- [77] M. Nagumo. *Fundamentals of hydrogen embrittlement*. Springer, 2016.
- [78] R. B. McLellan and Z. R. Xu. “Hydrogen-induced vacancies in the iron lattice”. In: *Scripta Materialia* 36.10 (May 1997).
- [79] M. Wasim, M. B. Djukic, and T. D. Ngo. “Influence of hydrogen-enhanced plasticity and decohesion mechanisms of hydrogen embrittlement on the fracture resistance of steel”. In: *Engineering Failure Analysis* 123. February (2021), p. 105312. ISSN: 13506307. DOI: [10.1016/j.engfailanal.2021.105312](https://doi.org/10.1016/j.engfailanal.2021.105312).
- [80] Y. Toji, S. Takagi, K. Hasegawa, and K. Seto. “Influence of low-temperature heat treatment after deformation on hydrogen entry into steel sheets”. In: *ISIJ International* 52.2 (2012), pp. 274–280. ISSN: 09151559. DOI: [10.2355/isijinternational.52.274](https://doi.org/10.2355/isijinternational.52.274).
- [81] M. Nagumo, K. Takai, and N. Okuda. “Nature of hydrogen trapping sites in steels induced by plastic deformation”. In: *Journal of Alloys and Compounds* 293 (1999), pp. 310–316. ISSN: 09258388. DOI: [10.1016/S0925-8388\(99\)00322-9](https://doi.org/10.1016/S0925-8388(99)00322-9).

- [82] H. Li, J. Venezuela, Q. Zhou, Z. Shi, M. Yan, R. Knibbe, M. Zhang, F. Dong, and A. Atrens. "Effect of plastic strain damage on the hydrogen embrittlement of a dual-phase (DP) and a quenching and partitioning (Q&P) advanced high-strength steel". In: *Materials Science and Engineering: A* 785. April (2020), p. 139343. ISSN: 09215093. DOI: [10.1016/j.msea.2020.139343](https://doi.org/10.1016/j.msea.2020.139343). URL: <https://doi.org/10.1016/j.msea.2020.139343>.
- [83] G. Pressouyre. "A classification of hydrogen traps in steel". In: *Metallurgical Transactions A* 10 (1979), pp. 1571–1573.
- [84] Y. S. Chen, H. Lu, J. Liang, A. Rosenthal, H. Liu, G. Sneddon, I. McCarroll, Z. Zhao, W. Li, A. Guo, and J. M. Cairney. "Observation of hydrogen trapping at dislocations, grain boundaries, and precipitates". In: *Science* 367.6474 (2020), pp. 171–175. ISSN: 10959203. DOI: [10.1126/science.aaz0122](https://doi.org/10.1126/science.aaz0122). URL: <http://science.sciencemag.org/>.
- [85] P. Ferreira, I. Robertson, and H. Birnbaum. "Hydrogen effects on the interaction between dislocations". In: *Acta materialia* 46.5 (1998), pp. 1749–1757.
- [86] A. Turk, G. R. Joshi, M. Gintalas, M. Callisti, P. E. Rivera-Díaz-del-Castillo, and E. I. Galindo-Nava. "Quantification of hydrogen trapping in multiphase steels: Part I – Point traps in martensite". In: *Acta Materialia* 194 (2020), pp. 118–133. ISSN: 13596454. DOI: [10.1016/j.actamat.2020.05.007](https://doi.org/10.1016/j.actamat.2020.05.007).
- [87] S. Bechtle, M. Kumar, B. P. Somerday, M. E. Launey, and R. O. Ritchie. "Grain-boundary engineering markedly reduces susceptibility to intergranular hydrogen embrittlement in metallic materials". In: *Acta Materialia* 57.14 (2009), pp. 4148–4157. ISSN: 13596454. DOI: [10.1016/j.actamat.2009.05.012](https://doi.org/10.1016/j.actamat.2009.05.012).
- [88] Y. J. Kwon, H. J. Seo, J. N. Kim, and C. S. Lee. "Effect of grain boundary engineering on hydrogen embrittlement in Fe-Mn-C TWIP steel at various strain rates". In: *Corrosion Science* 142. July (2018), pp. 213–221. ISSN: 0010938X. DOI: [10.1016/j.corsci.2018.07.028](https://doi.org/10.1016/j.corsci.2018.07.028).
- [89] D. Korzekwa, D. Matlock, and G. Krauss. "Dislocation substructure as a function of strain in a dual-phase steel". In: *Metallurgical and Materials Transactions A* 15.6 (1984), pp. 1221–1228.
- [90] H. Ghadbeigi, C. Pinna, S. Celotto, and J. Yates. "Local plastic strain evolution in a high strength dual-phase steel". In: *Materials Science and Engineering: A* 527.18-19 (2010), pp. 5026–5032.
- [91] Y. Momotani, A. Shibata, D. Terada, and N. Tsuji. "Effect of strain rate on hydrogen embrittlement in low-carbon martensitic steel". In: *International Journal of Hydrogen Energy* 42.5 (2017), pp. 3371–3379. ISSN: 03603199. DOI: [10.1016/j.ijhydene.2016.09.188](https://doi.org/10.1016/j.ijhydene.2016.09.188).
- [92] W. Callister and D. G. Rethwisch. *Materials Science and Engineering*. Vol. 8. John Wiley & Sons, 2011.
- [93] S. M. Lee and J. Y. Lee. "The effect of the interface character of TiC particles on hydrogen trapping in steel". In: *Acta Metallurgica* 35.11 (1987), pp. 2695–2700. ISSN: 00016160. DOI: [10.1016/0001-6160\(87\)90268-9](https://doi.org/10.1016/0001-6160(87)90268-9).

- [94] M. Ohnuma, J.-i. Suzuki, F.-G. Wei, and K. Tsuzaki. "Direct observation of hydrogen trapped by NbC in steel using small-angle neutron scattering". In: *Scripta Materialia* 58.2 (2008), pp. 142–145.
- [95] K. Kawakami and T. Matsumiya. "Numerical analysis of hydrogen trap state by TiC and V₄C₃ in bcc-Fe". In: *ISIJ international* 52.9 (2012), pp. 1693–1697.
- [96] S. Sagar, M. H. Sluiter, and P. Dey. "First - Principles study of hydrogen - Carbide interaction in bcc Fe". In: *International Journal of Hydrogen Energy* 50 (2024), pp. 211–223. ISSN: 03603199. DOI: [10.1016/j.ijhydene.2023.09.222](https://doi.org/10.1016/j.ijhydene.2023.09.222).
- [97] Y. Park, I. Maroef, A. Landau, and D. Olson. "Retained austenite as a hydrogen trap in steel welds". In: *Welding Journal-New York-* 81.2 (2002), 27–S.
- [98] S. Li, Y. Li, Y. C. Lo, T. Neeraj, R. Srinivasan, X. Ding, J. Sun, L. Qi, P. Gumbsch, and J. Li. "The interaction of dislocations and hydrogen-vacancy complexes and its importance for deformation-induced proto nano-voids formation in α -Fe". In: *International Journal of Plasticity* 74 (2015), pp. 175–191. ISSN: 07496419. DOI: [10.1016/j.ijplas.2015.05.017](https://doi.org/10.1016/j.ijplas.2015.05.017).
- [99] F. Wei, T. Hara, and K. Tsuzaki. "Precise determination of the activation energy for desorption of hydrogen in two Ti-added steels by a single thermal-desorption spectrum". In: *Metallurgical and Materials Transactions* 35.3 (2004), p. 587.
- [100] F.-G. Wei, T. Hara, T. Tsuchida, and K. Tsuzaki. "Hydrogen trapping in quenched and tempered 0.42 C-0.30 Ti steel containing bimodally dispersed TiC particles". In: *ISIJ international* 43.4 (2003), pp. 539–547.
- [101] F. G. Wei, T. Hara, and K. Tsuzaki. "High-resolution transmission electron microscopy study of crystallography and morphology of TiC precipitates in tempered steel". In: *Philosophical Magazine* 84.17 (2004), pp. 1735–1751. ISSN: 14786435. DOI: [10.1080/14786430310001638762](https://doi.org/10.1080/14786430310001638762).
- [102] G. Pressouyre and I. Bernstein. "A quantitative analysis of hydrogen trapping". In: *Metallurgical transactions A* 9 (1978), pp. 1571–1580.
- [103] S. E. Restrepo, D. Di Stefano, M. Mrovec, and A. T. Paxton. "Density functional theory calculations of iron-vanadium carbide interfaces and the effect of hydrogen". In: *International Journal of Hydrogen Energy* 45.3 (2020), pp. 2382–2389.
- [104] B. Zhang, J. Su, M. Wang, Z. Liu, Z. Yang, M. Militzer, and H. Chen. "Atomistic insight into hydrogen trapping at MC/BCC-Fe phase boundaries: The role of local atomic environment". In: *Acta Materialia* 208 (2021), p. 116744.
- [105] T. Depover and K. Verbeken. "Evaluation of the effect of V₄C₃ precipitates on the hydrogen induced mechanical degradation in Fe-CV alloys". In: *Materials Science and Engineering: A* 675 (2016), pp. 299–313.
- [106] E. V. den Eeckhout, K. Verbeken, and T. Depover. "Methodology of the electrochemical hydrogen permeation test: A parametric evaluation". In: *International Journal of Hydrogen Energy* 48 (78 Sept. 2023), pp. 30585–30607. ISSN: 03603199. DOI: [10.1016/j.ijhydene.2023.04.211](https://doi.org/10.1016/j.ijhydene.2023.04.211).

- [107] D. Hardie and S. Liu. “The effect of stress concentration on hydrogen embrittlement of a low alloy steel”. In: *Corrosion Science* 38.5 (1996), pp. 721–733. ISSN: 0010938X. DOI: [10.1016/0010-938X\(96\)00161-8](https://doi.org/10.1016/0010-938X(96)00161-8).
- [108] M. Wang, E. Akiyama, and K. Tsuzaki. “Crosshead speed dependence of the notch tensile strength of a high strength steel in the presence of hydrogen”. In: *Scripta Materialia* 53.6 (Sept. 2005), pp. 713–718. ISSN: 13596462. DOI: [10.1016/j.scriptamat.2005.05.014](https://doi.org/10.1016/j.scriptamat.2005.05.014). URL: <https://www.sciencedirect.com/science/article/pii/S1359646205003180>.
- [109] N. E. Nanninga, Y. S. Levy, E. S. Drexler, R. T. Condon, A. E. Stevenson, and A. J. Slifka. “Comparison of hydrogen embrittlement in three pipeline steels in high pressure gaseous hydrogen environments”. In: *Corrosion Science* 59 (June 2012), pp. 1–9. ISSN: 0010938X. DOI: [10.1016/j.corsci.2012.01.028](https://doi.org/10.1016/j.corsci.2012.01.028). URL: <https://www.sciencedirect.com/science/article/pii/S0010938X12000625>.
- [110] ASTM G142. “Standard Test Method for Determination of Susceptibility of Metals to Embrittlement in Hydrogen Containing Environments at High Pressure, High Temperature, or Both”. In: *ASTM Book of Standards* 03.Reapproved 2016 (1998), pp. 1–8. DOI: [10.1520/G0142-98R16.2](https://doi.org/10.1520/G0142-98R16.2).
- [111] A. Laureys, L. Claeys, T. De Seranno, T. Depover, E. Van den Eeckhout, R. Petrov, and K. Verbeken. “The role of titanium and vanadium based precipitates on hydrogen induced degradation of ferritic materials”. In: *Materials Characterization* 144.May (2018), pp. 22–34. ISSN: 10445803. DOI: [10.1016/j.matchar.2018.06.030](https://doi.org/10.1016/j.matchar.2018.06.030).
- [112] L. Vandewalle, T. Depover, and K. Verbeken. “Hydrogen trapping of carbides during high temperature gaseous hydrogenation”. In: *International Journal of Hydrogen Energy* xxxx (2023). ISSN: 0360-3199. DOI: [10.1016/j.ijhydene.2023.04.348](https://doi.org/10.1016/j.ijhydene.2023.04.348).
- [113] B. Malard, B. Remy, C. Scott, A. Deschamps, J. Chêne, T. Dieudonné, and M. H. Mathon. “Hydrogen trapping by VC precipitates and structural defects in a high strength Fe-Mn-C steel studied by small-angle neutron scattering”. In: *Materials Science and Engineering A* 536 (2012), pp. 110–116. DOI: [10.1016/j.msea.2011.12.080](https://doi.org/10.1016/j.msea.2011.12.080).
- [114] M. Wang, E. Akiyama, and K. Tsuzaki. “Effect of hydrogen on the fracture behavior of high strength steel during slow strain rate test”. In: *Corrosion Science* 49.11 (Nov. 2007), pp. 4081–4097. DOI: [10.1016/j.corsci.2007.03.038](https://doi.org/10.1016/j.corsci.2007.03.038).
- [115] O. Barrera, D. Bombac, Y. Chen, T. D. Daff, E. Galindo-Nava, P. Gong, D. Haley, R. Horton, I. Katarov, J. R. Kermode, C. Liverani, M. Stopher, and F. Sweeney. “Understanding and mitigating hydrogen embrittlement of steels: a review of experimental, modelling and design progress from atomistic to continuum”. In: *Journal of Materials Science* 53.9 (2018), pp. 6251–6290. ISSN: 15734803. DOI: [10.1007/s10853-017-1978-5](https://doi.org/10.1007/s10853-017-1978-5).

- [116] J. A. Ronevich and B. P. Somerday. “Assessing gaseous hydrogen assisted fatigue crack growth susceptibility of pipeline steel weld fusion zones and heat affected zones”. In: *Materials Performance and Characterization* 5.3 (2016), pp. 290–304. ISSN: 21653992. DOI: [10.1520/MPC20150057](https://doi.org/10.1520/MPC20150057).
- [117] F. G. Wei and K. Tsuzaki. “Hydrogen absorption of incoherent TiC particles in iron from environment at high temperatures”. In: *Metallurgical and Materials Transactions A: Physical Metallurgy and Materials Science* 35 A.10 (2004), pp. 3155–3163. DOI: [10.1007/s11661-004-0060-5](https://doi.org/10.1007/s11661-004-0060-5).
- [118] D. Di Stefano, R. Nazarov, T. Hickel, J. Neugebauer, M. Mrovec, and C. Elsässer. “First-principles investigation of hydrogen interaction with TiC precipitates in α -Fe”. In: *Physical Review B* 93.18 (2016), p. 184108.
- [119] J. Takahashi, K. Kawakami, Y. Kobayashi, and T. Tarui. “The first direct observation of hydrogen trapping sites in TiC precipitation-hardening steel through atom probe tomography”. In: *Scripta Materialia* 63.3 (2010), pp. 261–264. DOI: [10.1016/j.scriptamat.2010.03.012](https://doi.org/10.1016/j.scriptamat.2010.03.012).
- [120] R. Salehin, G. B. Thompson, and C. R. Weinberger. “Hydrogen trapping and storage in the group IVB-VIB transition metal carbides”. In: *Materials and Design* 214 (2022), p. 110399. ISSN: 18734197. DOI: [10.1016/j.matdes.2022.110399](https://doi.org/10.1016/j.matdes.2022.110399).
- [121] R. Baker. “Precipitation processes in steels”. In: *ISI Spec. Rep.* 64 (1959), p. 1.
- [122] J. Takahashi, K. Kawakami, and T. Tarui. “Direct observation of hydrogen-trapping sites in vanadium carbide precipitation steel by atom probe tomography”. In: *Scripta Materialia* 67.2 (2012), pp. 213–216.
- [123] Y. Ma, Y. Shi, H. Wang, Z. Mi, Z. Liu, L. Gao, Y. Yan, Y. Su, and L. Qiao. “A first-principles study on the hydrogen trap characteristics of coherent nano-precipitates in α -Fe”. In: *International Journal of Hydrogen Energy* 45.51 (2020), pp. 27941–27949. ISSN: 03603199. DOI: [10.1016/j.ijhydene.2020.07.123](https://doi.org/10.1016/j.ijhydene.2020.07.123).
- [124] S. Tang, L. Li, H. Yan, J. Jin, Q. Peng, M. Cai, J. Li, Z. Liu, and G. Wang. “Hydrogen trapping in vanadium carbide alloyed with transition metals”. In: *Nuclear Materials and Energy* 36.September (2023), p. 101504. ISSN: 23521791. DOI: [10.1016/j.nme.2023.101504](https://doi.org/10.1016/j.nme.2023.101504).
- [125] S. Tang, L. X. Li, Q. Peng, H. L. Yan, M. H. Cai, J. P. Li, Z. Y. Liu, and G. D. Wang. *First-principles insights into hydrogen trapping in interstitial-vacancy complexes in vanadium carbide*. 2022. DOI: [10.1039/d2cp02425j](https://doi.org/10.1039/d2cp02425j).
- [126] H. J. Seo, J. N. Kim, J. W. Jo, and C. S. Lee. “Effect of tempering duration on hydrogen embrittlement of vanadium-added tempered martensitic steel”. In: *International Journal of Hydrogen Energy* 46.37 (2021), pp. 19670–19681. ISSN: 03603199. DOI: [10.1016/j.ijhydene.2021.03.109](https://doi.org/10.1016/j.ijhydene.2021.03.109).
- [127] T.-C. software AB. *Thermo-Calc version 2021b*. May 1, 2023.

- [128] C. Ioannidou, Z. Arechabaleta, A. Navarro-López, A. Rijkenberg, R. M. Dalgliesh, S. Kölling, V. Bliznuk, C. Pappas, J. Sietsma, A. A. van Well, and S. E. Offerman. “Interaction of precipitation with austenite-to-ferrite phase transformation in vanadium micro-alloyed steels”. In: *Acta Materialia* 181 (2019), pp. 10–24. ISSN: 13596454. DOI: [10.1016/j.actamat.2019.09.046](https://doi.org/10.1016/j.actamat.2019.09.046).
- [129] H. E. Kissinger. “Reaction Kinetics in Differential Thermal Analysis”. In: *Analytical Chemistry* 29.11 (1957), pp. 1702–1706. DOI: [10.1021/ac60131a045](https://doi.org/10.1021/ac60131a045).
- [130] ASTM G129. “Standard Practice for Slow Strain Rate Testing to Evaluate the Susceptibility of Metallic Materials to Environmentally Assisted Cracking 1”. In: *ASTM Book of Standards* 00.Reapproved 2013 (2006), pp. 1–7. DOI: [10.1520/G0129-00R06.2](https://doi.org/10.1520/G0129-00R06.2).
- [131] ASTM E1181-02. “Standard Test Methods for Characterizing Duplex Grain Sizes”. In: *ASTM Book of Standards* 02.Reapproved 2008 (2008), pp. 1–15. DOI: [10.1520/E1181-02R23.Copyright](https://doi.org/10.1520/E1181-02R23.Copyright).
- [132] P. Castaño Rivera, V. P. Ramunni, and P. Bruzzoni. “Hydrogen trapping in an API 5L X60 steel”. In: *Corrosion Science* 54.1 (2012), pp. 106–118. DOI: [10.1016/j.corsci.2011.09.008](https://doi.org/10.1016/j.corsci.2011.09.008).
- [133] F. G. Wei, T. Hara, T. Tsuchida, and K. Tsuzaki. “Hydrogen trapping in quenched and tempered 0.42C-0.30Ti steel containing bimodally dispersed TiC particles”. In: *ISIJ International* 43.4 (2003), pp. 539–547. ISSN: 09151559. DOI: [10.2355/isijinternational.43.539](https://doi.org/10.2355/isijinternational.43.539).
- [134] T. Boot, P. Kömmelt, H. J. Brouwer, A. Böttger, and V. Popovich. “Effect of titanium and vanadium nano-carbide size on hydrogen embrittlement of ferritic steels”. In: *npj Materials Degradation* 9.2 (2025). ISSN: 23972106. DOI: [10.1038/s41529-024-00546-7](https://doi.org/10.1038/s41529-024-00546-7). URL: <http://dx.doi.org/10.1038/s41529-024-00546-7>.
- [135] A. Grajcar, R. Kuziak, and W. Zalecki. “Third generation of AHSS with increased fraction of retained austenite for the automotive industry”. In: *Archives of Civil and Mechanical Engineering* 12.3 (2012), pp. 334–341. ISSN: 16449665. DOI: [10.1016/j.acme.2012.06.011](https://doi.org/10.1016/j.acme.2012.06.011).
- [136] S. J. Kim, E. H. Hwang, J. S. Park, S. M. Ryu, D. W. Yun, and H. G. Seong. “Inhibiting hydrogen embrittlement in ultra-strong steels for automotive applications by Ni-alloying”. In: *npj Materials Degradation* 3.1 (2019), p. 12.
- [137] L. Vandewalle, T. Depover, and K. Verbeke. “Current state-of-the-art of hydrogen trapping by carbides: From theory to experiment”. In: *International Journal of Hydrogen Energy* March (2024). ISSN: 03603199. DOI: [10.1016/j.ijhydene.2024.03.266](https://doi.org/10.1016/j.ijhydene.2024.03.266).
- [138] P. Hammer, L. Romaner, and V. I. Razumovskiy. “Hydrogen trapping in mixed carbonitrides”. In: *Acta Materialia* 268.June 2023 (2024), p. 119754. ISSN: 13596454. DOI: [10.1016/j.actamat.2024.119754](https://doi.org/10.1016/j.actamat.2024.119754).

- [139] A. Drexler, B. Helic, Z. Silwayeh, C. Sommitsch, K. Mraczek, and J. Domitner. “Influence of Plastic Deformation on the Hydrogen Embrittlement Susceptibility of Dual Phase Steels”. In: *Key Engineering Materials* 926 KEM (2022), pp. 2077–2091. ISSN: 16629795. DOI: [10.4028/p-oeev61](https://doi.org/10.4028/p-oeev61).
- [140] P. Gong, J. Nutter, P. E. Rivera-Diaz-Del-Castillo, and W. M. Rainforth. “Hydrogen embrittlement through the formation of low-energy dislocation nanostructures in nanoprecipitation-strengthened steels”. In: *Science Advances* 6.46 (2020), pp. 6152–6163. ISSN: 23752548. DOI: [10.1126/sciadv.abb6152](https://doi.org/10.1126/sciadv.abb6152).
- [141] J. Rehr, K. Mraczek, A. Pichler, and E. Werner. “Mechanical properties and fracture behavior of hydrogen charged AHSS/UHSS grades at high- and low strain rate tests”. In: *Materials Science and Engineering: A* 590 (2014), pp. 360–367. ISSN: 09215093. DOI: [10.1016/j.msea.2013.10.044](https://doi.org/10.1016/j.msea.2013.10.044).
- [142] I. Moro, L. Briottet, P. Lemoine, E. Andrieu, C. Blanc, and G. Odemer. “Hydrogen embrittlement susceptibility of a high strength steel X80”. In: *Materials Science and Engineering: A* 527.27-28 (Oct. 2010), pp. 7252–7260. ISSN: 09215093. DOI: [10.1016/j.msea.2010.07.027](https://doi.org/10.1016/j.msea.2010.07.027).
- [143] M. N. Elkot, B. Sun, X. Zhou, D. Ponge, and D. Raabe. “Hydrogen-assisted decohesion associated with nanosized grain boundary κ -carbides in a high-Mn lightweight steel”. In: *Acta Materialia* 241 (2022), p. 118392. ISSN: 13596454. DOI: [10.1016/j.actamat.2022.118392](https://doi.org/10.1016/j.actamat.2022.118392).
- [144] M. Koyama, H. Springer, S. V. Merzlikin, K. Tsuzaki, E. Akiyama, and D. Raabe. “Hydrogen embrittlement associated with strain localization in a precipitation-hardened Fe-Mn-Al-C light weight austenitic steel”. In: *International Journal of Hydrogen Energy* 39.9 (2014), pp. 4634–4646. ISSN: 03603199. DOI: [10.1016/j.ijhydene.2013.12.171](https://doi.org/10.1016/j.ijhydene.2013.12.171).
- [145] T. Boot, T. A. Riemslog, E. T. Reinton, P. Liu, C. L. Walters, and V. Popovich. “In-situ hollow sample setup design for mechanical characterisation of gaseous hydrogen embrittlement of pipeline steels and welds”. In: *Metals* 11.8 (2021). ISSN: 20754701. DOI: [10.3390/met11081242](https://doi.org/10.3390/met11081242).
- [146] C. Park, N. Kang, S. Liu, J. Lee, E. Chun, and S. J. Yoo. “Effect of Prestrain on Hydrogen Embrittlement Susceptibility of EH 36 Steels Using In Situ Slow-Strain-Rate Testing”. In: *Metals and Materials International* 25.3 (2019), pp. 584–593. ISSN: 20054149. DOI: [10.1007/s12540-018-00221-y](https://doi.org/10.1007/s12540-018-00221-y). URL: <https://doi.org/10.1007/s12540-018-00221-y>.
- [147] K. Takai, H. Shoda, H. Suzuki, and M. Nagumo. “Lattice defects dominating hydrogen-related failure of metals”. In: *Acta Materialia* 56.18 (2008), pp. 5158–5167. ISSN: 13596454. DOI: [10.1016/j.actamat.2008.06.031](https://doi.org/10.1016/j.actamat.2008.06.031).
- [148] J. Shang, J. Guo, Z. Hua, B. King, T. Cui, and H. Wei. “Effects of plastic deformation on hydrogen trapping and hydrogen distribution in X80 pipeline steel”. In: *International Journal of Hydrogen Energy* December 2023 (2024). ISSN: 03603199. DOI: [10.1016/j.ijhydene.2023.12.272](https://doi.org/10.1016/j.ijhydene.2023.12.272). URL: <https://doi.org/10.1016/j.ijhydene.2023.12.272>.

- [149] C. Park, N. Kang, M. Kim, and S. Liu. “Effect of prestrain on hydrogen diffusion and trapping in structural steel”. In: *Materials Letters* 235 (2019), pp. 193–196. ISSN: 18734979. DOI: [10.1016/j.matlet.2018.10.049](https://doi.org/10.1016/j.matlet.2018.10.049). URL: <https://doi.org/10.1016/j.matlet.2018.10.049>.
- [150] A. Fukunaga. “Hydrogen embrittlement behaviors during SSRT tests in gaseous hydrogen for cold-worked type 316 austenitic stainless steel and iron-based superalloy A286 used in hydrogen refueling station”. In: *Engineering Failure Analysis* 160. February (2024), p. 108158. ISSN: 13506307. DOI: [10.1016/j.engfailanal.2024.108158](https://doi.org/10.1016/j.engfailanal.2024.108158). URL: <https://doi.org/10.1016/j.engfailanal.2024.108158>.
- [151] N. Verma, R. Delhez, N. M. van der Pers, F. D. Tichelaar, and A. J. Böttger. “The role of the substrate on the mechanical and thermal stability of Pd thin films during hydrogen (de) sorption”. In: *international journal of hydrogen energy* 46.5 (2021), pp. 4137–4153.
- [152] Hideki Hagi. *Diffusion coefficient of hydrogen in iron without trapping by dislocations and impurities*. 1994.
- [153] S. S. Rui, Q. N. Han, X. Wang, S. Li, X. Ma, Y. Su, Z. Cai, D. Du, and H. J. Shi. “Correlations between two EBSD-based metrics Kernel Average Misorientation and Image Quality on indicating dislocations of near-failure low alloy steels induced by tensile and cyclic deformations”. In: *Materials Today Communications* 27. May (2021), p. 102445. ISSN: 23524928. DOI: [10.1016/j.mtcomm.2021.102445](https://doi.org/10.1016/j.mtcomm.2021.102445). URL: <https://doi.org/10.1016/j.mtcomm.2021.102445>.
- [154] T. Hilditch, T. De Souza, and P. Hodgson. “Properties and automotive applications of advanced high-strength steels (AHSS)”. In: (2015), pp. 9–28.
- [155] C. C. Tasan, M. Diehl, D. Yan, M. Bechtold, F. Roters, L. Schemmann, C. Zheng, N. Peranio, D. Ponge, M. Koyama, K. Tsuzaki, and D. Raabe. “An Overview of Dual-Phase Steels: Advances in Microstructure-Oriented Processing and Micromechanically Guided Design”. In: *Annual Review of Materials Research* 45. April (2015), pp. 391–431. ISSN: 15317331. DOI: [10.1146/annurev-matsci-070214-021103](https://doi.org/10.1146/annurev-matsci-070214-021103).
- [156] D. Rudomilova, T. Prošek, P. Salvetr, A. Knaislová, P. Novák, R. Kodým, G. Schimo-Aichhorn, A. Muhr, H. Duchaczek, and G. Luckeneder. “The effect of microstructure on hydrogen permeability of high strength steels”. In: *Materials and Corrosion* 71.6 (2020), pp. 909–917.
- [157] D. Mallick, N. Mary, V. Raja, and B. Normand. “Study of diffusible behavior of hydrogen in first generation advanced high strength steels”. In: *Metals* 11.5 (2021), p. 782.
- [158] A. Drexler, B. Helic, Z. Silvayeh, K. Mraczek, C. Sommitsch, and J. Domitner. “The role of hydrogen diffusion, trapping and desorption in dual phase steels”. In: *Journal of Materials Science* 57.7 (2022), pp. 4789–4805. ISSN: 15734803. DOI: [10.1007/s10853-021-06830-0](https://doi.org/10.1007/s10853-021-06830-0). URL: <https://doi.org/10.1007/s10853-021-06830-0>.

- [159] K. S. Reddy, Y. Govindaraj, and L. Neelakantan. "Influence of microstructure on the hydrogen diffusion behavior in dual-phase steels: an electrochemical permeation study". In: *Journal of Materials Science* 57.41 (2022), pp. 19592–19611.
- [160] E. Rodoni, K. Verbeken, T. Depover, and M. Iannuzzi. "Effect of microstructure on the hydrogen embrittlement, diffusion, and uptake of dual-phase low alloy steels with varying ferrite-martensite ratios". In: *International Journal of Hydrogen Energy* 50 (Jan. 2024), pp. 53–65. ISSN: 03603199. DOI: [10.1016/j.ijhydene.2023.07.061](https://doi.org/10.1016/j.ijhydene.2023.07.061).
- [161] J. Sun, T. Jiang, Y. Sun, Y. Wang, and Y. Liu. "A lamellar structured ultrafine grain ferrite-martensite dual-phase steel and its resistance to hydrogen embrittlement". In: *Journal of Alloys and Compounds* 698 (2017), pp. 390–399. ISSN: 09258388. DOI: [10.1016/j.jallcom.2016.12.224](https://doi.org/10.1016/j.jallcom.2016.12.224).
- [162] D. P. Dunne, D. Hejazi, A. A. Saleh, A. J. Haq, A. Calka, and E. V. Pereloma. "Investigation of the effect of electrolytic hydrogen charging of X70 steel: I. The effect of microstructure on hydrogen-induced cold cracking and blistering". In: *International journal of hydrogen energy* 41.28 (2016), pp. 12411–12423.
- [163] M. Mohtadi-Bonab, J. Szpunar, and S. Razavi-Tousi. "Hydrogen induced cracking susceptibility in different layers of a hot rolled X70 pipeline steel". In: *International Journal of Hydrogen Energy* 38.31 (2013), pp. 13831–13841.
- [164] T. Depover, F. Vercruyssen, A. Elmahdy, P. Verleysen, and K. Verbeken. "Evaluation of the hydrogen embrittlement susceptibility in DP steel under static and dynamic tensile conditions". In: *International Journal of Impact Engineering* 123.March 2018 (2019), pp. 118–125. ISSN: 0734743X. DOI: [10.1016/j.ijimpeng.2018.10.002](https://doi.org/10.1016/j.ijimpeng.2018.10.002). URL: <https://doi.org/10.1016/j.ijimpeng.2018.10.002>.
- [165] T. Depover, E. Wallaert, and K. Verbeken. "Fractographic analysis of the role of hydrogen diffusion on the hydrogen embrittlement susceptibility of DP steel". In: *Materials Science and Engineering: A* 649 (2016), pp. 201–208. ISSN: 09215093. DOI: [10.1016/j.msea.2015.09.124](https://doi.org/10.1016/j.msea.2015.09.124). URL: <http://dx.doi.org/10.1016/j.msea.2015.09.124>.
- [166] R. Scharf, A. Muhr, G. Luckeneder, P. Larour, K. Mraczek, J. Rehr, F. Leomann, K.-H. Stellnberger, J. Faderl, and G. Mori. "Hydrogen embrittlement of DP-1000 flat steel sheet: Influence of mechanical properties, specimen geometry, pre-damaging and electrolytically zinc galvanizing". In: *Materials and Corrosion* 67.3 (2016), pp. 239–250.
- [167] E. Merson, A. V. Kudrya, V. A. Trachenko, D. Merson, V. Danilov, and A. Vinogradov. "Quantitative characterization of cleavage and hydrogen-assisted quasi-cleavage fracture surfaces with the use of confocal laser scanning microscopy". In: *Materials Science and Engineering: A* 665 (2016), pp. 35–46. ISSN: 09215093. DOI: [10.1016/j.msea.2016.04.023](https://doi.org/10.1016/j.msea.2016.04.023). URL: <http://dx.doi.org/10.1016/j.msea.2016.04.023>.

- [168] W. Qin and J. A. Szpunar. “A general model for hydrogen trapping at the inclusion-matrix interface and its relation to crack initiation”. In: *Philosophical Magazine* 97.34 (Dec. 2017), pp. 3296–3316. ISSN: 14786443. DOI: [10.1080/14786435.2017.1378451](https://doi.org/10.1080/14786435.2017.1378451).
- [169] B. Sun, W. Lu, B. Gault, R. Ding, S. K. Makineni, D. Wan, C. H. Wu, H. Chen, D. Ponge, and D. Raabe. “Chemical heterogeneity enhances hydrogen resistance in high-strength steels”. In: *Nature Materials* 20 (12 Dec. 2021), pp. 1629–1634. ISSN: 14764660. DOI: [10.1038/s41563-021-01050-y](https://doi.org/10.1038/s41563-021-01050-y).
- [170] E. Martínez-Pañeda, Z. D. Harris, S. Fuentes-Alonso, J. R. Scully, and J. T. Burns. “On the suitability of slow strain rate tensile testing for assessing hydrogen embrittlement susceptibility”. In: *Corrosion Science* 163 (Feb. 2020). ISSN: 0010938X. DOI: [10.1016/j.corsci.2019.108291](https://doi.org/10.1016/j.corsci.2019.108291).
- [171] P.-y. Liu, B. Zhang, R. Niu, S.-l. Lu, P. A. Burr, H. Lu, A. Guo, and H.-w. Yen. *Engineering metal-carbide hydrogen traps in steels*. 2024. DOI: [10.1038/s41467-024-45017-4](https://doi.org/10.1038/s41467-024-45017-4).
- [172] L. Cho, P. E. Bradley, D. S. Lauria, M. L. Martin, M. J. Connolly, J. T. Benzing, E. J. Seo, K. O. Findley, J. G. Speer, and A. J. Slifka. “Characteristics and mechanisms of hydrogen-induced quasi-cleavage fracture of lath martensitic steel”. In: *Acta Materialia* 206 (Mar. 2021). ISSN: 13596454. DOI: [10.1016/j.actamat.2021.116635](https://doi.org/10.1016/j.actamat.2021.116635).
- [173] T. Boot, P. Kömmelt, R. W. Hendriks, A. J. Böttger, and V. Popovich. “Effect of plastic deformation on the hydrogen embrittlement of ferritic high strength steel”. In: *npj Materials Degradation* 9.39 (1 Dec. 2025). ISSN: 23972106. DOI: [10.1038/s41529-025-00592-9](https://doi.org/10.1038/s41529-025-00592-9).
- [174] T. Boot, T. Riemsdag, E. Reinton, P. Liu, C. L. Walters, and V. Popovich. “Assessing the Susceptibility of Existing Pipelines to Hydrogen Embrittlement”. In: *Minerals, Metals and Materials Series* 5 (2021), pp. 722–729. ISSN: 23671696. DOI: [10.1007/978-3-030-65261-6_65](https://doi.org/10.1007/978-3-030-65261-6_65). URL: http://dx.doi.org/10.1007/978-3-030-65261-6_65.
- [175] T. Boot, S. Sagar, P. Dey, and V. Popovich. “Hydrogen trapping efficiency of carbide nano-precipitates and their effect on hydrogen embrittlement susceptibility of single phase ferritic AHSS”. In: *Proceedings of the Fourth International Conference on Metals & Hydrogen* C04 (2022).

ACKNOWLEDGEMENTS

The journey of a PhD student is one of ups and downs. There are always more setbacks than triumphs. Problems often arise that are out of our control to solve, and so we just have to learn to accept them. Rather than getting stuck thinking about problems, it helps to be appreciative of the good things that we have, like the people are around us. This makes the PhD journey not only one of self discovery, but also one of discovering the importance of our relationships to others.

First and foremost, I want to extend my gratitude to my project supervisors, Dr. Vera Popovich and Dr. Amarante Böttger. They supervised me previously for my masters and bachelors projects, respectively, which contributed to a comfortable setting within the team. Their style of supervision is one that I admire and aim to emulate. One of taking a step back when things are moving along but being available for help at any point when required. I am especially thankful for the time they spent reviewing my manuscripts as quickly as possible so I could revise, improve and (re-)submit without delay. This is not something that should be taken for granted as a PhD student. Furthermore, Vera taught me a valuable mantra that pops up in the back of my head whenever I encounter a problem. It evolved from many conversations we had, where I told her one of my plans had not worked out, to which she responded: "OK, so what's plan B?". Always plan for things to go wrong, and be ready with an alternative when they do. I will carry this with me throughout my career.

This project was one part of the larger Designing Hydrogen-Resistant Alloys Through Novel Multi-Scale Modelling and Experimentation (De-Hy) project. My thanks go out to our project partners m2i, University of Groningen, Cambridge University, Nedschroef, Allseas and specifically TATA Steel in IJmuiden, who was the main industrial partner, for making the project possible. Ir. Pascal Kömmelt from TATA Steel deserves thanks in particular for his contribution to all the papers published as part of my work package. It was invaluable to have someone with practical know-how on both the steels and testing methods used in the research, who has a critical eye when reviewing manuscripts, and who is a great partner for discussions on fundamental hydrogen embrittlement mechanisms and how they manifest on macro scale.

It has been my pleasure to act as supervisor for several students during my project. I want to thank Lorenzo, Elena, Maria, Sara and Eirik for showing me what it is like on the other side of the student-supervisor relationship. I have been lucky to supervise motivated, intelligent and independent students that took the challenge of studying Hydrogen Embrittlement and contributing to its understanding. Hopefully I have managed to convey my interest in the topic to you all. Specific thanks go out to Sara and Eirik for

contributing to studies that became a part of this thesis.

Doing a PhD project can be a lonely process. This makes it all the more important to have people around you to share experiences with. I think that we are very lucky at the MSE department to have so many amazing colleagues around. A non-exhaustive list of those I am very glad to have met: Jithin, Soroush, Vitoria, Arash, Jaji, Eszter, Can, Luís, Daniel, Joep, Aswin, Philipp, Gautham, Elsa, Khatereh, Virginia, Amir, Arthur, Jasper, Arjun, Alice, Mohammed, Fabian, Hannah, José, Julia, Keer, Marco, Camilla, Gaojie, Jhon, Konstantina, Pablo, Robert, Tobia, Yeli, Zamran, Zhaorui, Jianing, Ehsan and Devi. It has been a pleasure to share my PhD experience with you, and I am sorry if I missed your name here. Of particular importance to this shared experience was the everyday exchange of (cultural) points of view during one of our enlightening lunch discussions. Cucumbers are crunchy water, and they are berries. I want to thank those who started and ended the PhD around the same time as specifically: my project partner and office mate Saurabh, my office mate Can, Devi, Arjun, and Luís from the masters curriculum, Eszter, José, and my flatmate Alexander who got to see me at home in the best and worst of times (as I saw him).

I don't think any experimental project could have been successful without the help of our technicians. They provide essential continuity in knowledge of experimental methods and setups that is not possible to achieve within one PhD project. Thank you Ton, Elise, Raymond, Sean, Sander, Durga, Patrick, Remko, Jurriaan, Ruud, Richard, Rob, Julia, Hans, Kees and Frans. There are two of them that I want to thank specifically here: Ton Riemslog and Hans Brouwer. Ton is an endless source of creative solutions to design problems and has helped me overcome many of them since my masters project. When coming up with as many ideas as Ton does, not all of them can be implemented. A select few of them, however, have been the key to success in my work. His is an underappreciated role, which is why I want to highlight it here. Hans helps so many people at the same time that I have never figured out how he fits it in a work day. In between his busy schedule, he somehow also finds time to talk about not just technical challenges, but topics like science, health, religion and life itself. His enthusiasm and work ethic are inspiring, as is his ability to discuss topics on which we fundamentally disagree while remaining kind, understanding and professional. Our chats have been the favourite part of many of my days.

Lastly my eternal gratitude goes out to my family and my girlfriend Chaandi. I still think my parents know me better than myself. It was my father who finally convinced me to apply for the PhD after he noted my enthusiasm every time I talked about the topic, something that I had yet to notice myself. All of us in the family have been through life-changing events over the past years, of both personal and professional nature. For some of us, these years have been the hardest of our lives. I am incredibly grateful to have made it through together, and for how it has brought us closer to each other. I could not have done this without you. Chaandi and I met during my last year of the PhD, which as any candidate will say, is not a great time to start a relationship. Her kindness, patience and love have helped me push through the final stages of the project, and have allowed me to return to myself again in an environment filled with love and care. Chaandi, you are my person, and I love you a little more every day.

CURRICULUM VITÆ

Tim BOOT

18-05-1995 Born in Rotterdam, The Netherlands

EDUCATION

2013-2016 Bachelor of Science Mechanical Engineering (Werktuigbouwkunde)
Delft University of Technology

2017-2020 Master of Science Materials Science & Engineering
Delft University of Technology

2020-2024 PhD. Materials Science & Engineering
Delft University of Technology
Thesis: Hydrogen Embrittlement Susceptibility of Ferritic
High Strength Steels
Promotors: Dr. V. A. Popovich & Dr. A. J. Böttger

PROFESSIONAL EXPERIENCE

2018-2019 Researcher at NPSP BV

LIST OF PUBLICATIONS

5. T. Boot, P. Kömmelt, R. W. Hendrikx, A. J. Böttger, and V. Popovich. “Effect of plastic deformation on the hydrogen embrittlement of ferritic high strength steel”. In: *npj Materials Degradation* 9.39 (1 Dec. 2025). ISSN: 23972106. DOI: [10.1038/s41529-025-00592-9](https://doi.org/10.1038/s41529-025-00592-9)
4. T. Boot, P. Kömmelt, H. J. Brouwer, A. Böttger, and V. Popovich. “Effect of titanium and vanadium nano-carbide size on hydrogen embrittlement of ferritic steels”. In: *npj Materials Degradation* 9.2 (2025). ISSN: 23972106. DOI: [10.1038/s41529-024-00546-7](https://doi.org/10.1038/s41529-024-00546-7). URL: <http://dx.doi.org/10.1038/s41529-024-00546-7>
3. T. Boot, A. Suresh Kumar, S. Eswara, P. Kömmelt, A. Böttger, and V. Popovich. “Hydrogen trapping and embrittlement of titanium- and vanadium carbide-containing steels after high-temperature hydrogen charging”. In: *Journal of Materials Science* 59.18 (2024), pp. 7873–7892. ISSN: 15734803. DOI: [10.1007/s10853-024-09611-7](https://doi.org/10.1007/s10853-024-09611-7)
2. L. E. Faucon, T. Boot, T. Riemslog, S. P. Scott, P. Liu, and V. Popovich. “Hydrogen-Accelerated Fatigue of API X60 Pipeline Steel and Its Weld”. In: *Metals* 13.3 (2023). ISSN: 20754701. DOI: [10.3390/met13030563](https://doi.org/10.3390/met13030563)
1. T. Boot, T. A. Riemslog, E. T. Reinton, P. Liu, C. L. Walters, and V. Popovich. “In-situ hollow sample setup design for mechanical characterisation of gaseous hydrogen embrittlement of pipeline steels and welds”. In: *Metals* 11.8 (2021). ISSN: 20754701. DOI: [10.3390/met11081242](https://doi.org/10.3390/met11081242)

Conference Proceedings:

2. T. Boot, T. Riemslog, E. Reinton, P. Liu, C. L. Walters, and V. Popovich. “Assessing the Susceptibility of Existing Pipelines to Hydrogen Embrittlement”. In: *Minerals, Metals and Materials Series* 5 (2021), pp. 722–729. ISSN: 23671696. DOI: [10.1007/978-3-030-65261-6_65](https://doi.org/10.1007/978-3-030-65261-6_65). URL: http://dx.doi.org/10.1007/978-3-030-65261-6_65
1. T. Boot, S. Sagar, P. Dey, and V. Popovich. “Hydrogen trapping efficiency of carbide nano-precipitates and their effect on hydrogen embrittlement susceptibility of single phase ferritic AHSS”. in: *Proceedings of the Fourth International Conference on Metals & Hydrogen C04* (2022)

Hi ChatGPT. I'm looking for an inspirational quote to end my PhD thesis with, but I have no inspiration. Could you come up with a quote for me instead? The field is materials science.

Perfect—since your field is **materials science**, here are some quotes that align more closely with the themes of **discovery, structure, transformation, and persistence** that often define the field:

"The best materials aren't found—they're made."

An original quote (suitable for adding a personal touch)

"To understand a material is to see order in complexity and beauty in the invisible."

Original/philosophical (tailored for thesis use)

"Science may never come up with a better office communication system than the coffee break, but materials science is how we build everything that holds the coffee."

Light-hearted, semi-original spin (for a more humorous exit)

Wow, thank you! This saves me a lot of time I would have had to spend thinking.

